Micro Electro Mechanical Systems for Microwave and Millimeter Wave Circuits

Sisteme micro-electro-mecanice pentru circuite de microunde şi unde milimetrice

Micro Electro Mechanical Systems for Microwave and Millimeter Wave Circuits

EDITORS:

Mehmet Kaynak, Alexandru Müller,
Dan Dascălu, Roberto Sorrentino

EDITURA ACADEMIEI ROMÂNE

Bucureşti, 2014

The responsibility for originality and the contents of the articles lies exclusively with the authors.

Address: EDITURA ACADEMIEI ROMÂNE
Calea 13 Septembrie nr. 13, sector 5,
050 711, Bucureşti, România,
Tel. 4021-3188146, 4021-3188106
Fax: 4021-3182444
E-mail: edacad@ear.ro
Internet: http://www.ear.ro

Peer reviewers:
Prof. Gheorghe Brezeanu, Dr. Mihai Mihailă, m.c. al Academiei României

Descrierea CIP a Bibliotecii Naţionale a României

Micro Electro Mechanical Systems for Microwave and Millimeter Wave Circuits / editors: Mehmet Kaynak, Alexandru Müller, Dan Dascălu, Roberto Sorrentino; ed.- Bucureşti : Editura Academiei Române, 2014
ISBN 978-973-27-2438-5

I. Mehmet Kaynak (ed.)
II. Alexandru Müller (ed)
III. Dan Dascălu (ed.)
IV. Roberto Sorrentino (ed.)

62-83
62-86

Editorial assistant: Mihaela Marian
Computer operator: Elena Trică
Cover: Elena Trică

Passed for press: 06.2014. Size: 16 / 70 × 100.
Printed sheets: 11
D.L.C. for large libraries: 621.3.029.6
D.L.C. for small libraries: 62

CONTENTS

FOREWORD 7

FAST AND NON INTRUSIVE FAILURE ANALYSIS OF BiCMOS RF-MEMS
N. TORRES MATABOSCH, F. COCCETTI, M. KAYNAK, B. ESPANA, B. TILLACK, J.L. CAZAUX 9

DESIGN AND VALIDATION OF RF-MEMS WIDE BAND PHASE SHIFTERS IN HARSH ENVIRONMENTS
A. HARCK, P. BLONDY, S. FARGEOT, S. VILLERS 19

MEMS-BASED ADJUSTABLE HIGH-Q E-PLANE FILTERS
F. GENTILI, V. NOCELLA, L. PELLICCIA, F. CACCIAMANI, P. FARINELLI, R. SORRENTINO 27

AN ACCURATE EM MODELING OF 140 GHz BiCMOS EMBEDDED RF-MEMS SWITCH
S. TOLUNAY, M. WIETSTRUCK, A. GÖRITZ, M. KAYNAK, B. TILLACK 35

FREQUENCY AND BANDWIDTH CONTROL OF SWITCHABLE ICROSTRIP BANDPASS FILTERS USING RF-MEMS OHMIC SWITCHES
Z. BRITO-BRITO, I. LLAMAS-GARRO, L. PRADELL, F. GIACOMOZZI, S. COLPO 43

HIGH-FREQUENCY OPTIMIZATION OF BiCMOS EMBEDDED THROUGH-SILICON VIAS FOR BACKSIDE-INTEGRATED MEMS
M. WIETSTRUCK, M. KAYNAK, S. MARSCHMEYER, A. GÖRITZ, S. TOLUNAY, S. KURTH, B. TILLACK 53

RF MEMS MODELING WITH ARTIFICIAL NEURAL NETWORKS
L. VIETZORRECK, M. MILIJIĆ, Z. MARINKOVIĆ, T. KIM, V. MARKOVIĆ, O. PRONIĆ-RANČIĆ 63

MEMBRANE SUPPORTED D-BAND ANTENNA PROCESSED ON LOW-RESISTIVITY SILICON
A.-C. BUNEA, A. AVRAM, D. NECULOIU, C. RUSCH 67

ANALYSIS OF RF MEMS SWITCHES WITH METAL-METAL CONTACTS
S. KURTH, S. VOIGT, A. BERTZ, S. HAAS, J. FRÖMEL, T. GESSNER, A. AKIBA, K. IKEDA 75

LONG-TERM RELIABILITY OF RF-MEMS DIELECTRIC-LESS CAPACITIVE SWITCHES
V. MULLONI, F. GIACOMOZZI, G. RESTA, B. MARGESIN 81

NONLINEARITY DETERMINATION AND LINEARITY DEGRADATION IN RF MEMS MULTI-DEVICE CIRCUITS
U. SHAH, M. STERNER, J. OBERHAMMER 89

COMPARATIVE STUDY OF CONTACTED AND CONTACT LESS CHARGING IN RF MEMS CAPACITIVE SWITCHES
M. KOUTSOURELI, L. MICHALAS, P. MARTINS, E. PAPANDREOU, A. LEULIET, S. BANSROPUN, G. PAPAIOANNOU, A. ZIAEI 99

SENSITIVITY, REPEATABILITY AND LATERAL SCANNING RESOLUTION OF MICROMACHINED NEAR-FIELD MILLIMETER-WAVE PROBE FOR SKIN CANCER DIAGNOSIS
F. TÖPFER, S. DUDOROV, J. OBERHAMMER 107

DESIGN AND MULTIPHYSICS ANALYSIS OF LOW-LOSS 60-GHz SPNT RF-MEMS SWITCHES
M.W. ROUSSTIA, M.H.A.J. HERBEN 117

3D MICROMACHINED Ka (30 GHz) BAND RF MEMS FILTER FOR ON-BOARD SATELLITE COMMUNICATION SYSTEMS
A.Q.A. QURESHI, L. PELLICCIA, S. COLPO, F. GIACOMOZZI, P. FARINELLI, B. MARGESIN 127

CONTROLLABLE ESSENCE OF COMPLEX MATERIALS EXPLOITING TWO-HOT-ARM ELECTROTHERMAL ACTUATORS
A.X. LALAS, N.V. KANTARTZIS, T.D. TSIBOUKIS 137

A CARBON NANOTUBES RIDGE GAP RESONATOR
A.M SALEEM, S. RAHIMINEJAD, V. DESMARIS, P. ENOKSSON 147

DESIGN OF AN UWB ANTENNA WITH A NOVEL RECONFIGURABLE MEMS BAND NOTCH ACTUATED WITHOUT BIAS LINES
A. NEMATI, B.A. GANJI 153

RESIDUAL STRESS AND SWITCHING TRANSIENT STUDIES FOR BiCMOS EMBEDDED RF MEMS SWITCH USING ADVANCED ELECTRO-MECHANICAL MODELS
A. MEHDAOUI, S. ROUVILLOIS, G. SCHRÖPFER, G. LORENZ, M. KAYNAK, M. WIETSTRUCK 163

FOREWORD

The main scope of the MEMSWAVE conference is to bring together scientists from different universities, research institutes, industrial companies interested in the development of the RF-MEMS field, to create a forum for the knowledge exchange between the RF-MEMS players, provide a qualified international forum for researchers and people from the industry, interested in the area and introduce to the most recent advances and achievements, especially on European activities.

The MEMSWAVE workshop was generated by the European project "Micromachined Circuites for Microwave and Millimeter Wave Applications" <<MEMSWAVE>> (1998-2001) coordinated by IMT-Bucharest. The project was nominated between the ten finalists (from 108 participants) to the Descartes Prize 2002.

This qualified international forum, which has become a reference point for the RF MEMS field and gathering interest from all over Europe and the rest of the world, was started in Sinaia Romania. The first 2 editions were organized by IMT Bucharest at Sinaia in 1999 and 2001. A special volume in the series Micro and Nanoengineering "Micromachined Microwave Devices and Circuits" of the Romanian Academy Press, was dedicated to the second edition of the workshop and was published in 2002.

Starting from 2002, the MEMSWAVE workshop is an itinerant European event and has become a reference point for the field, gathering interest from all over Europe and the rest of the world.

The next editions were held in Heraklion and Toulouse. From 2004 the MEMSWAVE workshop was connected to the European FP6 Network of Excellence in RF MEMS "AMICOM" and was strongly supported by this network. Most of the European teams involved in these challenging topics were partners in the AMICOM project. The workshop was organized in Uppsala (2004), Lausanne (2005), Orvieto (2006), Barcelona (2007) and became conference being important instruments for knowledge dissemination of the AMICOM network results.

In 2008 at Fodele, Greece, took place the first MEMSWAVE conference following the completion of AMICOM. In 2009, the conference was organized by the MemSRaD Research Group of the Fondazione Bruno Kessler (FBK), in 2010 by Universita del Salento, Lecce, in 2011 by University of Athens, in 2012 by METU-MEMS Center of Middle East Technical University (METU) Ankara.

The conference is technically sponsored by the European Microwave Association (EuMA). However, the significant number of contribution has manifested the lasting support of the European RF MST community to this event.

It is now a tradition to publish the papers in the Series of Micro and Nanotechnologies of the Romanian Academy Press. Previous volumes may be requested at IMT-Bucharest (print@imt.ro). The present volume contains the papers presented at the 14th edition of the MEMSWAVE conference organized by IHP (Innovations for High Performance Microelectronics) Frauenhofer, Frankfurt (Oder), Germany, in July 2013, in Postdam.

The editors
May 2014

Fast and Non Intrusive Failure Analysis of BiCMOS RF-MEMS

N. TORRES MATABOSCH[1,2], F. COCCETTI[1,2], M. KAYNAK[3], B. ESPANA[4], B. TILLACK[3] and J.L. CAZAUX[4]

[1]CNRS, LAAS, 7 avenue du Colonel Roche F-31400 Toulouse, France
[2]Univ de Toulouse, UPS, LAAS, F-31400 Toulouse, France
[3]IHP, Im Technologiepark 25, 15236 Frankfurt (Oder), Germany
[4]Thales Alenia Space, 26 Avenue Jean-François Champollion, 31037 Toulouse, France
E-mail: #ntorres@laas.fr

Abstract. A cost effective and non-intrusive failure analysis methodology applied to capacitive RF-MEMS components based on a standard 250 nm BiCMOS technology is presented. The approach relies on non contact profilometry and an equivalent circuit model extracted in past works. The failure analyses are based on space application specifications, and allow to carry out a wafer level selection of functional devices (screening).

1. Introduction

RF-MEMS technology is considered to be one of the most promising solutions for advanced frequency agile RF architectures. Combining this technology with the impressive performances of BiCMOS's in a single process represents a switching paradigm in RF systems design. Even though process dispersions in CMOS technology are known to be very small, they may yield significant deviation in the behavior of MEMS devices. Therefore, it is very important to study the relationship between the fabrication process parameters and the effects of the variation on the RF performance which allow the Design for Reliability implementation. An accurate and versatile model would significantly help to predict the process variation effects in design level.

In terms of reliability, all the failure mechanisms have already been studied and classified by means of the FMEA (Failure Mode and Effect Analysis) [1]. However, standard methodology and failure criteria definition are missing nowadays. The key issue is to detect after manufacturing which parameter of the

device (electrical or mechanical) can be used as an indicator of possible future failure mechanisms in each specific application. This could eliminate the default switch over the wafer defining the yield of the process regarding reliability. This is the purpose of the present work developed in the framework aerospace application.

2. Switch Description

A. Brief Technology Description

Figure 1 illustrates the RF-MEMS switch integration in IHP's 0.25 μm SiGe BiCMOS process (SG25H1) based on 5 aluminum metal layers [2]. The capacitive switch is built between the two metal layers (M2 and M3). M3 is the membrane and it is realized using a stress controlled Ti/TiN/AlCu/Ti/TiN stack. The RF line is built in M2 and the high-voltage electrodes are formed using the bottom metal layer (M1). The additional RF-MEMS switch process only adds 1 more mask to the standard BiCMOS flow in order to release the RF-MEMS device. Thus, it does not increase the mask cost which is one of the main concerns of these technologies.

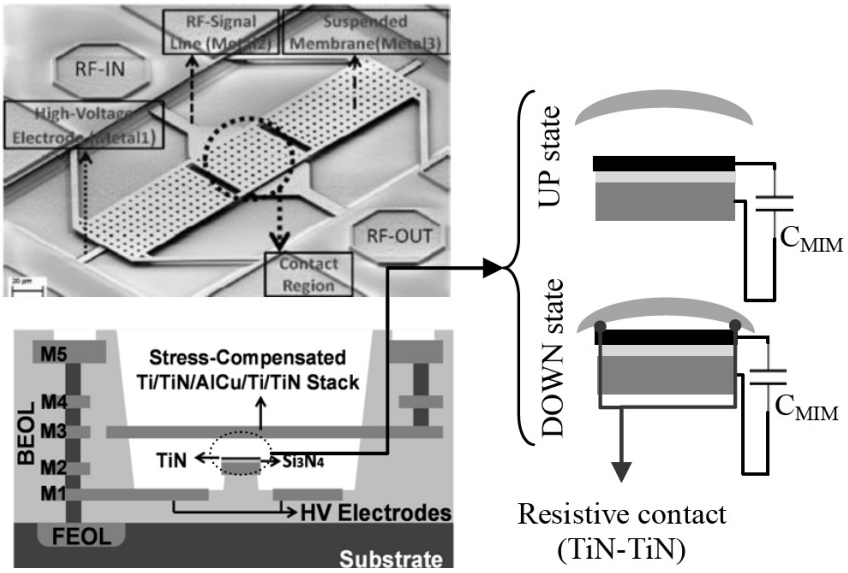

Fig. 1. Switch (top) and cross section (bottom) with a zoom of the contact region of the BiCMOS-MEMS fabrication process.

All the fabricated devices use the same contact region [3] and the target operating frequency is tuned by adding series inductances at the anchors of the switch [4]. The main advantage of this solution is that the membrane is mechanically optimized only one time in order to yield high reliability, while the

switch can be designed to work at different frequencies without affecting the mechanical performance. On the other hand, the bandwidth of the switch is reduced at lower frequencies because of the higher values of inductances (hence higher losses and lower Q-factor) that are needed. For this reason these switches are typically suitable for applications at frequencies higher than 40 GHz.

3. Failure Analysis

In past work an accurate scalable lumped-elements model has already been proposed for these switches [5]. The relevance of the proposed model resides in its capability to map all the lumped-elements back to specific constitutive parts (shape and size) of the device, provides by this way a complete and detailed electrical description. This model has been moreover used to trace back and to detect possible manufacturing flaw or deviation due to technological dispersion.

The purpose of the present paper is to introduce an evolution of these past works by proposing a failure analysis selection criteria (screening) for mission profiles coming from space applications. From the manufacturer point of view, the availability of an effective screening procedure is paramount. The definition of the selection criteria depend on the capability of the component to satisfy the targeted application performance, for given working conditions. This paper uses the industrial requirements provided by the industrial partner (Thales Alenia Space) presented in [6]. According to them, a maximum deviation of 10% in V_{PIN} and V_{POUT} and an increase of 1dB in IL for 1h of continuous stress are assumed as acceptable limits beyond which failure is detected (failure criteria). The actuation profile has been monitored through RF parameters (specifically $|S_{12}(V)|$) measurements since the DOWN state (contact) position is reached below the mechanical pull-in.

The 8-inch wafer is divided in cells within which the switches are replicated (Fig. 2). The size of the cell has been previously established and studied by the manufacturer. One quarter of wafer is used for the presented results since horizontal and vertical symmetry applies. The availability of a large number of devices allows a fair monitoring of the process dispersion and it is instrumental to assess the reliability of the device for given industrial specifications [7]. Another important point is that the reliability study presented hereafter can be extended to any type of switches using the same movable part.

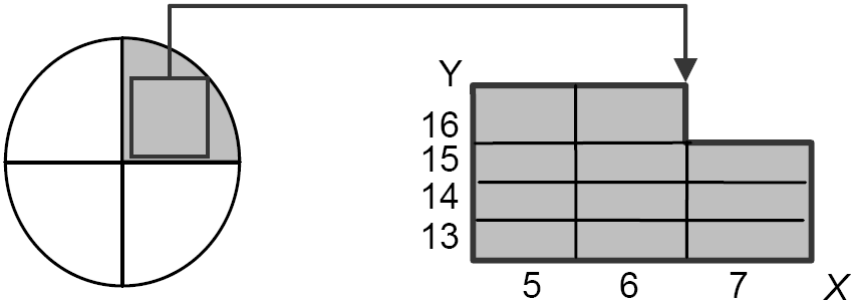

Fig. 2. Quarter of 8 inch wafer studied for the reliability tests.

A. Definition of Selection Criterion

Several devices of each cell have been held in DOWN position during 1 h measuring the IL and the pull-in/out voltage every 10 min. Fig. 3 plots the deviation after stress of the pull-out voltage for several identical devices with different initial V_{POUT}. It is demonstrated that the higher the V_{POUT}, the lower is the deviation after stress. Moreover, the difference between V_{PIN} and V_{POUT} plays also an important role and it should be also as low as possible. Applying the aforementioned industrial requirements (10% deviation in V_{POUT}) on devices taken on the entire wafer, a limited number of components succeeded the tests. These devices (in black dots in Fig. 3) are characterized by:

$$V_{POUT} > 36 \text{ V} \tag{1}$$

and

$$V_{PIN} - V_{POUT} \leq 1 \tag{2}$$

which are therefore chosen as the sought selection criteria.

The condition (2) is due to the short distance between the different metal layers used for the electrodes and the transmission line. It is well known that the relationship between the gap (g) and the applied voltage (V) is related to the stiffness (k), the initial gap between actuator and membrane (g_0) and the size of the actuator (surface (S), thickness (t_d) and material (ε_d)) by mean of the following relation [8]:

$$V = \sqrt{\frac{2k}{\varepsilon_0 S}}\, g^2 \left(g_0 - g\right) \tag{3}$$

Plotting the g(V) curve of the successfully tested devices (Fig. 4) using (3), it becomes evident that the correspondent actuation voltage is placed in the quasi-linear region (below pull-in) meaning that the V_{PIN} and V_{POUT} are coincident. The distance between membrane and line is smaller than 2/3 of the distance between the membrane and the electrode (g_0).

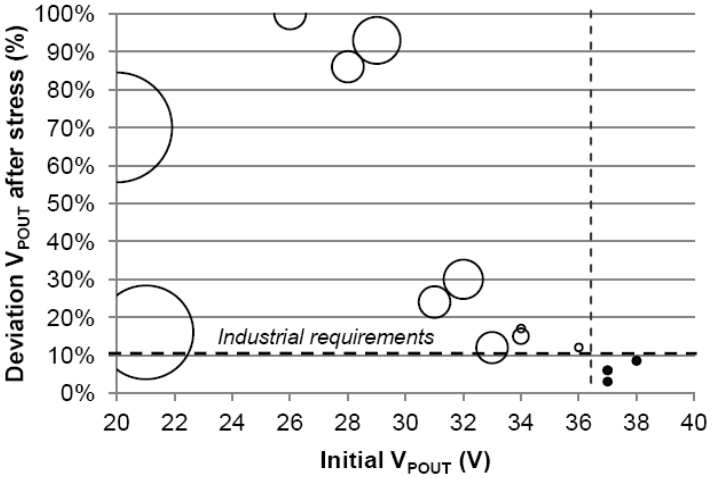

Fig. 3. Relation between the deviation after 1h of stress and the initial VPOUT. The size of the disk represents the difference between VPIN and VPOUT. The black point represents the devices that succeeded the tests

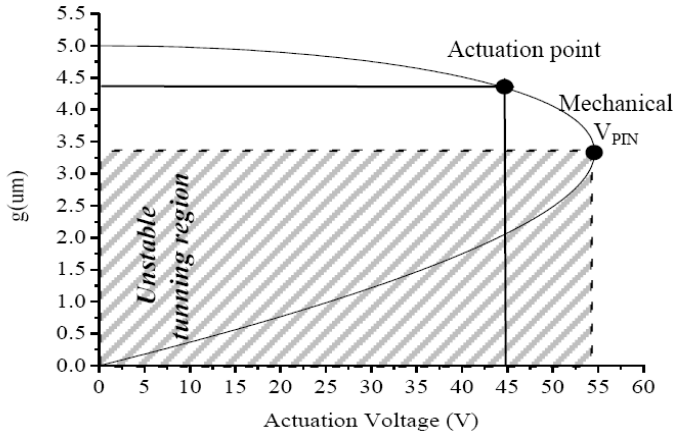

Fig. 4. g(V) of a succeeded device with the actuation point when applying 45V and the mechanical pull-in.

B. Methodology Applied for Failure Detection

Once the selection criterion has been established, the next step is to develop a technique in order to predict which devices accomplish $V_{POUT} > 36V$. The proposed screening protocol is based on distance measurement between different metal layers. This approach is cost-effective (very quick), non-intrusive (no activation of the device is needed) and can be implemented over the whole wafer (also in TCV – Technology Characterization Vehicles specific cells).

In Table 1 the measurements of the gap between membrane and electrode (M1-M3) and between membrane and line (M2-M3) for the tested devices in UP state (OFF) is depicted. This result demonstrates the possibility to detect by means of a profilometer measurement weather the device is compliant with the targeted performances. Distances about 2.8 μm and 4.7 μm from M2-M3 and M1-M3 respectively coincide with pull-out voltages above 36V which is the established criteria.

Table 1. Distance between metals before and after stress

Switch	M2-M3		M1-M3	
	Reference	***After***	***Reference***	***After***
X6_Y13_30G	2.26±0.06	2.3	5.18±0.09	4.9
X6_Y13_50G		1.5		5
X6_Y14_30G	2.3±0.35	2.5	5.26±0.13	5.1
X6_Y15_30G	2.66±0.12	2.8	5.03±0.14	4.8
X6_Y15_50G		2.6		5
X6_Y16_40G	2.57±0.04	**2.7**	5.07±0.09	**4.9**
X6_Y16_50G		2.6		4.9
X7_Y13_40G	2.33±0.05	2.36	5.5±0.7	5
X7_Y13_50G		2.4		4.9
X7_Y14_40G	2.56±0.05	**2.7**	4.8±0.01	**4.8**
X7_Y15_30G	2.58±0.06	**2.87**	4.75±0.2	**4.47**
X7_Y15_40G		**2.8**		**4.5**

The name of the switch is given by: X*x*_Y*y*_*f*G where *x,y* are the position over the wafer and *f* is the working frequency.

Regarding the distribution over the wafer, it is observed that the regions placed at the exterior part of the wafer (X7) succeed the tests (Fig. 5). This result is very useful for the manufacturer since it allows a performance based (RF and lifetime) monitoring and analysis of the wafer yield.

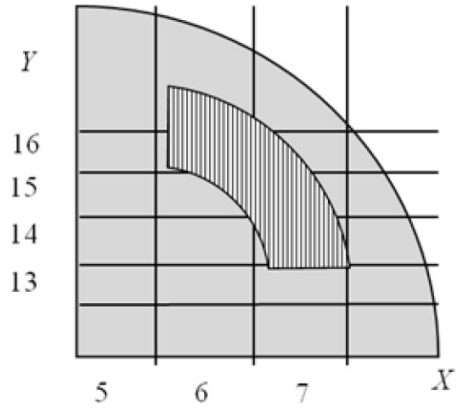

Fig. 5. Area of the wafer with optimal RF and lifetime performance.

C. Failure Mechanism Study

Comparing both distances (M1–M3 and M2–M3) with the reference value extracted from the devices of the same cell, it has been observed that the failure mechanism is due to fatigue and creep. Since the electrostatic force is applied on the lateral part of the membrane, the creep effect turns out to decrease the distance M1–M3 which implies an increase of the distance between M2–M3 (Fig. 6).

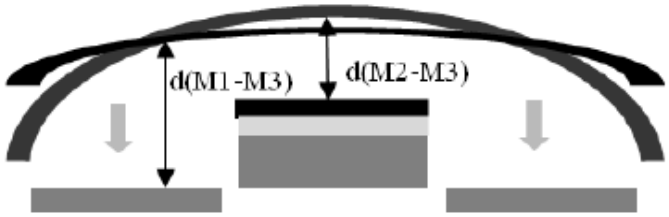

Fig. 6. Schema of the mechanical deformation before (black) and after (red) stress.

The occurrence of fatigue phenomena was observed by comparing the S-parameters in UP state before and after the test (Fig. 7). By using the equivalent circuit model of the device described in [5], the undesired resonance found at 35GHz has been properly modeled and attributed to the likely breaking of one of the suspending arms. A clear evidence of this failure mechanism is given by the excellent agreement between the measurement of the defective device (after stress) and the equivalent circuit model modified in order to account for this failure (broken arm).

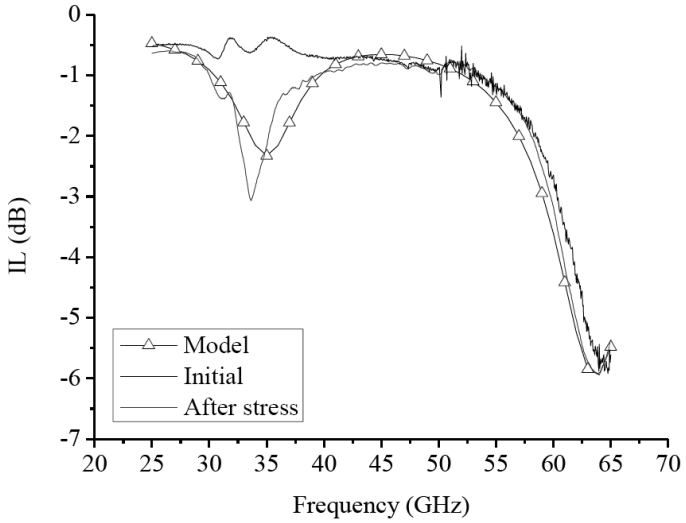

Fig. 7. Comparison of IL before (black) and after (red) stress with the model (triangle).

With respect to the schematic presented in [5], beside the effect of the broken arm on the Lanchor, the parameters that have been also modified are the capacitances CMEMS and CM1-M3. In fact, due to the fatigue, the distance between the metals has changed and both values of capacitance should be modified using (4) and (5) respectively.

$$C_{MEMS}^{failed} = C_{MEMS} \cdot \frac{d_{M2-M3}^{initial}}{d_{M2-M3}^{final}} \tag{4}$$

$$C_{M1-M3}^{failed} = C_{M1-M3} \cdot \frac{d_{M1-M3}^{initial}}{d_{M1-M3}^{final}} \tag{5}$$

In order to avoid failure mechanisms associated with fatigue and creep three possible approaches are typically envisioned. Going in order of growing implementation difficulties they are: to increase the effective Young's modulus by material engineering, to increase the membrane thickness and finally to redesign the membrane (anchors) shape. An optimal solution may pass through a combination of them.

4. Conclusion

This paper has showed a cost-effective and non-intrusive reliability monitoring technique such to predict creep and/or fatigue induced phenomena. The proposed reliability approach has demonstrated its validity and effectiveness in observing and analyzing the MEMS process yield, be it within the same wafer or wafer to wafer. This is a very important achievement for future commercialization of RF-MEMS devices and circuits.

Acknowledgments. The authors would like to thank the IHP pilot line and Christian Wipf for the technical support during manufacturing and RF measurement respectively, and the partial financial and technical support provided by Thales Alenia Space in Toulouse.

References

[1] I. De WOLF, *Reliability of MEMS*, Proc. of the 7th Int. Conf. on Thermal, Mechanical and Multiphysics Simulation and Experiments in Micro-Electronics and Micro-Systems (EuroSime), pp. 1–6, 2006

[2] M. KAYNAK, *et al.*, *BiCMOS embedded RF-MEMS switch for above 90 GHz applications using backside integration technique*, Electron Devices Meeting (IEDM), 2010 IEEE International, pp. 36.5.1–36.5.4, 6-8 Dec. 2010

[3] M. KAYNAK, *et al*., *RF-MEMS switch module in a 0.25 μm BiCMOS technology*, Silicon Monolithic Integrated Circuits in RF Systems (SiRF), IEEE 12th Topical Meeting, pp. 25–28, 16-18 January, 2012

[4] M. KAYNAK, *et al*., *Packaged BiCMOS embedded RF-MEMS switches with integrated inductive loads*, Microwave Symposium Digest (MTT), IEEE MTT-S International, pp. 1–3, 17-22 June 2012

[5] N. TORRES MATABOSCH, *et al.*, *Accurate and versatile. equivalent circuit model for RF-MEMS circuit. Optimization in BiCMOS. technology*, Microwave Integrated Circuits Conference (EuMIC), European, October, 2012.

[6] O. VENDIER, *RF-MEMS for space applications*, Microwave Integrated Circuits Conference (EuMIC), European, RF-MEMS for Mm-wave Reconfigurable ICs Workshop, November 2012.

[7] N. TORRES MATABOSCH, *et al*., *Estimation of RF performance from LF measurements: Towards the design for reliability in RF-MEMS*, Microelectronics Reliability, **52**(9–10), pp. 2310–2313, September–October, 2012

[8] G.M. REBEIZ, RF MEMS: Theory, Design, and Technology, New York: Wiley, pp. 87–104, 2003.

Design and Validation of RF-MEMS Wide Band Phase Shifters in Harsh Environments

Alexandre HARCK[1], Pierre BLONDY[1],
Sylvie FARGEOT[2], Serge VILLERS[2]

[1]XLIM–UMR CNRS n°7252, 123, Avenue Albert Thomas
87060 Limoges Cedex, France
E-mail: alexandre.harck@xlim.fr
[2]Astrium SAS, B.P. 20011, 33165 St. Médard en Jalles Cedex, France

Abstract. This paper describes progress towards the fabrication of 2.5GHz integrated MEMS switched line phase shifters. PCB fabricated phase shifter is presented in a first part and MEMS integration on this type of board is shown. Is can be seen that polymer flip-chip bonding of RF-MEMS is feasible and low loss MEMS switches can be successfully integrated.

1. Introduction

Telemetry on space launch vehicle is one of the most important functions that allowing for precise and efficient control of flight parameters. The required antennas for the remote operation of these systems have to be integrated very close to the outside of the space vehicle, and are therefore exposed to harsh environments encountered by the vehicle. During the flight, it is necessary to know the behavior of the different parts of the space launcher. Telemetry is used to transmit all information via a radio link between the launcher and the ground. The signal can be transmitted via electronically steerable antennas since this type of antenna provides appropriate directivity and optimum robustness against interference. Such antenna requires phase shifters based feeding network to adjust beam direction of the antenna, as shown in Fig. 1. Low loss, RF-MEMS based phase shifters, would be very well suited for this purpose, allowing the use of a single signal source, divided into several radiating elements. By passing signals through different delay lines, several delays (0°, 90°, and 180°) can be selected. This architecture provides a strong reduction in mass and volume, and relatively low energy consumption. It

also raises several challenges, like power handling, that needs to be optimized, and co-integration of RF-MEMS switches on printed circuit board devices.

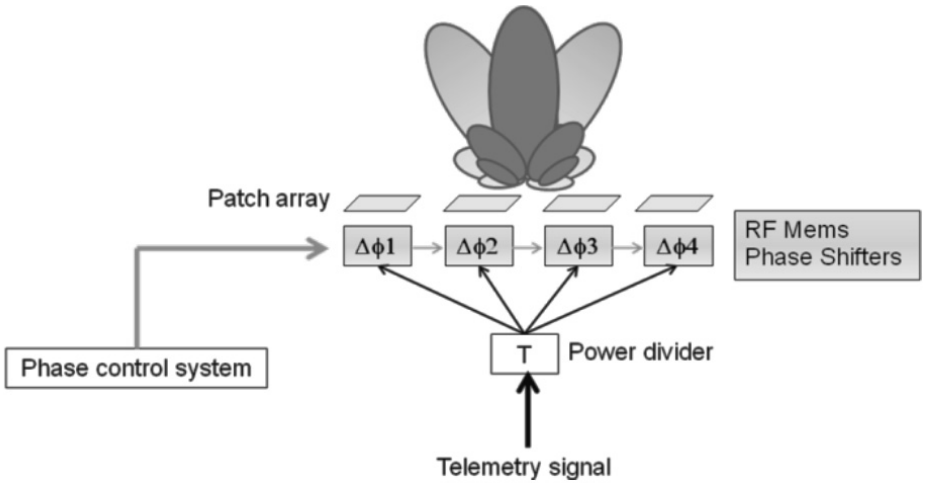

Fig. 1. Electronically steerable antennas SPNT (Single Pole N Throw) switch distribution.

2. Phase Shifter Description

According to the specifications, it is necessary to have three phase shift states for each antenna. Switched line based true time delay phase shifters (0°, 90°, and 180°) have been chosen for wideband operation. The line length and width have been computed using CAD based design package, using a 1.5 mm thick duroid (Er = 2.8) substrate. This result in relatively low loss transmission lines, well suited for the present application.

As shown in Fig. 2, switching between the different line lengths causes controlled delays at the output of the phase shifter. Since transmission lines have moderate loss, their impact on the overall phase shifter loss is very moderate, as shown in the following simulations.

Electromagnetic simulations are shown in Fig. 3, based on ADS Momentum. Transmission parameters are obtained for each delay line, ideally connected on the layout shown in Fig. 2. It can be seen from these simulations that reflection loss are very moderate, and that the corresponding insertion loss are less than 0.5 dB around 2.5 GHz.

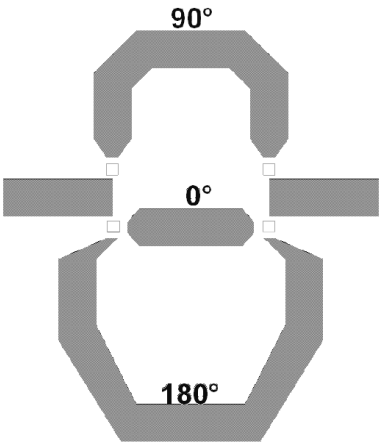

Fig. 2. Design of phase shifter switched lines (35mm×35mm).

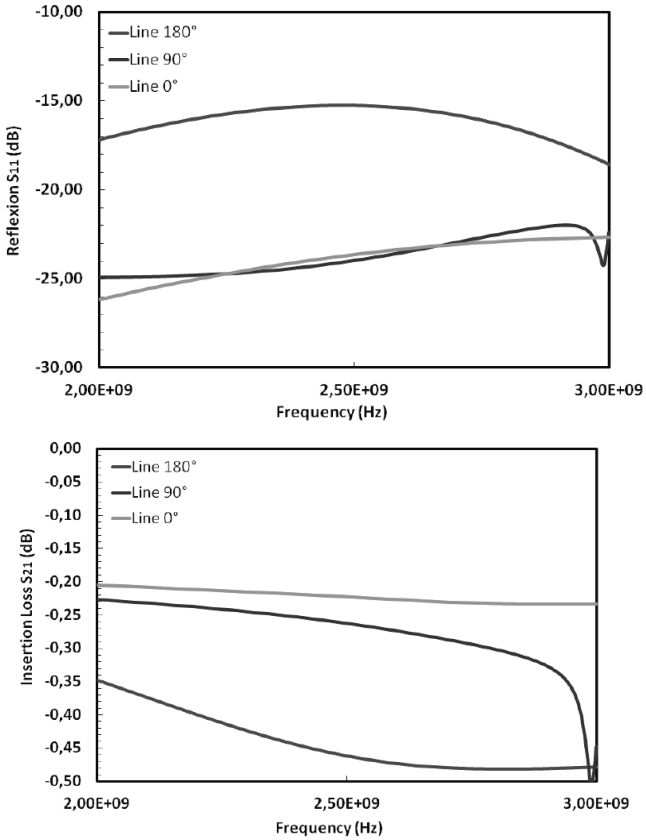

Fig. 3. ADS-Momentum simulations of the phase shifter.

A. RF-MEMS Switches

The RF-MEMS switches are placed on the phase shifter between the different switched lines, allowing the transmission of RF signal. This signal will be high power, but should not damage RF MEMS switches during data transmission. Therefore, different designs have been investigated, as shown in Fig. 4. 1-MEMS design is a simple SPDT switch, allowing for routing RF signals between two delay lines. A design with 2-MEMS has been fabricated and integrated in order to improve the current handling of the device. It is also dividing the insulation by 2, as the equivalent capacitance is doubled as switches are parallel. A design with 4 RF-MEMS, (2 in parallel and 2 in series) has also been fabricated to improve isolation, since it has capacitance equivalent to 1-MEMS design.

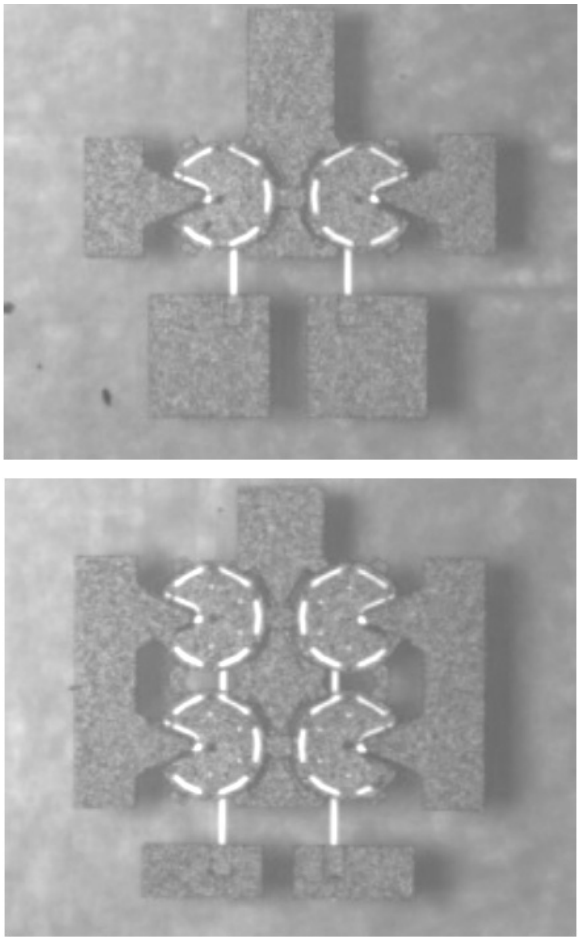

Fig. 4. Fabricaed MEMS designs (1mm*1mm).
1-MEMS (left side) and 2-MEMS (right side).

Simulations results are shown in Fig. 5 and confirm our expectations; the 4-MEMS design is equivalent to 1-MEMS design, and off-state capacitances are almost identical, with slight difference due to design differences. For 2-MEMS design, there is an expected difference of 6 dB taking into account the single capacitance. The simulated insertion losses are less than 0.2 dB (not taking the contact resistance into account) and minimized up to 5 GHz.

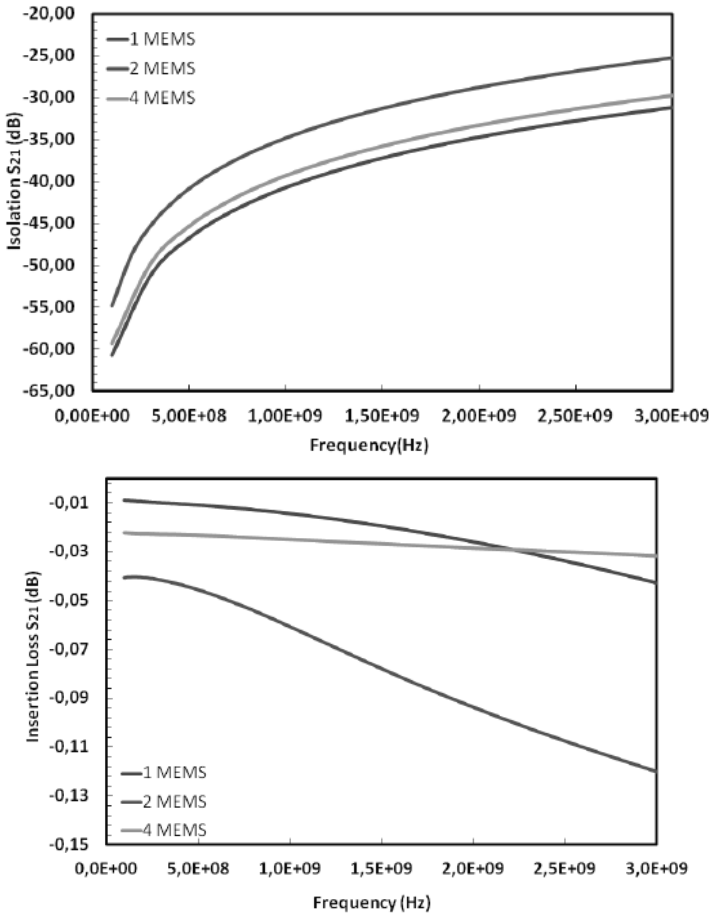

Fig. 5. ADS-Momentum simulations of RF-MEMS switches

3. Manufacturing

A. RF-MEMS

The superposition of thin layers of different materials is used to manufacture the switches. For this, photolithography masks are necessary to keep only the design of the component. Its structure is kept simple, a first metal electrode provides the

actuating and bias lines then, sacrificial layers allow to suspend the final structure, and finally a second metal layer which transmits the RF signal through its movable part is added (Fig. 6).

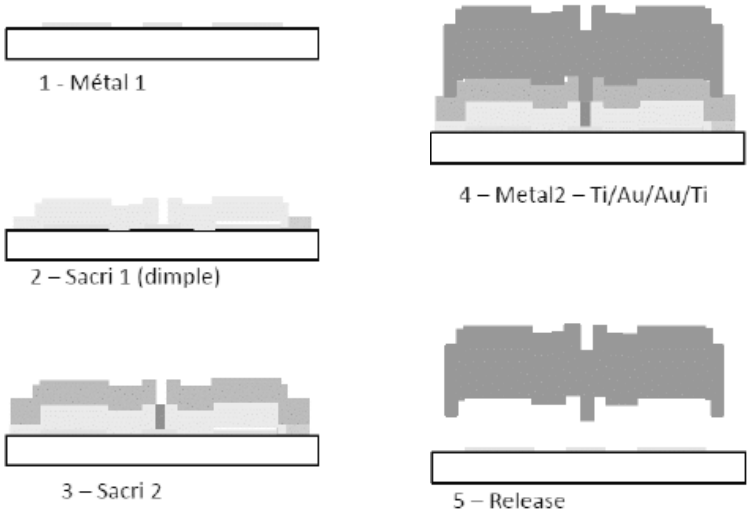

Fig. 6. Manufacturing of RF-MEMS.

B. Fabrication of the Switched-Line Phase Shifter

For the phase shifter, wet etching process technique was chosen because it allows a neat and clean etching. To etch the phase shifter, photolithography method has been used. This protects the parts that want to keep, and etch the rest of the substrate Fig. 7.

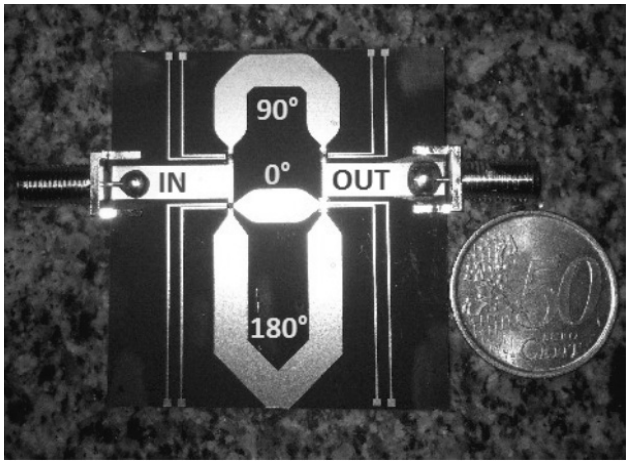

Fig. 7. Microphotograph Fabricated phase shifter.

The disadvantage of this method is over-etching that it is necessary to take into account when making masks; in general it is about the thickness of metallization.

C. Integration of RF-MEMS

Once the circuit made, the RF-MEMS switches are integrated on the substrate. For this, the flip-chip technique has been used. The RF-MEMS switch is mounted towards the membrane substrate. To realize this, it is necessary to use a polymer ring. This ring is used to suspend the component, and prevent the flow of the conductive paste that may short-cut the phase shifter, lines (see Fig. 8). Then, with the help of a pick & place machine, it is possible to place with enough accuracy the glue and switches onto the phase shifter. A vacuum oven curing removes binders and polymerizes glue, thereby welding the switch with the lines of the phase shifter.

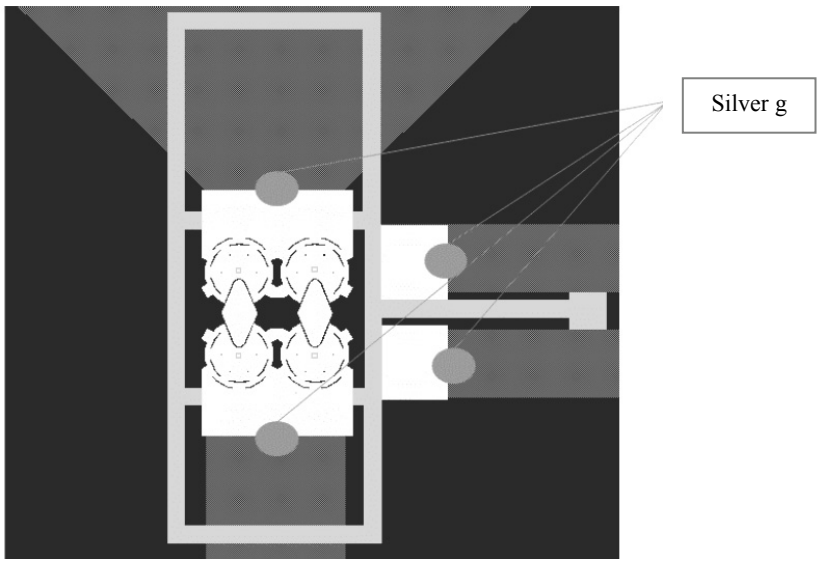

Fig. 8. MEMS switch flip-chip mounting.

4. Test of the Packaged Flip-Chipped Switch

During the manufacturing, it is necessary to pay attention to the resins and solutions used. A desorption step is necessary in order to not pollute MEMS contacts. First, a simple packaging with a resin has highlighted an increase in resistance, (Fig. 9). This is due to the desorbing of the resin during the firing in the oven.

The S_{21} parameters without encapsulation have good transmission while with encapsulation the signal is attenuated. This test confirms a risk of pollution as

possible in the flip-chip or encapsulation. Results with low outgassing materials will be shown at the conference.

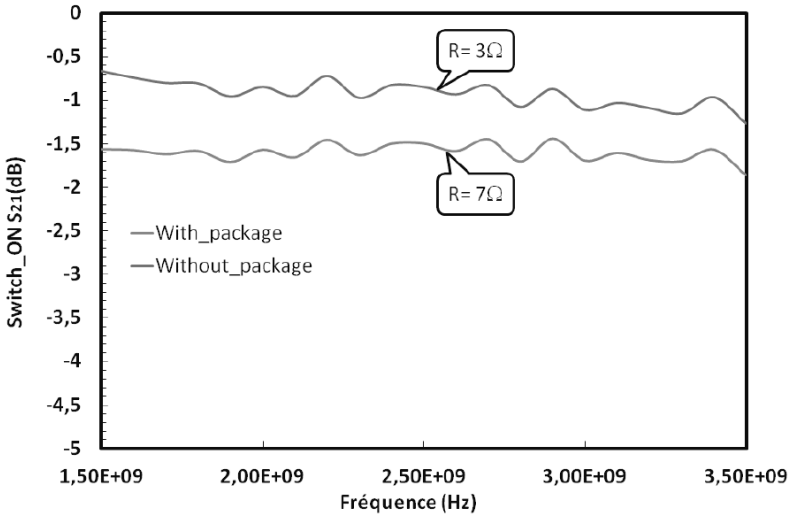

Fig. 6. Measured measurements S_{21}.

5. Conclusions

This paper reports progress towards the integration of RF-MEMS switches on PCB-like substrates. Flip-chip mounting of the devices permit to achieve low complexity, high performances phase shifters to be built. Moreover, flip-chip mounting needs improvement but offers an opportunity for encapsulation RF-MEMS switches at very low cost.

Acknowledgements. The authors wish to thank EADS Astrium Aquitaine for the financial support of this work.

References

[1] P. CHAUVEAU, P. BLONDY, S. FARGEOT, *Etude de la tenue de composant MEMS-RF à l'environnement mécanique sévère d'un lanceur spatiale*, 2009.

MEMS-Based Adjustable High-Q E-Plane Filters

Fabrizio GENTILI[1], Valeria NOCELLA[1], Luca PELLICCIA[2],
Fabrizio CACCIAMANI[1], Paola FARINELLI[2], Roberto SORRENTINO[1]

[1]DIEI, University of Perugia, Perugia, Italy
[2]RF Microtech Srl, Perugia, Italy

Abstract. This paper presents a new concept for the design of high-Q bandpass filters with fine-tuning compensating for small deviation of their nominal response due to manufacturing tolerances and temperature variations. Discrete frequency steps are realized using a rectangular waveguide resonator loaded with a reconfigurable E-plane circuit. Ohmic MEMS switches are placed along thin E-plane metal strips so as to modify the TE101 mode resonant frequency, thus the central frequency of the filters. As an example, in a 10 GHz resonant cavity frequency steps of 0.1% can be obtained. High Q-factors are maintained if low loss substrates are used. Preliminary simulations results are reported for both an X-band and a K-band cavity.

Key words: *bandpass filter; high-Q; MEMS; tunable filter; waveguide filter.*

1. Introduction

In recent years many techniques have been proposed to realize tunable bandpass filters for size and mass minimization of the front-ends.

Similar techniques can be adopted to realise filters with an adjustable response, thus a fine-tuning. Their aim is to compensate for tolerances of the realization process (machining and assembling) and temperature changes that may cause a drift of the filter response.

An acceptable trade-off among tuning capabilities, high unloaded Q, low-cost and small size, must be taken into account as a figure of merit for such techniques. For instance, magnetically tunable filters show wide tuning ranges and high Q, but are bulky and consume considerable DC power [1]. Tunable filters realized on planar technology based on RF MEMS [2] or ferroelectric components [3] offer compact size, fast tuning speed and wide tuning range, but limited Qs (< 300). Higher Qs (500-1500) can be reached using evanescent-mode cavities [4] or dielectric-loaded resonators [5], but such solutions require customized MEMS devices such as accurate varactors or movable membranes.

As is well known, RF MEMS are an attractive technology for microwave

applications thanks to their low insertion loss, low power consumption, low cost and compact size [6]. High-Q tunable filters can be obtained by suitably combining RF MEMS and high-Q cavity resonators. In [7] a MEMS varactor has been used in a ridge-loaded cavity at 5 GHz to tune its resonant frequency resulting in a (measured) Q above 500 and a tuning range up to 10%.

A new tuning concept for high-Q tunable bandpass filters employing ohmic cantilever RF MEMS switches has been patented in 2010 [8] and the first experimental results with real MEMS in [9] showed Qs around 1000.

Another MEMS-based tuning approach for waveguide filters was proposed by the same authors in [10] showing similar performances.

A new concept of adjustable bandpass filters leading to very high Qs (> 1000) is proposed in this paper. The filter is based on rectangular waveguide resonators loaded with thin E-plane metal strips on a low-loss substrate. Ohmic RF MEMS switches are used to modify the lengths of the different metal strips so as to digitally change the resonant frequency of the fundamental TE101 mode, thus the filter passband frequency. In [12] this concept was employed to move the centre frequency of a filter thus realising a reconfigurable response.

The main advantages of such a solution are the several small frequency steps that can be obtained, the high-Q (> 1000) in all states and the simple design and fabrication leading to a potentially low-cost manufacturing. The discrete fine tuning can be used in order to compensate for undesired filter response changes due to tolerances of manufacturing process and temperature sensitivity.

To illustrate and validate the proposed tuning principle, a resonant cavity at X-band has been designed and simulated with equivalent models for the MEMS, showing very satisfactory and promising results.

2. The Tuning Principle

Two kinds of rectangular waveguide sections loaded with E-plane metal septa patterned on a low-loss and low-permittivity substrate are depicted in Fig. 1.

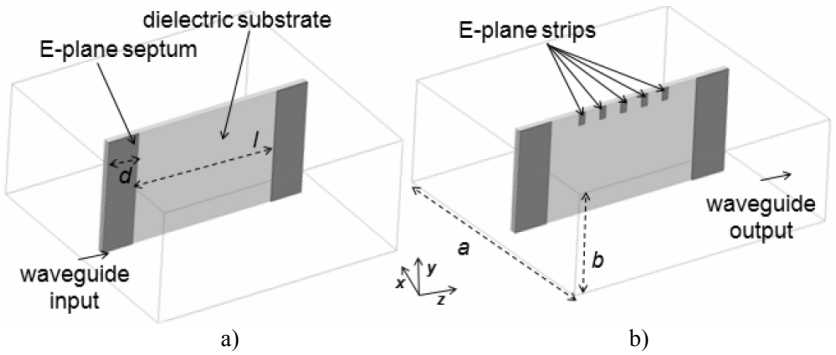

Fig. 1. Conventional E-plane resonator (a), strip-loaded E-plane resonator (b).

The resonator of Fig. 1a consists of a waveguide section comprised by two E-plane septa of length *d.* The latter determines the input (output) coupling between the TE10 mode of the guide and the TE101 resonant mode of the resonator (*i.e.* an inductive coupling), while the distance *l* between the septa determines the resonant frequency of the fundamental TE101 mode [11].

In Fig. 1b additional E-plane conductive thin strips are placed between the septa and used to change the resonant frequency of the TE101 mode, in a similar way as in [10]. We call the structure in Fig. 1b a strip-loaded E-plane resonator. The thin strips behave as metallic tuning screws located in the region of the E-field maximum of the resonant mode: the longer the strips the lower the resonant frequency [13].

The strip-loaded E-plane resonator of Fig. 1b is amenable to tuning as illustrated in Fig. 2. Here, MEMS switches are placed along the thin strips very close to the short-circuited ends (i.e. close to the top waveguide broad wall).

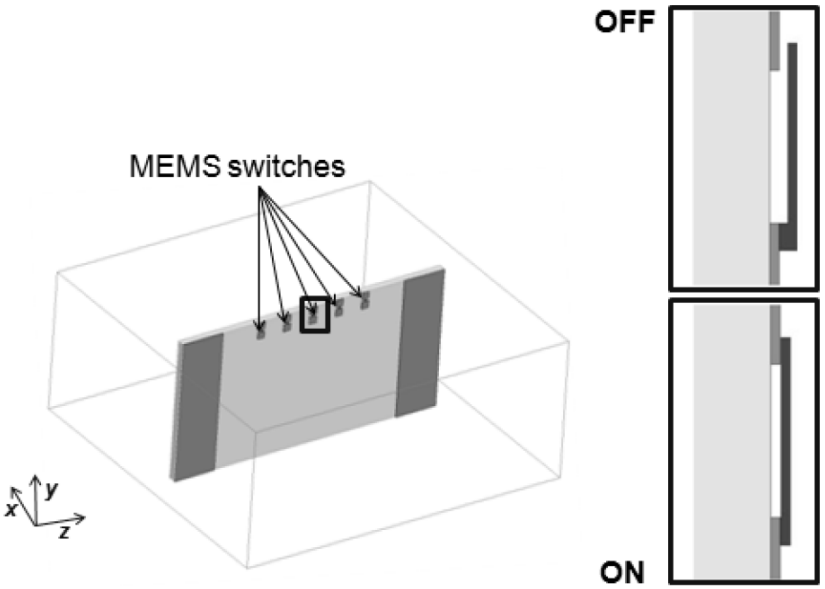

Fig. 2. Tunable strip-loaded E-plane resonator using MEMS swithes.

The MEMS switches can be realized as ohmic cantilever switches. In the case of the RF switches fabricated at FBK (Fondazione Bruno Kessler) foundry in Trento (Italy), they consist of 110 μm wide and 170 μm long gold thin beams suspended above an interrupted line and a DC actuation pad underneath the beam. In the on-state (with roughly 50 V DC voltage) the switch is closed and can be modelled as a very low series resistance (*Ron* ~ 1 Ω), while in the off-state the switch is open and can be modelled as a low series capacitance (*Coff* ~ 10 fF). Such approximations are valid up to 25 GHz [6].

The tuning principle of Fig. 2 is as follows. We refer to the fundamental TE101 resonant mode. When all the switches along all the strips are closed (state 11111 in Fig. 3a), the strip are continuous conducting lines and the E-field in the central longitudinal plane (*yz* in Fig. 3) is confined below them as in the case of Fig. 2, thus the resonant frequency is lowered. When instead all the switches are open (state 00000 in Fig. 3b), the E-field goes through the interrupted conducting lines, thus the mode perturbation is reduced and the resonant frequency is increased with respect to previous case. As a result, the resonant frequency is lowered by switching on the MEMS.

The entity of the frequency shift can be controlled by choosing the length and the number of the strips, as well as the distance between them. Intermediate frequency states are allowed switching only some strips: e.g. in the state 00001 only one strip is closed.

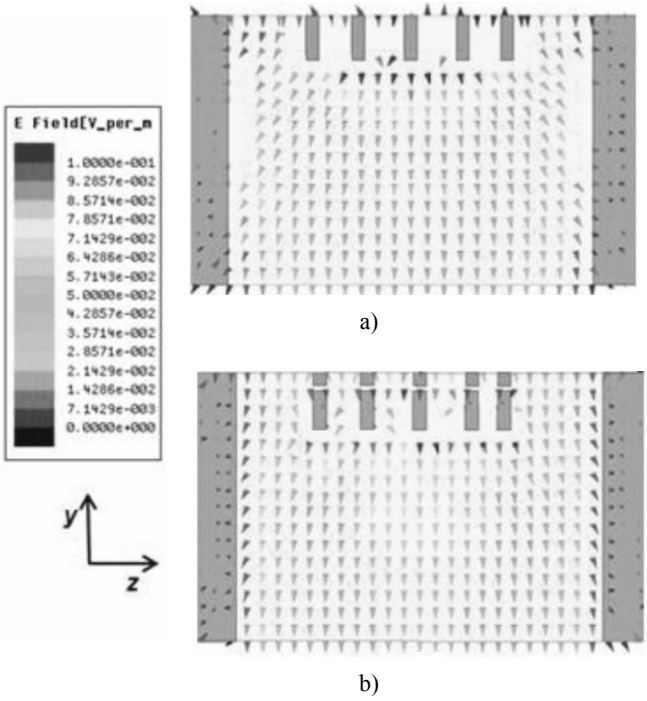

a)

b)

Fig. 3. E-field behavior when the MEMS is on (a), E-field behavior when the MEMS is off (b) of the fundamental resonant mode of the resonator in Fig. 2.

3. Tunable Single-Resonator

The practical design of a MEMS-based tunable strip-loaded E-plane resonator is illustrated in this section. Two resonant frequencies are considered, in X-band (WR90 standard waveguide) and in K-band (WR45 standard waveguide).

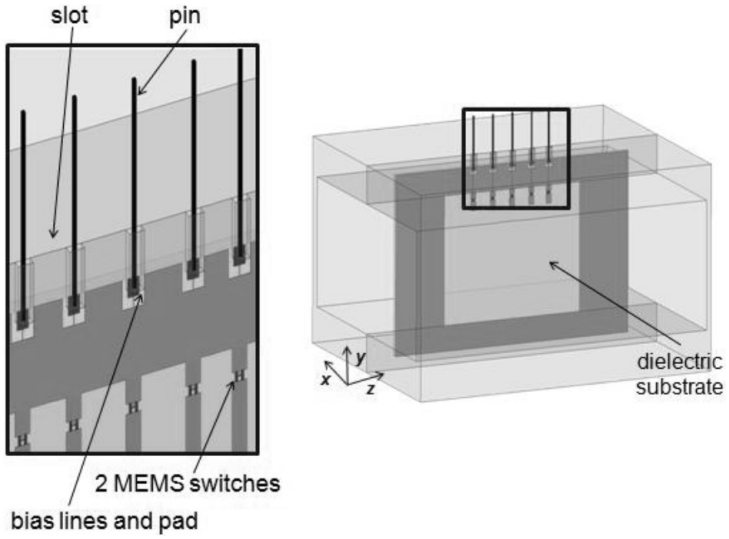

Fig. 4. HFSS models for a feasible MEMS-base tunable strip-loaded E-plane resonator: the MEMS and the strips are on the metal septa substrate.

Referring to Fig. 4, the E-plane circuit pattern (*i.e.* septa and strips) and the MEMS switches are realized on a 500 μm thick quartz substrate using gold. The strips are 500 μm wide. Quartz is preferred over silicon because of its lower permittivity (3.78) and tanδ (1·10-4).

In the model of Fig. 4 the quartz protrudes in the waveguide broad wall in order to allow the connection of the MEMS bias lines to the external DC circuitry. The 10 μm wide bias lines are realized in high resistivity polysilicon [6] and they are placed underneath the substrate metallization (see Fig. 4). The slots opened in the waveguide broad wall are thin enough not to interrupt the flowing current (that is zero in the middle of the transverse plane for the TE101 mode), thus preventing or minimizing undesired radiation.

Two ohmic cantilever MEMS switches have been considered in parallel in each strip (*i.e.* 10 switches in each resonator), thus the equivalent series resistance is roughly 0.5 Ω in each strip.

The structure has been carefully modelled by HFSS including the bias lines, the lossy substrates and the actual material conductivity.

4. Simulation Results

Preliminary simulation results of the tunable cavities in X- and K-band are here presented. Each cavity presents five MEMS switches that can assume two different states, therefore the number of combinations is 32 (*i.e.* 25). However some combinations are equivalent to each other, therefore the number of different states reduces to 20. In the following tables the results obtained for the X-band and the K-

band cavity are shown. Simulations were carried out considering silver plating on the internal walls.

Table 1. Comparison between the starting state (00000) and the next one (00001) for X-band cavity

STATE	Q	Res. Freq.	Δf
00000	3600	10 GHz	9MHz
00001	3500	9.991 GHz	

Table 2. Comparison between the first (00000) and last state (11111) for X-band cavity

STATE	Q	Res. Freq.	Freq. Range
00000	3600	10 GHz	64MHz
11111	3400	9.936 GHz	

A total frequency shift of 0.64% is observed in the X-band cavity. The step between a state and the next one is not constant in this case where all the five lines were identical and equidistant. Anyway it can be chosen as desired by opportunely design the length and position of the lines.

Table 3. Comparison between the starting state (00000) and the next one (00001) for K-band cavity

STATE	Q	Res. Freq.	Δf
00000	2580	20	50MHz
00001	2215	19.950	

Table 4. Comparison between the first (00000) and last state (11111) for K-band cavity

STATE	Q	Res.Freq.	Freq. Range
00000	2580	20	250MHz
11111	1690	19.750	

A total frequency shift of 250 MHz (1.25%) is obtained for the case of a K-band cavity. Simulation also shows that the Q-factor is maintained to high values (1690). This means that such cavities can be used as building blocks for designing filters with low losses and built-in fine-tuning.

The steps □f here considered are comparable to the frequency shifts deriving from a mechanical tolerance of +/- 20um, or a temperature drift of 80°C for a component in aluminium.

5. Conclusions and Future Work

A new concept has been proposed for high-Q MEMS-based adjustable bandpass filters with small steps in frequency. A waveguide resonator is employed consisting

of a rectangular waveguide section comprised between two metallic E-plane septa and loaded with thin E-plane conductive strips on a low-loss substrate. The thin strips are connected to the top waveguide wall by RF MEMS switches. In this manner, the TE101 mode resonant frequency can be modified depending on the MEMS state. This tuning principle allows for a fine tuning to be realised which may result very useful for high frequencies where resonators size is particularly small and where compensation for manufacturing tolerance effects and temperature variations are necessary. High Q-factor is maintained over the tuning range making this approach suitable for realising low loss filters.

The advantage of this approach over classical tuning screws is that small frequency steps are achievable in a controlled and repeatable way. Fine-tuning is still feasible even in cases where it would be impossible with screws for dimensional issues. Moreover, being the driving of the switch entirely electronic this approach is amenable to remote control.

An adjustable E-plane filters with real ohmic cantilever MEMS switches will be designed and manufactured in the next months employing ohmic switches fabricated at FBK foundry (Fondazione Bruno Kessler, Trento) [6].

References

[1] J. UHER and W.J.R. HOEFER, *Tunable microwave and millimeter-wave bandpass filters*, IEEE Trans. Microwave Theory and Techniques, **39**(4), pp. 643–653, April, 1991.

[2] A. OCERA, P. FARINELLI, P. MEZZANOTTE, R. SORRENTINO, B. MARGESIN, F. GIACOMOZZI, *A novel MEMS-tunable hairpin line filter on silicon substrate*, 36th European Microwave Conference, Manchester September, 2006.

[3] S. COURREGES, YUAN LI, ZHIYONG ZHAO, KWANG CHOI, A. HUNT, J. PAPAPOLYMEROU, *Ferroelectric Tunable Bandpass Filters for Ka-Band Applications*, Proceedings of 38th Microwave Conference, pp. 55–58, Amsterdam, 27-31 October, 2008.

[4] S.-J. PARK, I. REINES, C. PATEL and G. REBEIZ, *High-Q RF-MEMS 4-6 GHz Tunable Evanescent-Mode Cavity Filter*, IEEE MTT-S Int. Microwave Symp. Dig., Proceedings of workshop WFD, pp. 1145–148, 7-12 June, 2009.

[5] D.W. WINTER and R.R. MANSOUR, *Tunable Dielectric Resonator Bandpass Filter with Embedded MEMS Tuning Elements*, IEEE Trans. Microwave Theory & Tech., **55**(1), pp. 154-159, January, 2007.

[6] P. FARINELLI, F. GIACOMOZZI, G. MANNOCCHI, R. MARCELLI, B. MARGESIN, P. MEZZANOTTE, S. Di NARDO, P. RUSSER, R. SORRENTINO, F. VITULLI, L. VIETZORRECK, *RF-MEMS SPDT Switch on Silicon Substrate for Space Application*, Silicon Monolithic Integrated Circuits in RF Systems, pp. 151–154, 8-10 Septtember, 2004.

[7] R. STEFANINI, M. CHATRAS, A. POTHIER, J.C. ORLIANGES, P. BLONDY, *High Q Tunable Cavity using Dielectric Less RF-MEMS Varactors*, Proceedings of the 39th European Microwave Conference, pp. 1744–1747, Rome, 29 September-1 October, 2009.

[8] P. LIGANDER, O. PERSSON, L. PELLICCIA, S. BASTIOLI, R. SORRENTINO, Patent Title: *An Electrcially Tunable Waveguide Filter and Waveguide Tuning Devices*, Int. Publication N.: WO 2012/016584 A1; International Application N.: PCT/EP2010/061218, International Filing Date: 2nd August 2010, International Publication Date: 9th February, 2012.

[9] L. PELLICCIA, F. CACCIAMANI, P. FARINELLI, P. LIGANDER, O. PERSSON, R. SORRENTINO, *High-Q MEMS-Tunable Waveguide Filters in K-band*, Proceedings of the 42nd European Microwave Conference (EuMC), Amsterdam, The Netherlands, 28 October – 2 November, 2012.

[10] L. PELLICCIA, P. FARINELLI, R. SORRENTINO, *MEMS-based High-Q Reconfigurable E-plane Filters*, Proceedings of the 41st European Microwave Conference (EuMC), Manchester, UK, 9-14 October, 2011.

[11] Yi-Chi SHIH, *Design of Waveguide E-Plane Filters With All-Metal Inserts*, IEEE Trans. Microwave Theory & Tech, **MTT-32**(7), pp. 695–704, July, 1984.

[12] L. PELLICCIA, V. NOCELLA, F. CACCIAMANI, F. GENTILI, P. FARINELLI, R. SORRENTINO, *Discrete-tunable High-Q E-plane Filters*, Submitted to the 43rd European Microwave Conference (EuMC), Nurnberg, Germany, 6-11 October, 2013.

[13] G. MATTHAEI, L. YOUNG, E.M.T. JONES, *Microwave Filters, Impedance Networks, and Coupling Structures*, Artech House, Norwood, MA, 1980.

An Accurate EM Modeling of 140 GHz BiCMOS Embedded RF-MEMS Switch

S. TOLUNAY[1], M. WIETSTRUCK[1], A. GÖRITZ[1],
M. KAYNAK[1] and B. TILLACK[1,2]

[1]IHP, Im Technologiepark 25, 15236 Frankfurt (Oder), Germany
Tel: (+49) 335 5625 487,
E-mail: tolunay@ihp-microelectronics.com
[2]Technische Universität Berlin, HFT4, Einsteinufer 25, 10587, Berlin, Germany

Abstract. An accurate 3D *electromagnetic* (EM) model for a 140 GHz BiCMOS embedded RF-MEMS switch in 0.13 µm technology is built up in Ansoft HFSS solver. The 3D EM solver allows defining the air cavity of the switch and the *back-end-off-line* (BEOL) oxide simultaneously in the same model, in contrast to 2.5D planar EM solvers. Using the developed model, RF behavior of the MEMS device in air and the routing layers in oxide can be simulated at the same time which is very important considering the very high frequency of operation. Furthermore, the process effects such as bending of the membrane can also be modeled by changing the initial gap in the simulator. The simulation results show the significant importance of the EM model of RF-MEMS switch at such highfrequency of operation.

Index Terms: RF-MEMS switch, 3D FEM, mm-wave, EM modeling.

1. Introduction

In the recent years, new generation communication system technologies demand not only miniaturization but also multifunctionality at the same time. In this point of view, RF-MEMS technology seems to be a promising option in order to add functionality to the RF systems. One of the most attractive RF-MEMS developments is in RF-MEMS switches. As a result of their low insertion-loss, high isolation, high linearity, near-zero power consumption and low fabrication cost, there is a growing interest in RF-MEMS switches for mm-wave frequency applications for the recent years [1].

EM modeling of RF-MEMS switches is performed mostly by using 2.5 D planar EM solvers where modeling of passive devices is very convenient and straightforward. However, most of the 2.5 D planar solvers have the limitation of

defining non-uniform dielectric planes in horizontal direction; means if the material between two metals is defined as a dielectric, it is the same dielectric everywhere in the same horizontal plane. Nevertheless, this is in contrast with the MEMS devices because the mechanical part of the MEMS devices are mostly in air but the anchors and routing layers are in a dielectric. Therefore, for high frequency EM simulation of RF-MEMS devices, a more careful modelling strategy is essential.

In this work, RF-MEMS switch embedded into BEOL of IHP`s 0.13 µm BiCMOS technology is designed and simulated using Ansoft HFSS 3 D FEM (Finite-Element-Method) solver at 140 GHz. The paper starts with the basic information about the technology and EM modeling strategy is given after that.

2. BiCMOS Embedded RF-MEMS Switch

RF-MEMS switch, embedded in IHP`s 0.25 µm BiCMOS technology, had been demonstrated before up to 140 GHz operating frequencies [2-3]. However, previous experiences have shown that the size of the RF-MEMS devices is getting the main limitation for higher frequencies, such as 140 GHz. Therefore, firstly the size of the RF-MEMS switch was shrunk and an accurate 3D EM model has been developed. BEOL metallization of 0.13 µm BiCMOS technology has 7 metal layers instead of 5 and the distances between the metals are also different compared to 0.25 µm BiCMOS technology [2]. Indeed, it is not possible to easily transfer the 0.25 µm RF-MEMS switch to 0.13 µm BiCMOS technology and some significant effort is necessary in order to optimize the switch at 140 GHz of operation.

A. RF-MEMS Switch Technology

The capacitive RF-MEMS switch is designed between Metal4 (M4) and TopMetal1 (TM1) of IHP`s 0.13 µm BiCMOS technology. Figure 1 shows the process integration scheme of the RF-MEMS switch. Similar to 0.25 µm BiCMOS technology, RF-MEMS switch in 0.13 µm BiCMOS technology consists of high-voltage electrodes (Metal 4), RF-signal line (M5) and movable membrane (TM1). The movable membrane is modeled as an AlCu layer that is stacked by TiN layers both on top and bottom.

The MIM capacitor which is used in contact region of the switch is formed on M5 in the 0.13 µm BiCMOS technology.

One of the main changes from 0.25 µm to 0.13 µm technology is the smaller dimensions of the switch. With the reduced size of the switch, mechanical properties like stiffness also changed. With the increase of the stiffness, actuation voltage also increased. Higher electrical resonance frequency is achieved as a result of decreased contact capacitance of the switch due to the reduced contact size of the switch which provides higher frequency of operation The RF performance of the switch is optimized at 140 GHz operating frequency.

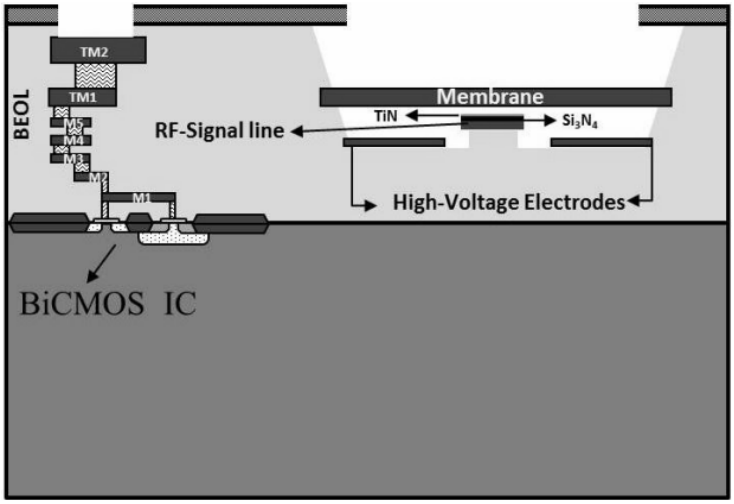

Fig. 1. Cross section of the 0.13 µm BiCMOS process, including embedded RF-MEMS switch.

B. EM Modeling

The limitation of the planar EM solvers is that the layers are defined infinite in horizontal directions. As the air cavity for released RF-MEMS devices in SiO_2 cannot be easily defined with planar EM solvers, all device including the anchors and routings is simulated in complete air or another dielectric environment. Such case might have less influence considering the operating frequencies less than 40 GHz. However, at 140 GHz, the anchors and the routing layers of the switch which are normally in the BEOL oxide has a significant effect on the overall performance of the RF-MEMS switch, considering the low resistive silicon substrate (50Ω-cm) below the RF-MEMS switch. Therefore there is a strong need to simulate intrinsic MEMS devices in air and other parts in BEOL oxide environment. The simulation setup in Ansoft HFSS for 140 GHz BiCMOS embedded RF-MEMS switch which considers the air cavity inside the BEOL oxide is shown in Fig. 2.

In 3D EM simulations the intrinsic part of the RF-MEMS switch can be simulated in air and the rest in oxide but there is still another limitation coming from the fabrication issues. For an accurate switch model in 3D EM solver, the contact parameters especially in down-state need to be precisely modeled. The contact capacitance of the switch depends on the membrane`s stress behavior in both up and down states and also on surface roughness in down state. In order to model the RF-MEMS switch in 3 D EM, the air capacitances of the switch in both states needs to be known. Therefore, the contact regio (Fig. 3) capacitances for up and down states, C_{up} and C_{down}, are measured and appropriate membrane position is formed with respect to the measured values.

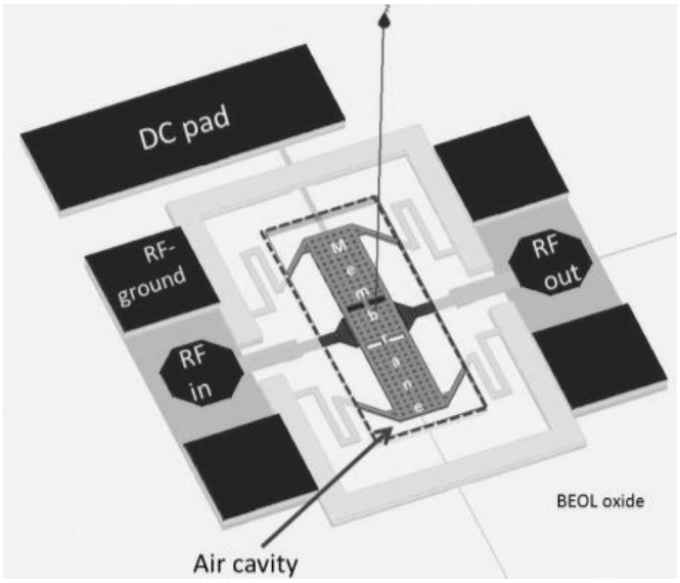

Fig. 2. Simulation setup in Ansoft HFSS for 140 GHz BiCMOS embedded RF-MEMS switch.

With the extracted contact air capacitances, which are measured as 15 fF and 90 fF for Cup and Cdown respectively, and known contact area, the distances between the membrane and TiN of the MIM capacitor on the RF-signal line are calculated for both states using the simple parallel plate capacitor equation. Calculated distances are then used in the EM model for the accurate modeling of the stressed membrane.

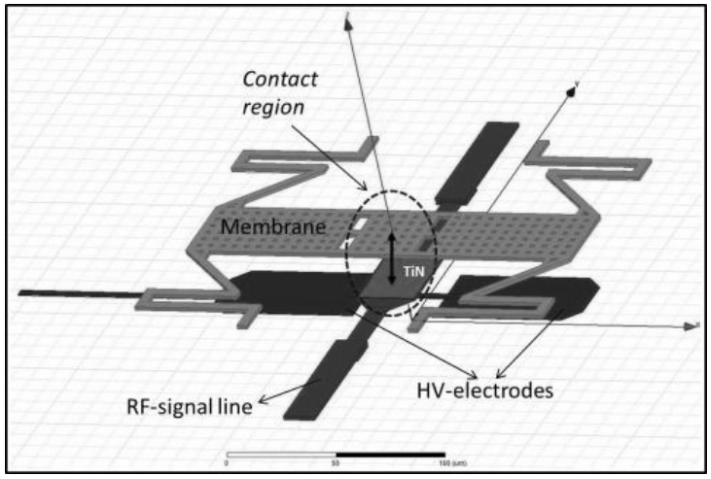

Fig. 3. Contact region of the RF-MEMS switch.

EM simulation results of the RF-MEMS switch for different contact air capacitances that change with different distances in the contact region are shown in Fig. 4. Each graph includes s-parameter results with the change of the membrane distance by 50 nm steps over 730 nm initial distance. The bold red and blue curves show the expected up and down state results, respectively. As it can be easily seen, the electrical resonance frequency of the switch is getting smaller with the decreased distance between membrane and MIM layer. For 140 GHz BiCMOS embedded RF-MEMS switch in 0.13 μm technology, insertion loss less than 2 dB and isolation better than 32 dB are achieved, including the RF measurement pads. The return loss for up-state is less than 25 dB at the interested frequency band, although it was not exactly optimized for 140 GHz.

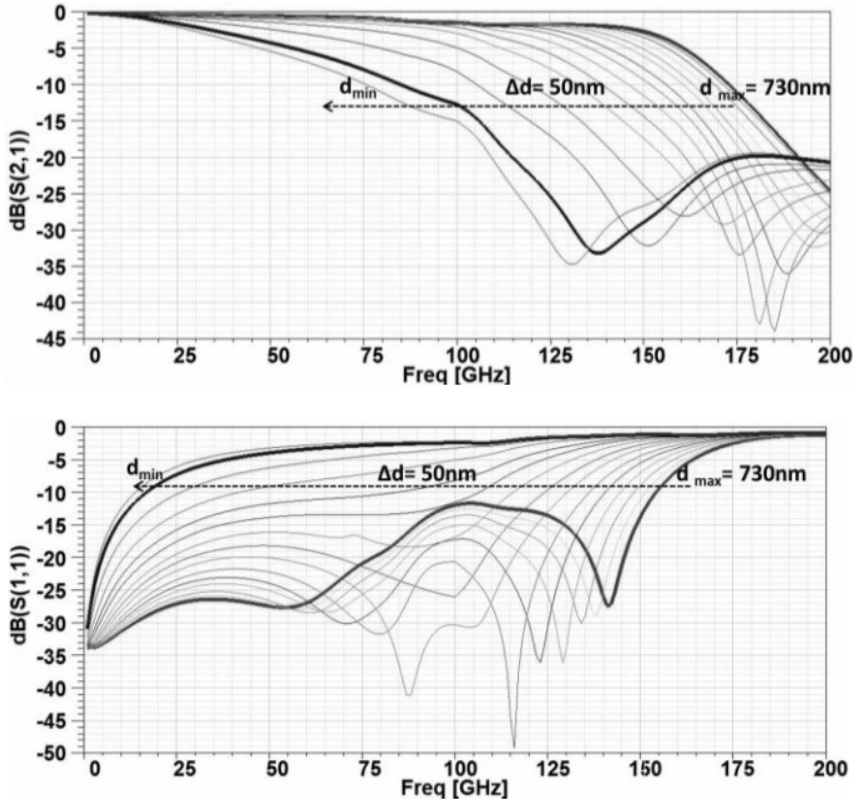

Fig. 4. Simulated RF performance of the RF-MEMS Switch for different contact region distances with the change of 50 nm in each step.

As mentioned before, in planar EM solvers, RF-devices cannot be simulated with the air cavity in SiO_2 because the layers are defined infinite in horizontal plane and at high frequencies the anchors and the routing layers of the RF-MEMS

switch which are normally in the BEOL oxide has a significant effect on the overall performance of the RF-MEMS switch. In order to compare the RF performance of the switch in two different environment conditions, RF simulations of the switch are also done when all parts of the switch, including the parts normally in BEOL oxide, are in air.

Figure 5 and 6 show the comparison of the RF performances of the switch for two different environment conditions. The bold red and blue curves show the RF performance of the switch when it`s all in air and RF performance of the switch when the anchors and the routing layers of the RF-MEMS switch are in the BEOL oxide, respectively. As two environment conditions are compared, in the up-state RF-MEMS switches at high frequencies have quite different insertion and return losses when in the down state they have quite similar isolations. In both environment conditions contact region is simulated in air. Similar RF performances in down-state are results of domination of the down-state contact capacitance, Cdown, when compared with the other parts of the switch. Different RF behaviors in up-states are because of the domination of the anchors and routings of the switches, as compared to Cup, that are simulated in oxide or in air. Comparison of the RF performance of the switches shows that at high frequencies depending on the simulation environment different results in down-state can be obtained. Indeed, an accurate EM model for 140 GHz RF-MEMS switch needs to consider the anchors and the routing layers in BEOL oxide.

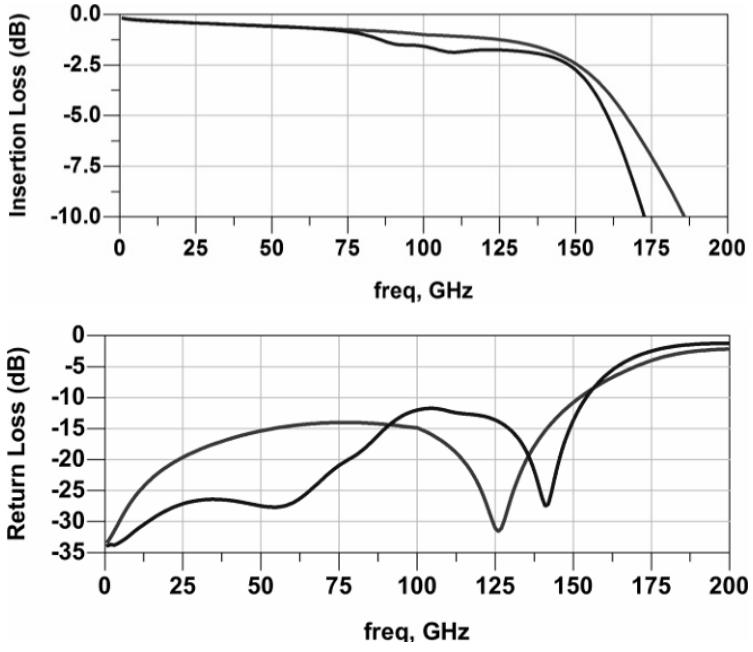

Fig. 5. Simulated RF performance of the RF-MEMS Switch when all is in air (red) and when the anchors and the routing layers are in the BEOL oxide (blue), in up-state.

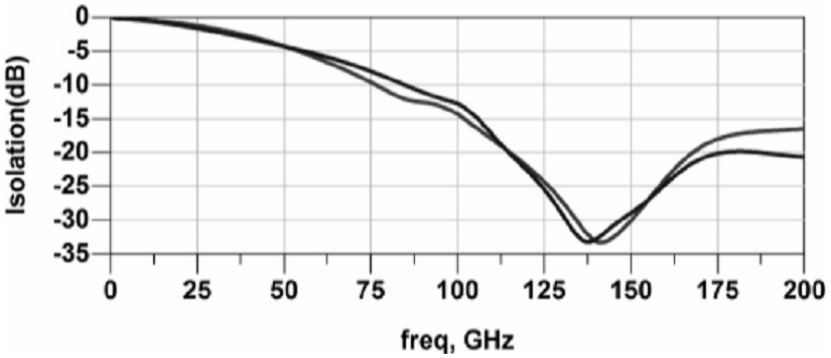

Fig. 6. Simulated RF performance of the RF-MEMS Switch when all is in air (red) and when the anchors and the routing layers are in the BEOL oxide (blue), for isolation in down-state.

Further optimization on the return loss of the RF-MEMS switch will also decrease the insertion loss of the switch at 140 GHz. As mentioned before, the results in Fig. 4 includes the significant pad parasitics which needs to be considered especially at 140 GHz. Figure 7 shows the RF performance comparisons of the switches with and without measurement pads for insertion losses, when the return losses are excluded. Insertion loss reduced from 2 dB to 1.4 dB at 140 GHz.

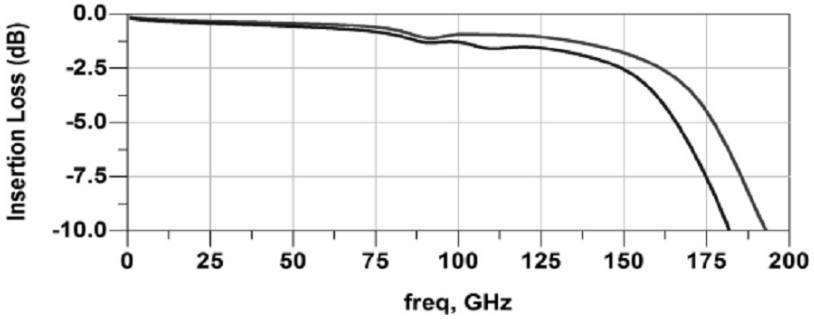

Fig. 7. Simulated RF performance of the RF-MEMS Switch with (blue) and without (red) measurement pads, for insertion loss in up-state.

3. Conclusion

3D EM modeling for 140 GHz BiCMOS embedded RF-MEMS switch in 0.13 µm technology was demonstrated. As stressed membrane gives complexity for EM modeling, the switch was successfully modeled using measurement supported 3 D EM model for RF simulations. 140 GHz BiCMOS embedded RF-MEMS switch which considers the air cavity inside the BEOL oxide is also compared with the case of planar EM solvers as all switch is simulated in air. Also reduction of 30% in insertion loss is achieved by de-embedding the RF pads.

Acknowledgements. This work was supported by the European Commission under the contract No. 257335-FLEXWIN (www.flexwin.eu) and by the European Commission under the contract No. 288531-NANOTEC (www.project-nanotec.com).

References

[1] G. REBEIZ, Microwave Magazine, IEEE, **2**(4), pp. 59–71, 2001.
[2] M. Kaynak, *et al*., IEDM Technical Digest, pp. 1–4, December, 2009.
[3] M. Kaynak, *et al*., IEDM Technical Digest, pp. 832–835, December, 2010.

Frequency and Bandwidth Control of Switchable Icrostrip Bandpass Filters using RF-MEMS Ohmic Switches

Zabdiel BRITO-BRITO[1], Ignacio LLAMAS-GARRO[2], Lluis PRADELL[3], Flavio GIACOMOZZI[4], Sabrina COLPO[4]

[1]ITESO, Jesuit University of Guadalajara, 44604 Jalisco, México
[2]Centre Tecnologic de Telecomunicacions de Catalunya (CTTC), 08860 Barcelona, Spain
[3]Technical University of Catalonia (UPC), 08034 Barcelona, Spain
[4]Fondazione Bruno Kessler (FBK), 38123 Povo Trento, Italy

Abstract. In this paper a reconfigurable bandpass filter is designed using ohmic-contact cantilever-type Micro Electro Mechanical Systems (MEMS) switches. The filter can switch between two different states with a center frequency tunable range of 13% in C band. The topology allows achieving two accurate center frequencies, each associated with a precisely defined bandwidth, using six MEMS ohmic-switches. The design carefully takes into account the external quality factor for both filter states to ensure a good impedance match at each frequency. The two sets of coupling coefficients and resonator lengths implemented with the MEMS ohmic switches originate the bandwidths and center frequencies required by design specifications. The filter is designed to have center frequencies of 5.5 and 6.2 GHz, with a fractional bandwidth (FBW) of 5 and 3%, respectively. Filter specifications were successfully met with the proposed topology. The filter was fabricated on a quartz substrate and measured responses are in good agreement with simulations.

1. Introduction

Reconfigurable filters are a key component in compact communication systems, because they allow selecting different operating bands with a single filter by using integrated tuning elements. Another advantage of the reconfigurable filter is to reduce the total volume of the system. A recent trend in reconfigurable filters is to obtain devices that reconfigure their parameters independently: center frequency [1, 2], bandwidth [3, 4], center frequency and bandwidth [5, 6] or selectivity [7, 8]. Designed filters with MEMS switches include monolithically integrated [9, 10] and planar circuits with integrated commercial MEMS switches [11].

The goal of this work is to design a precise frequency and bandwidth

controllable filter topology using MEMS switching elements. This paper presents a bandpass filter designed to produce two fractional bandwidth (FBW), 5% for a low frequency state and 3% for a high frequency state with a center frequency tuning range of 13% in C band. The filter was designed using six ohmic-contact cantilever-type MEMS switches that control transmission line extensions to achieve reconfiguration.

The center frequency is controlled by adjusting the length of the resonators. The bandwidth is controlled by adjusting the coupling between resonators. The external quality factor Qe is selected using MEMS ohmic-switches to maintain a proper input/output coupling for both states of the filter. The filter is able to reconfigure center frequency and bandwidth accurately.

This paper is divided in five sections. Section 2 contains a discussion of the proposed filter topology, describing how the filter design parameters, center frequency and bandwidth were controlled. Section 3 discusses the MEMS technology used to implement the filter on a quartz substrate. Section 4 discusses simulated and measured responses of the filter. Finally section 5 gives an overall conclusion of this work.

2. Filter Design

Table 1 shows the specifications of the two filter states. Each of the states is defined by three parameters: the external quality factor Qe which relates the input and output coupling of the filter, the coupling coefficient K between the resonators, and the length of the resonator [12]. To find optimum filter layout using the ADS/Momentum simulator, the coupling between feed lines of the filter and the first or last resonator are calculated in order to match the theoretical values of Qe. Similarly, by simulating the coupling between resonators, the values of K are found using the well-known methods in [12].

Table 1. Filter specifications

	Center Frequency	Fractional Bandwidth
Low frequency state	5.5 GHz	5 %
High frequency state	6.2 GHz	3 %

The topology of the filter, shown in Fig. 1, is based on parallel coupled transmission lines [12]. The topology uses six transmission line extensions switched using ohmic-contact cantilever-type MEMS switches, which se up precisely the three design parameters required to produce the two states of the filter specified in Table 1.

In this topology all the MEMS ohmic-switches are of to produce the high frequency state, and are on for the low frequency state.

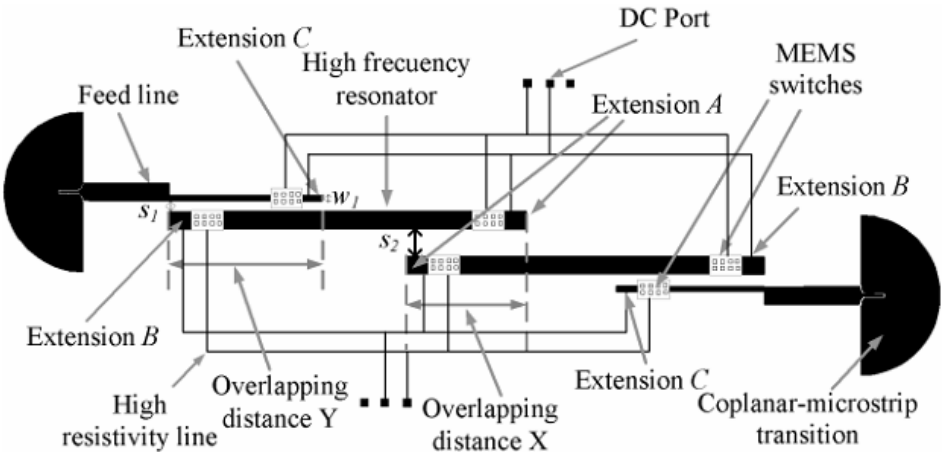

Fig. 1. Switchable bandpass filter topology.

Figure 2 shows the relationship between the external quality factor *Qe* and the overlapping distance Y between the input line and a resonator (see Fig. 1). The values were simulated using ADS/Momentum and considering fixed values for the spacing S1 and the width w of the input line.

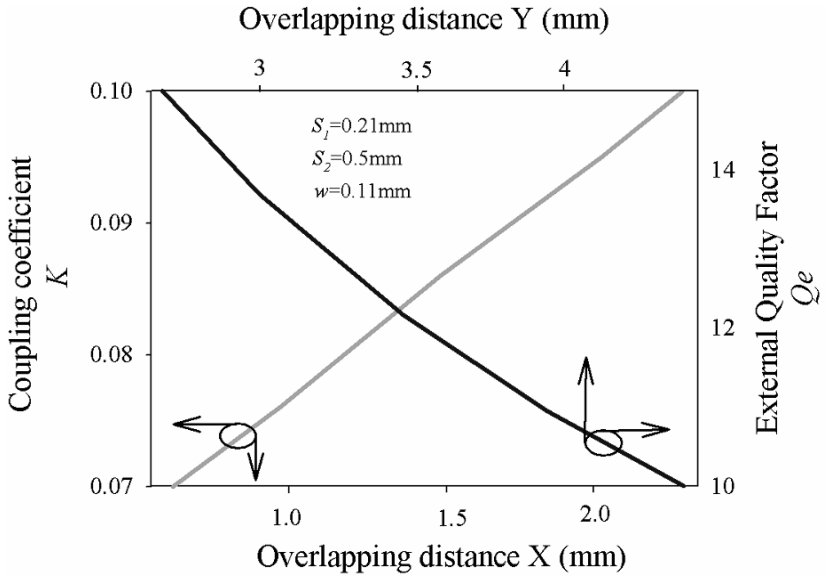

Fig. 2. External quality factor *Qe* for different overlapping distances Y and Coupling coefficient K for different overlapping distances X.

Figure 2 shows also the relationship between the coupling coefficient *K* and the overlapping distance X between resonators (see Fig. 1); the values were simulated considering fixed values for the spacing S_2. The length of the resonator extension A (see Fig. 1) is used to accurately determine the *K* values which define the bandwidth required for each state of the filter.

The filter center frequency is determined by the total length of the resonators; however as the bandwidth must take precise values, each resonator is designed to have two extensions. Extension A set the values of K for each state of the filter (see Fig. 1). Extension B defines the total length of the resonator without increasing the coupling between the resonators, which provides independent control of the bandwidth and center frequency of the filter. When both extensions are enabled the response of the filter is set to the low frequency state, while the high frequency state is obtained when the extensions are disabled.

The input and output couplings of the filter are fixed through the extensions B and C, when both extensions are enabled, the input and output coupling of the filter is the optimal for low frequency state, and when the extensions are disabled, the input and output is the optimal for high frequency state.

To define filter layout, each state of the filter was optimized using ADS/ Momentum to produce the required theoretical design parameters *Qe* and *K* for each filter state.

3. MEMS Technology

The fabrication technology for the MEMS reconfigurable bandpass filter is an integrated eight-mask surface micromachining process from FBK [13]. In Fig. 3, a cross section of the ohmic switches used in the design is shown. In this technology, movable bridges/cantilevers are manufactured using a 2-μm-thick electrodeposited gold layer. Another 3-μm-thick gold film is selectively superimposed to increase the rigidity of the central part of the beam and for the patterning of the microstrip lines. A third 150-nm gold layer is evaporated over the underpass metal line to implement a low-resistance metal-to-metal contact. A high performance ohmic-contact series cantilever MEMS switch, with structure and dimensions similar to the one reported in [14] has been used to realize the integrated filter. The cantilever is suspended above an interrupted microstrip signal line and anchored at one end.

The membrane dimensions are 180 μm (length) and 110 μm (width). In order to generate a good ohmic contact between the cantilever and the line, some dimples have been placed in the contact area of the microstrip line, by using small poly-silicon bumps deposited underneath. The membrane embeds 10 μm × 10 μm holes for the easier removal of the sacrificial layer, increased flexibility and reduced damping. The bias network is made of poly-silicon high resistivity lines to reduce losses.

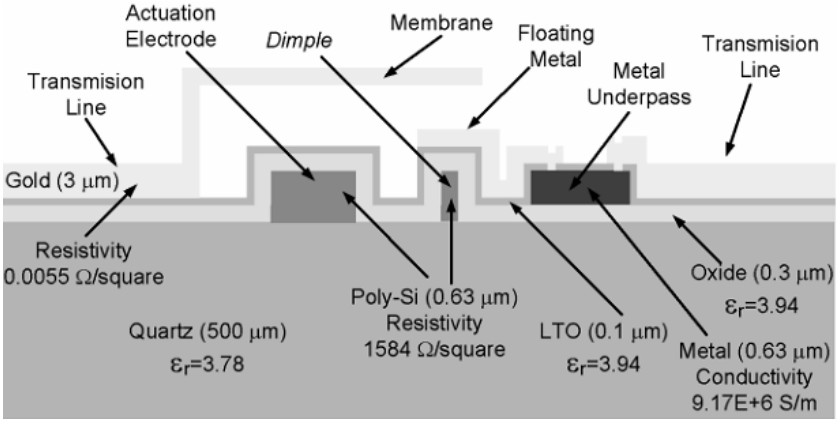

Fig. 3. Diagram of the cantilever MEMS switch on a quartz substrate.

4. Results

The fabricated filter is shown in Fig. 4 and Table 2 contains the filter dimensions. It was realized on a 500 μm thick quartz substrate (ε_r=3.78, tgδ=0.0001). The measurements were taken using a N5242A PNA-X Agilent network analyzer and a probe station.

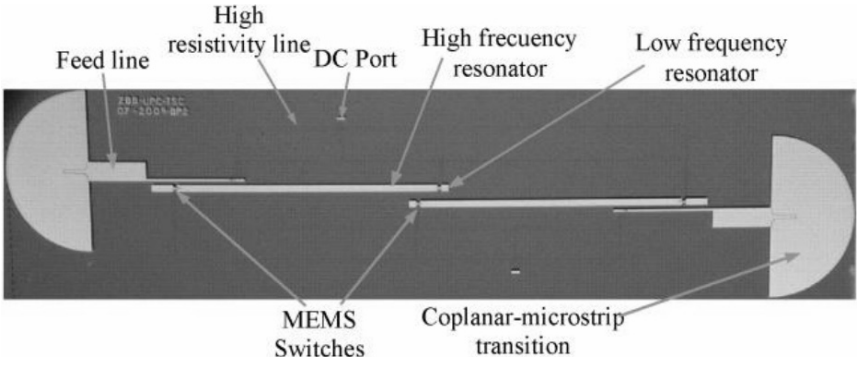

Fig. 4. Photograph of the switchable bandpass filter.

Table 2. Filter dimensions (in mm)

W_1	S_1	S_2	High resistivity lines		Extension A length	Extension B length	Extension C length	Overlapping distance X	Overlapping distance Y	High frequency resonator	
			Mean length	width						length	width
0.11	0.21	0.5	8.5	0.01	0.37	1.1	0.95	2.15	4.94	26.9	0.5

The measured actuation voltage of the MEMS switches is around 50 V. Tables 3 and 4 contain a summary of results. A good agreement in terms of center frequency and bandwidth was obtained for both filter states.

Table 3. Simulated and measured results

	Center Frequency		Fractional Bandwidth	
	Low frequency state	High frequency state	Low frequency state	High frequency state
Simulated	5.5 GHz	6.2 GHz	5 %	3 %
Measured	5.48 GHz	6.13 GHz	7.2 %	3.5 %

Table 4. Insertion loss

	Low Frequency	**High frequency**
Simulated	2.29 dB	1.47 dB
Measured	8.12 dB	4.5 dB

A comparison between simulated and measured responses of the MEMS switchable bandpass filter is shown in Fig. 5. For the low frequency state the center frequency deviation between simulations and measurements is 20 MHz.

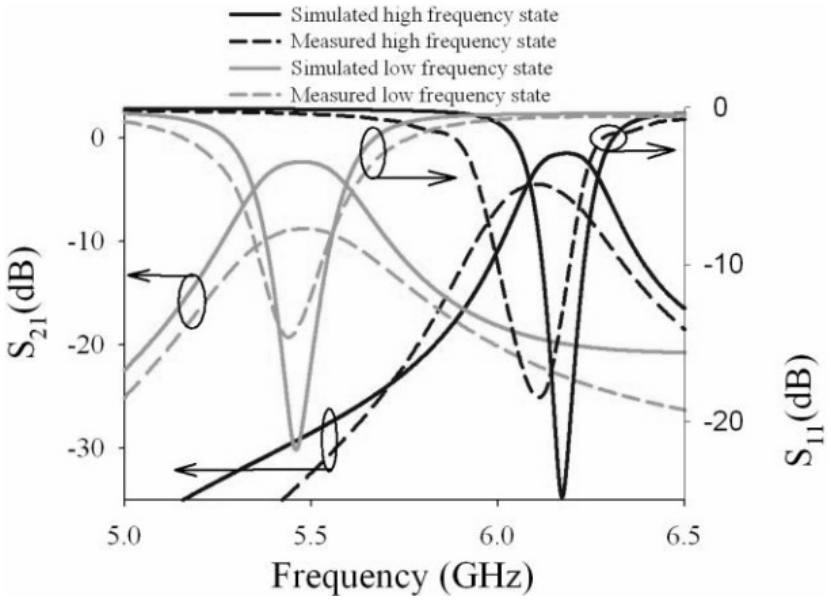

Fig. 5. Simulated and measured results.

The return loss at the passband of the filter is around 21 dB in simulations, and 15 dB in measurements. The difference between the simulated and measured bandwidth is 2.2%. Concerning the high frequency state the center frequency deviation between simulations and measurements is 70 MHz. The difference between the simulated and measured bandwidth is 0.5%. The return loss at the passband of the filter is found to be at around 24 dB in simulations, and 19 dB for the measurements.

The deviations between simulated and measured results are analyzed by simulating the filter with different contact resistances and OFF-state capacitances. Fig. 6 shows the simulated results considering the effect of different MEMS switch contact resistance (r_1=1 Ω, r_2=10 Ω, r_3=20 Ω and r_4=30 Ω) on the filter low frequency response. The simulation includes the high resistivity lines. It is apparent that higher values of contact resistance increase the insertion loss in the ON-state. Simulated contact resistance is *Ron*=32.27Ω.

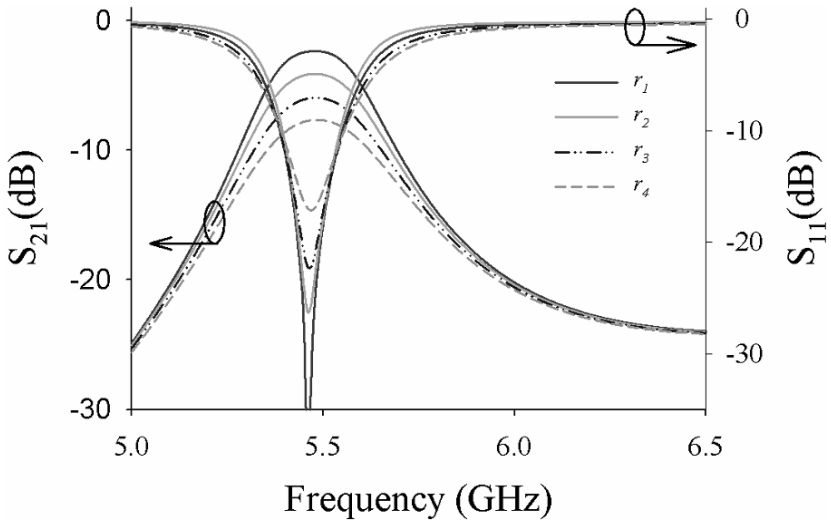

Fig. 6. Simulated results for different series cantilever MEMS switch contact resistance (ON state); r_1 = 1 Ω, r_2 = 10 Ω, r_3 = 20 Ω and r_4 = 30 Ω.

Figure 7 shows the simulated results considering the effect of different MEMS switch OFF-state capacitance on the filter high frequency state. The simulation includes the high resistivity lines. The simulations were done using OFF-state capacitances C_1 = 1fF, C_2 = 10 fF, C_3 = 20 fF and C_4 = 30 fF. It is apparent that the series OFF-state capacitance shifts the center frequency of the filter in the high frequency state. Simulated OFF-state capacitance is C_{off} = 23.46 fF.

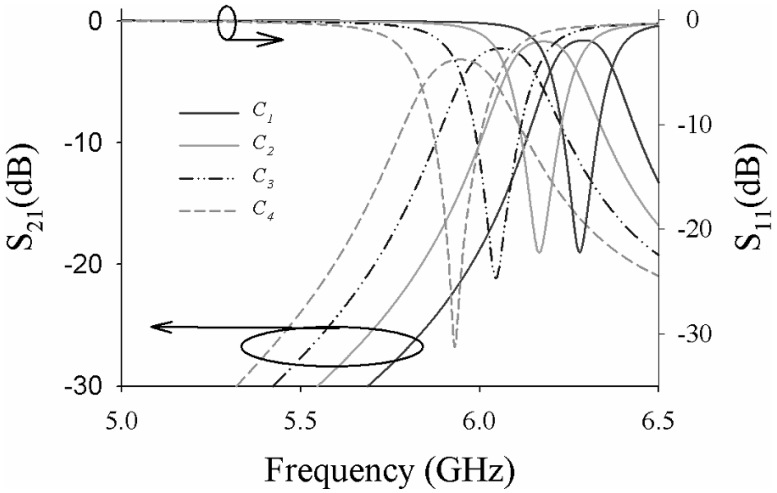

Fig. 7. Simulated results for different series cantilever MEMS switch capacitance (OFF state); C_1=1 fF, C_2=10 fF, C_3=20 fF and C_4=30 fF.

4. Conclusions

A bandpass filter switchable between two discrete frequency bands is demonstrated. The filter is designed using ohmic-contact cantilever MEMS switches to switch between two different states with a center frequency tunable range of 13% in C band. Good agreement between simulations and measurements has been obtained for center frequency and bandwidth. Deviations in the measurements with respect to simulations have been analyzed, and were attributed to an increase of the contact resistance and of the OFF-state capacitance of the switch in the fabricated filter.

Acknowledgements. The authors would like to thank Adrian Contreras at UPC, for assisting the measurements and the staff of FBK MT-Lab for the fabrication of the RF-MEMS device. This work has been financed by research projects TEC2010-20318-C02-01 and PIB2010BZ-00585 from the Spanish Ministry of Education and Culture and research grant Torres Quevedo PTQ-08-01-06434 from the Spanish government. Z. Brito-Brito wishes to thank CONACYT, Mexico for scholarship No. 207926/302540.

References

[1] A.B. YU, A.Q. LIU, Q.X. ZHANG, *Wide tuning range MEMS bandpass filter with inductance change*, International Conference on Solid-State Sensors, Actuators and Microsystems, Transducers **2**, pp. 2061–2064, 5-9 June, 2005.

[2] W.D. Yan, R.R. Mansour, *Tunable Dielectric Resonator Bandpass Filter With Embedded MEMS Tuning Elements*, IEEE Transactions on Microwave Theory and Techniques **55**(1), pp. 154–160, January, 2007.

[3] T. YASUE, T. KOMATSU, N. NAKAMURA, K. HASHIMOTO, H. HIRANO, M. ESASHI, S. TANAKA, *Wideband tunable love wave filter using electrostatically-actuated MEMS variable capacitors integrated on lithium niobate*, International Conference on Solid-State Sensors, Actuators and Microsystems Transducers, pp. 1488–1491, 5-9 June 2011.

[4] A. MILLER, H. JIA-SHENG, Wideband Bandpass Filter With Reconfigurable Bandwidth, IEEE Microwave and Wireless Components Letters **20**(1), pp. 28–30, January 2010.

[5] C. LUGO, G. WANG, J. PAPAPOLYMEROU, Z. ZHAO, X. WANG, A.T. HUNT, *Frequency and Bandwidth Agile Millimeter-Wave Filter Using Ferroelectric Capacitors and MEMS Cantilevers*, IEEE Transactions on Microwave Theory and Techniques **55**(2), Part 2, pp. 376–382, February, 2007.

[6] D. MERCIER, P. BLONDY, D. CROS, P. GUILLON, Distributed MEMS Tunable Filters, European Microwave Conference; pp. 1–4, 24-26 September, 2001.

[7] Z. BRITO-BRITO, I. LLAMAS-GARRO, L. PRADELL, *Selectivity tuned bandpass filter*, Electronics Letters **45**(9), pp. 984–985, 10th September 2009.

[8] C. MUSOLL-ANGUIANO, I. LLAMAS-GARRO, Z. BRITO-BRITO, L. PRADELL-CARA,
A. CORONA-CHAVEZ, *Fully adaptable band-stop filter using varactor diodes*, Microwave and Optical Technology Letters **52**(3), pp. 554–558, March, 2010.

[9] A. OCERA, P. FARINELLI, P. MEZZANOTTE, R. SORRENTINO, B. MARGESIN, F. GIACOMOZZI, *A Novel MEMS-Tunable Hairpin Line Filter on Silicon Substrate*, European Microwave Conference, pp. 803–806, 10-15 September 2006.

[10] S.-J. PARK, K.-Y. LEE, G.M. REBEIZ, *Low-Loss 5.15-5.70-GHz RF MEMS Switchable Filter for Wireless LAN Applications*, IEEE Transactions on Microwave Theory and Techniques **54**(11), pp. 3931–3939, November 2006.

[11] K. ENTESARI, K. OBEIDAT, A.R. BROWN, G.M. REBEIZ, *A 25-75-MHz RF MEMS Tunable Filter*, IEEE Transactions on Microwave Theory and Techniques **55**(11), pp. 2399–2405, November, 2007.

[12] J.-S. HONG and M. J. LANCASTER, *Microstrip Filters for RF/Microwave Applications*, New York, USA, John Wiley & Sons Inc. 2001.

[13] F. GIACOMOZZI, V. MULLONI, S. COLPO, J. IANNACCI, B. MARGESIN, A. FAES, *A flexible technology platform for the fabrication of RF-MEMS devices*, Proceedings of International Semiconductor Conference (CAS), pp. 155–158, Sinaia, Romania, 2011.

[14] A. OCERA, P. FARINELLI, F. CHERUBINI, P. MEZZANOTTE, R. SORRENTINO, B. MARGESIN, F. GIACOMOZZI, *A MEMS-Reconfigurable Power Divider on High Resistivity Silicon Substrate*, IEEE/MTT-S International Microwave Symposium, pp. 501–504, 2007.

High-Frequency Optimization of BiCMOS embedded Through-Silicon Vias for backside-integrated MEMS

M. WIETSTRUCK[1], M. KAYNAK[1], S. MARSCHMEYER[1], A. GÖRITZ[1], S. TOLUNAY[1], S. KURTH[2] and B. TILLACK[1,3]

[1]IHP, Im Technologiepark 25, 15236 Frankfurt (Oder), Germany
[2]Fraunhofer ENAS, Technologie-Campus 3, 09126 Chemnitz, Germany
[3]Technische Universität Berlin, HFT4, Einsteinufer 25, 10587 Berlin, Germany

Abstract. In this work, the high-frequency behavior of BiCMOS embedded *through-silicon vias* (TSV) is analyzed using 3D full-wave EM simulations. Different types of analyzed transmission structures similar to MMIC microstrip and stripline transmission lines are investigated. By optimizing the TSV signal trasmission structure and the dimension of the TSV itself, very low-loss signal transmission with an insertion loss of 0.16 dB up to 100 GHz is feasible. This opens the way to minimize the interconnection losses and provide high-performance BiCMOS circuitry together with backside-integrated components like bulk-micromachining RF-MEMS for heterogeneous 3 D syetem-integration.

1. Introduction

There is a growing interest using through-silicon vias for 3D heterogeneous integration [1]. The integration of TSVs into a high-performance 0.25 µm SiGe:C BiCMOS technology enables the realization of small-size and highly integrated three-dimensional systems [2]-[3]. Apart from a real 3D-integration approach by stacking chips on top of each other, TSVs can be also useful to electrically connect additional components on the wafer backside or inside the silicon substrate to increase the overall system functionality [4]. This gives the possibility to bring together additional components like bulk micromachining RF-MEMS and electronic circuits to improve the system performance and reduce packaging and assembly costs (Fig. 1).

Especially for very high-frequency systems the interconnections between different circuits or system blocks need to be considered and therefore having low-loss electrical connections from wafer front-to-backside is mandatory. The most

promising solution for these type of interconnects are TSVs. In this work, the high-frequency behavior of BiCMOS embedded TSVs is analyzed. By optimizing the TSV signal transmission structure and the dimensions of the TSV itself, very low-loss signal transmission in case of a low or medium-resistive silicon substrate with a substrate resistivity of 50 Ωcm in a wide frequency range up to 100 GHz is feasible. This opens the way to minimize the interconnection losses and provide high-performance BiCMOS circuitry together with backside-integrated RF-MEMS.

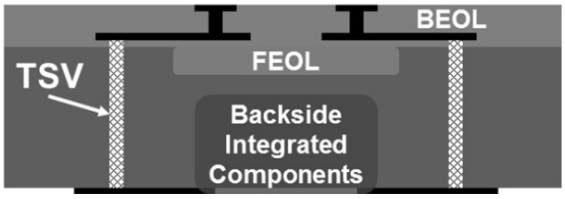

Fig. 1. BiCMOS chip with embedded TSVs for electrical connection from wafer front- to backside.

2. Through-Silicon *Via* Technology

BiCMOS embedded annular-type TSVs are integrated in a 0.25 µm BiCMOS technology using a *via*-middle approach. After fabrication of the Front-End-of-Line (FEOL), deep annular trenches with a depth of ~75 µm and an aspect ratio of 1:25 are etched into the silicon substrate using Bosch process. A SiO_2-liner is deposited on the trench sidewalls to isolate the TSVs from silicon substrate using SACVD process [5]. To achieve a low-ohmic electrical connection from wafer front- to backside, the trenches are filled with CVD-tungsten applying an alternating deposition and etch-back process. Finally, the TSVs are connected to the *Back-End-of-Line* (BEOL) *via* the first metallization layer (Metal1) and the standard BEOL fabrication is finished (Fig. 2).

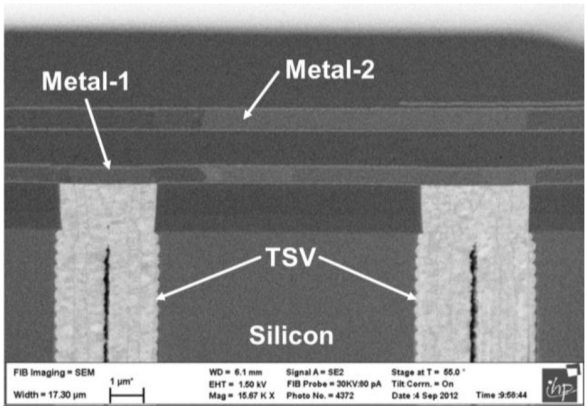

Fig. 2. FIB-image showing BiCMOS embedded tungsten TSVs and part of the BEOL metallization stack.

3. TSV 3D EM-Simulation

The high-frequency S-parameter simulation is realized using 3D full-wave simulation tool HFSS. For high-frequency signal transmission, the signal needs to be transferred using a transmission line structure similar to an embedded ground/ signal microstrip- (GS), ground/ signal/ground stripline- (GSG) or coaxial structure to guide the signal from wafer front- to backside. It provides a well-defined impedance matching to 50 Ω to prevent from significant signal reflection [6]. A GS- and GSG-structure can be realized with a lower complexity fabrication process compared to coaxial TSV because of unavoidable thickness variations of coaxial signal and ground-ring during BOSCH-process and the requirement for at least two metallization layers on wafer backside. Hence, we will focus on GS- and GSG-structures (Fig. 3).

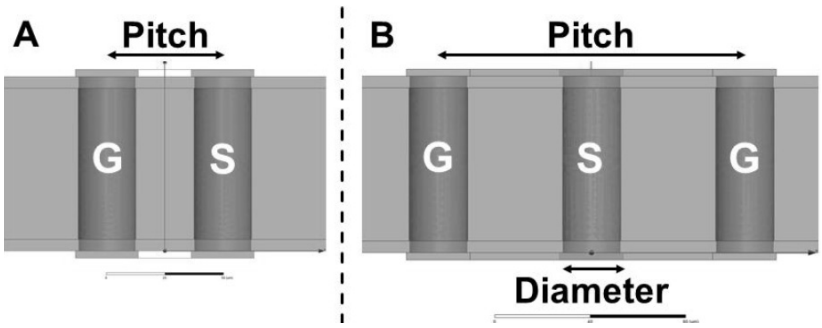

Fig. 3. Cross-section view of TSV simulation models showing the GS- (A) and GSG-structure (B) with signal and return-path.

The most important design parameters for transmission line impedance matching are the metal-line width and the separation. Transferring these transmission line design parameters to a GS- or GSG-TSV structure, the TSV diameter as the line width and the TSV pitch as the separation needs to be optimized. The RF-performance influence of TSV diameter, pitch and the interaction between each other will be investigated by applying a parametric RF-simulation. Both parameters will be swept simultaneously providing all possible design configurations ending in a matrix of n*m parameter sets.

A. GS-TSV Structure

The TSV diameter is varied in the range from 15 to 35 µm with a step-size of 5µm whereas the pitch is varied in the range from 40 to 100 µm with a step-size of 10 µm ending in a matrix of 35 parameter sets. The insertion loss for all different combinations is summarized in Fig. 4 showing a strong sensitivity of the insertion loss with respect to the design parameters.

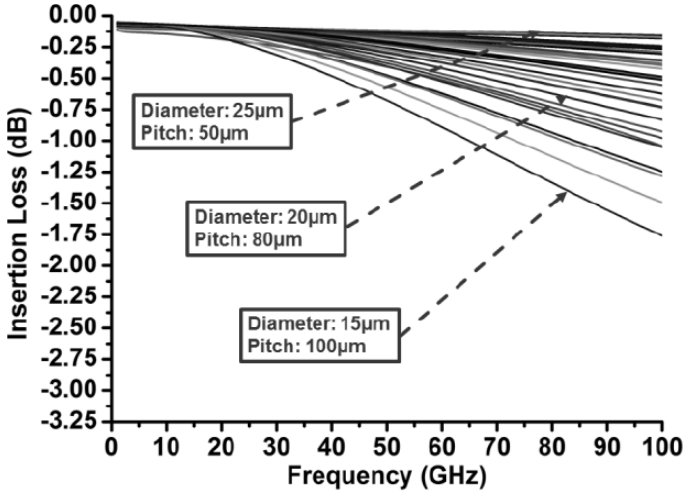

Fig. 4. Insertion loss vs. frequency for TSV diameter from 15 to 35 µm and TSV pitch from 40 to 100 µm. Three different arbitrary parameter sets are highlighted.

It is obvious that the insertion loss shows a continuous behavior over the whole frequency band without any resonance effects. Therefore a comparison of the insertion loss at a specific operating frequency of 100 GHz is reasonable (Fig. 5).

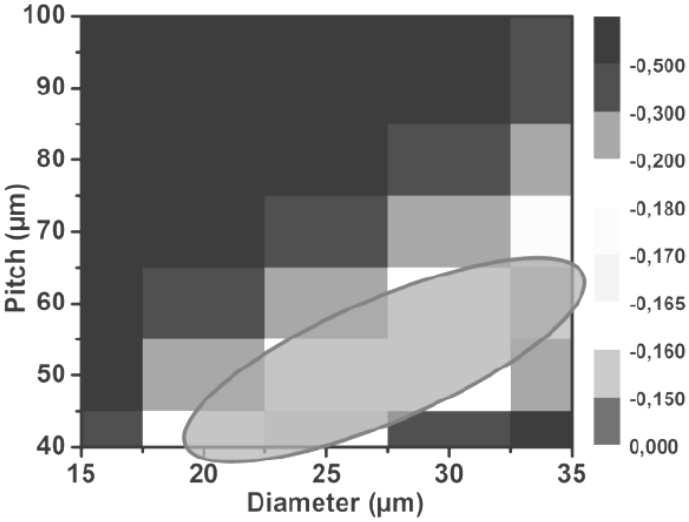

Fig. 5. Insertion loss vs. diameter and pitch at 100 GHz. The area with minimum insertion loss of 0.16-0.17 dB is highlighted.

Besides obtaining a minimum insertion loss, the area consumption of the full transmission structure needs to be also considered. A fixed TSV diameter of 25 µm is chosen for further investigation because it provides a good tradeoff between

insertion loss, manufacturability and area consumption (less than 1% increase in insertion loss compared to the best simulated result). The insertion and return loss with variation of the TSV pitch is shown in Fig. 6.

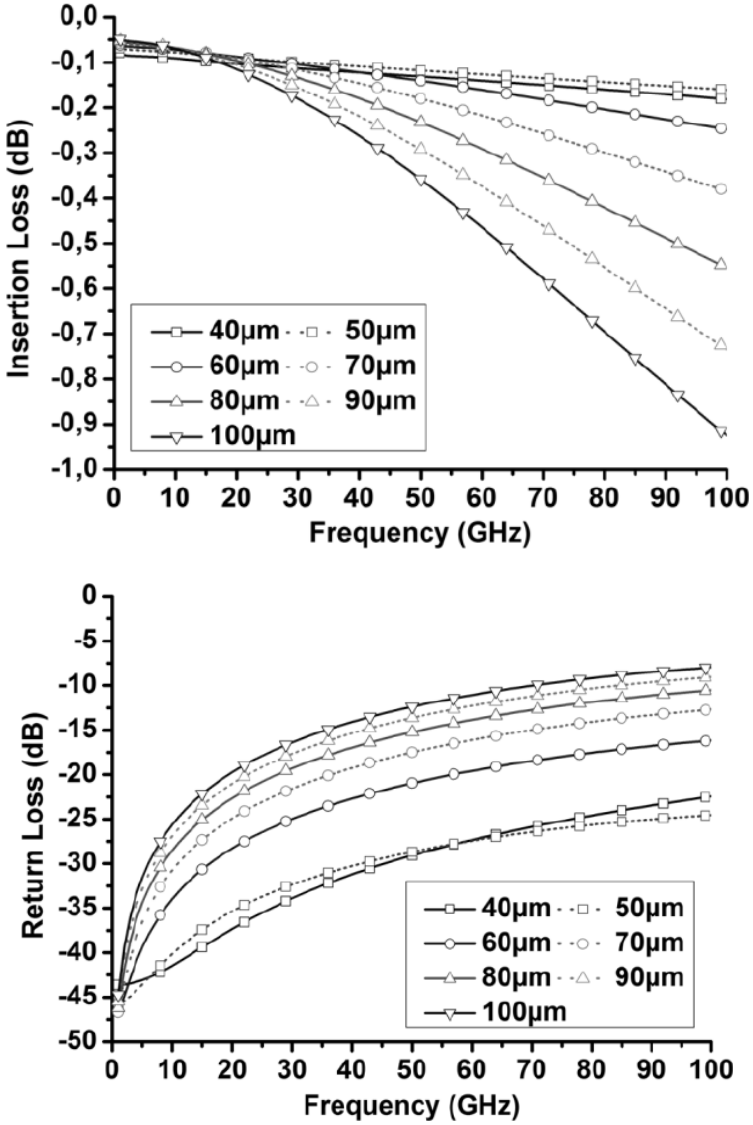

Fig. 6. Insertion and return loss with a fixed diameter of 25 µm and variation of the TSV pitch for a GS-structure.

Obviously, a diameter of 25 µm and a pitch of 50 µm are sufficient to achieve a minimum insertion loss of 0.16 dB up to 100 GHz. In comparison, having a pitch

of 60 µm or 100 µm would result in an increase in insertion loss up to 0.25 dB or 0.92 dB at 100 GHz. The reason for the significant increase in insertion loss with increased TSV pitch is the impedance mismatch which can be obviously seen by the return loss in Fig. 6. For the optimal TSV structure, the return loss is below -25 dB over the whole frequency band providing a very good matching to 50 Ω whereas 60 µm or 100 µm pitch result in a return loss of more than -16 dB or -10 dB, respectively.

B. GSG-TSV Structure

To keep the TSV diameter range similar to the GS-structure the diameter is again varied in the range from 15 to 35 µm with a step-size of 5 µm. The pitch area is increased ranging from 80 to 160 µm with a step-size of 10 µm because of the impedance reduction of the second return-path TSV. The insertion loss for all different combinations is summarized in Fig. 7 showing a similar continuous behavior up to 100 GHz.

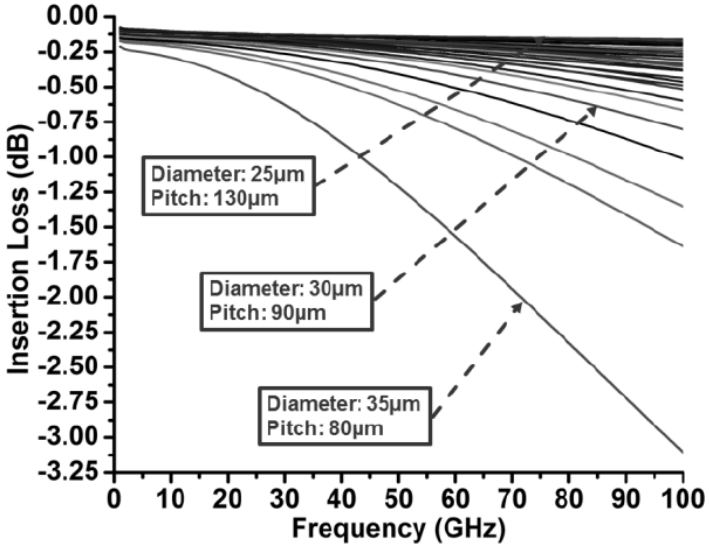

Fig. 7. Insertion loss *vs*. frequency for TSV diameter from 15 to 35 µm and TSV pitch from 80 to 160 µm. Three different arbitrary parameter sets are highlighted.

For comparison, the insertion loss at 100 GHz with respect to the TSV diameter and pitch is shown in Fig. 8.

With a diameter of 20 or 25 µm an insertion loss of ~0.16 dB can be achieved. Because of the afore-mentioned thickness variation of different TSV diameter during Bosch process and to provide direct comparison with the GS-structure, the same diameter of 25 µm is chosen and the insertion and return loss is extracted with variation of the TSV pitch (Fig. 9).

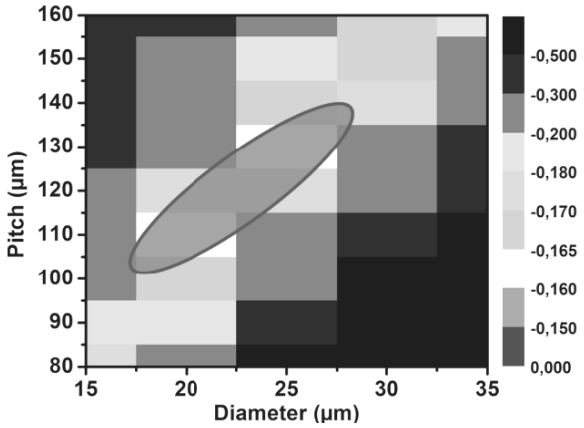

Fig. 8. Insertion loss *vs*. diameter and pitch at 100 GHz. The area with minimum insertion loss of ~0.16 dB is highlighted.

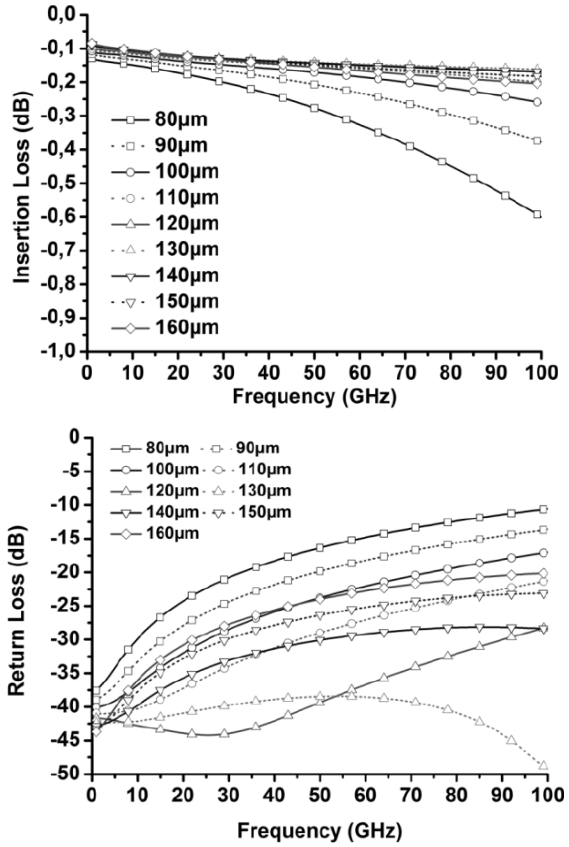

Fig. 9. Insertion and return loss with a fixed diameter of 25 µm and variation of the TSV pitch for a GSG-structure.

With a diameter of 25 µm and a pitch of 130 µm a minimum insertion loss of 0.16 dB and a return loss below -38 dB up to 100 GHz can be achieved providing a very low loss signal transmission and optimal impedance matching.

C. Comparison of GS and GSG-Structure

In principle, both GS and GSG-structures are suitable to provide a low-loss signal transmission from wafer front- to backside. To compare both GS- and GSG-structures using the extracted optimal design parameters of 25 µm diameter and 50 µm pitch (GS) or 25 µm diameter and 130 µm pitch (GSG), the insertion loss, return loss and area consumption for the whole transmission structure should be analyzed. In terms of insertion loss, a minimum insertion loss in the range of 0.16dB can be achieved with both GS- and GSG-structures. In terms of return loss, a GSG-structure gives a better performance of less than -38dB compared to -25 dB for a GS-structure but in principle both versions show a very good matching to a 50 Ω system impedance. The main difference appears in the area consumption of the transmission structures including the TSVs itself, the separation area and the connection pads. The GS-structure occupies an area of ~2100 μm^2. In comparison the GSG-structure occupies an area of ~4250 μm^2 due to the increased separation requirement. Nevertheless comparing to a common SiP-approach using bond wires or flip chip-approach a significant area reduction can be achieved using both GS- or GSG-structures. At least two bond pads would be required to achieve the same functionality with an area of 6400 μm^2/ bond pad which implies an increase of 3-6 times the TSV transmission structures.

4. Conclusion

The high-frequency behavior of BiCMOS embedded TSV has been demonstrated. It has been shown that the design of TSV needs to be strongly taken into account because it is obvious that the high-frequency behavior is very sensitive to the TSV design. With respect to process limitations, the TSV diameter and TSV pitch has been found to be very important parameters to optimize the insertion loss, return loss and impedance matching characteristics.

With the appropriate design parameters TSV transmission structures in a GS- or GSG-configuration showing a minimum insertion loss of 0.16 dB and a return loss of less than -25 dB up to 100 GHz. Using the most-valuable signal transmission design parameters, a high-performance interconnection from wafer front- to backside can be realized. To reduce the area consumption of a TSV transmission structure, GS-structures are advantageous over GSG-structures due to the usage of only two TSVs and the reduced separation in between the TSVs. TSV transmission structures in general and especially GS-structures have an outstanding potential to save highly expensive BiCMOS chip area.

Therefore the integration of BiCMOS embedded TSV gives the opportunity to

make the BiCMOS technology more attractive by including additional components like RF-MEMS into the silicon substrate to increase the system functionality and reduce the overall costs.

Acknowledgements. The authors thank to the team of the IHP pilot line for excellent support. This work was supported by the BMBF (03IS2011-NANETT *Nanosystemintegration*).

References

[1] J. BARON, *et al*, *3DIC & TSV Interconnects–2012 Business Update*, Yole Developpement 2012.

[2] T. KARNIK, *et al*, *Microprocessor system applications and challenges for through-silicon-via-based three-dimensional integration*, IET Comput. Digit. Tech. **5**(3), pp. 205–2012, 2011.

[3] I. NDIP, *et al*, *High-Frequency Modeling of TSVs for 3-D Chip Integration and Silicon Interposer Considering Skin-Effect, Dielectric Quasi-TEM and Slow-Wave Modes*, IEEE Transactions on Components, Packaging and Manufacturing Technology **1**(10), October, 2011.

[4] V. RAJARAMAN, *et al*, *Below-IC post-CMOS integration of thick MEMS on a thin-SOI platform using embedded interconnects*, IEEE 254th International Conference on Micro Electro Mechanical Systems (MEMS), pp. 220–223, Paris, France, 2012.

[5] M. LISKER, *et al*, S*ub-Atmospheric Chemical Vapor Deposition of SiO_2 for Dielectric Layers in High Aspect Ratio TSV*, ECS Transactions **35**(2), pp. 95, 2011.

[6] T.G. LIM, *Through-Silicon Via Interposer for Millimetre Wave Applications*, IEEE 61st Electronic Components and Technology Conference (ECTC), pp. 577–582, 2011.

RF MEMS Modeling with Artificial Neural Networks

L. VIETZORRECK, M. MILIJIĆ, Z. MARINKOVIĆ, T. KIM,
V. MARKOVIĆ and O. PRONIĆ-RANČIĆ

Abstract. In this contribution we will show how artificial neural networks can be efficiently used to build models of RF MEMS components or to optimize them without enhanced numerical efforts. The method is especially interesting for technologists, who want to modify or optimize switch parameters for a fixed technology without using heavy simulation tools. As examples the fast and accurate calculation of scattering parameters for an ohmic switch dependent on 4 different geometrical dimensions over frequency is shown. The second example is the derivation of some lateral dimensions for the resonant frequency of a capacitive switch without using optimization routines.

For the design and development of RF MEMS based circuits it is very helpful to have proper and accurate MEMS models to be used in a circuit simulation. The circuit models are usually derived by physical assumptions, however, the complexity of the model increases by considering more parasitic effects, making the model extraction more complicated. Moreover, it is needed to optimize the MEMS by adjusting the geometrical parameters to achieve a desired performance. Usually the optimization is performed by a series of time-consuming full-wave simulations.

In this paper a new *Artificial Neural Networks* (ANN) based method to be used in the design of RF MEMS devices is proposed. ANNs have excellent learning and generalization abilities, and thus are suitable to be applied as a fitting tool for different RF and microwave devices [1–3]. ANNs are trained by a set of existent input and output relations, obtained by simulations or measurements. The model is then validated by comparing the ANN response with output values obtained for combinations of dimension values, within the parameter range of the test set, not seen by the ANN during the training. In the past, ANNs have been used for modeling a capacitive switch by variation of width and length of the membrane [4]. In this contribution neural models of RF MEMS switches are used for the

determination of the scattering parameters of an ohmic switch (see Fig. 1a), based on the 4 lateral dimensions length and width of the bridge, Ls and Ws, as well as the size of the gaps Lg and Wg to the surrounding CPW, which will strongly affect the matching of the switch (see Fig. 1b).

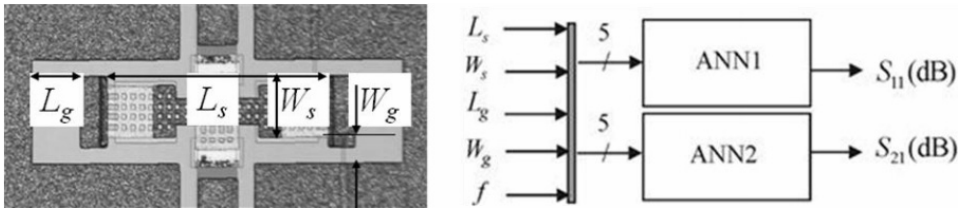

a) b)

Fig. 1. a) Photograph of the Ohmic switch realized by FBK Trento [5] with dimensions b) ANN model utilized.

A comparison of the scattering parameters obtained by the newly derived ANN model with full-wave simulations is shown in Fig. 2. As it can be seen, over the whole frequency range a good coincidence between the two simulation results is obtained. Of course, for producing the required data for training of the ANNs, a certain number of full wave simulations is needed before. The distribution of the parameter combinations is randomly chosen, but spanning the whole possible parameter space. After the model has been successfully installed, results for any combination of parameters within the given input space can be modeled within seconds. Also finding optimal gap values to match the switch in a certain frequency range becomes very easy by plotting a number of curves with varying parameters or using the optimization routine of a circuit simulator instead of the much more time-consuming routines of a full-wave simulation tools. For technologists, having a settled technology, where only the lateral parameters might by varied according to the desired application, this might be an interesting approach, as once the model has been established, they can perform simulations and optimization without using full-wave electromagnetic simulation tools.

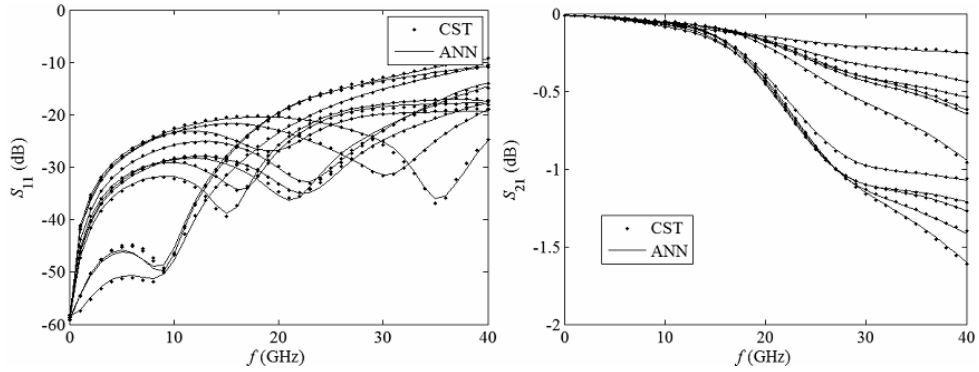

Fig. 2. Comparison of return loss and insertion loss for an ohmic switch in down position.

As another example the inverse model for a capacitive switch [6] is shown. Here the resonance frequency is given as input and some lateral dimensions of a switch, where the membrane consists of a solid part in the middle and a fingered part at the anchoring, are derived (see Fig. 3).

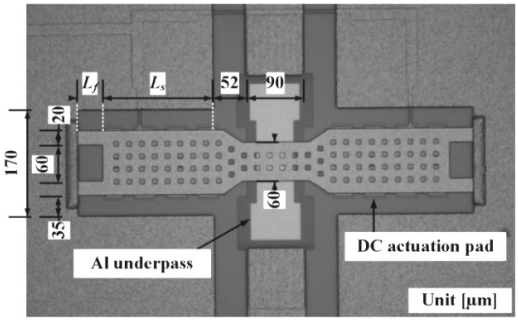

Table 1. Rf mems switch inverse modelling results: *Ls*

L_f (μm)	f_{res} (GHz)	L_S (target) (μm)	L_S (μm)	Relative error (%)
25	22.78	75	74.9	0.1
65	19.17	75	75.5	0.7
85	17.92	75	75.3	0.4
65	10.83	350	348.0	0.6
85	10	400	403.4	0.9

Fig. 3. Photograph of capacitive switch [5] and ANN model with results.

By fixing one of the variable parameters, e.g. the length of the fingers Lf, we can obtain the necessary length of the solid part Ls for the desired resonance frequency without running any optimization procedure.

Acknowledgements. We thank Fondazione Bruno Kessler, Trento, University of Perugia, Thales Alenia, Italy and CNR, Rome, for providing switch parameters and measurement results.

References

[1] Q.J. ZHANG and K.C. GUPTA, *Neural Networks for RF and Microwave Desig*n, Boston, MA: Artech House, 2000.

[2] J.E. Rayas-Sanchez, *EM-based optimization of microwave circuits using artificial neural networks: The state-of-the-art*, IEEE Trans. Microw.Theory Tech. **52**(1), pp. 420–435, January, 2004.

[3] H. KABIR, L. ZHANG, M. YU, P. AAEN, J. WOOD and Q.J. ZHANG, *Smart modelling of microwave devices*, IEEE Microw. Mag. **11**, pp.105–108, May, 2010.

[4] Y. LEE, D.S. FILIPOVIC, *Combined full-wave/ANN based modelling of MEMS switches for RF and microwave applications*, Proc. of IEEE Antennas and Propagation Society International Symposium 1A, pp. 85–88, July, 2005.

[5] S. DiNARDO, P. FARINELLI, F. GIACOMOZZI, G. MANNOCCHI, R. MARCELLI, B. MARGESIN, P. MEZZANOTTE, V. MULLONI, P. RUSSER, R. SORRENTINO, F. VITULLI, L. VIETZORRECK, *Broadband RF-MEMS based SPDT*, Proc. European Microwave Conference, Manchester, Great Britain, September 2006.

[6] T. KIM, Z. MARINKOVIĆ, V. MARKOVIĆ, M. MILIJIĆ, O. PRONIĆ-RANČIĆ, L. VITZORRECK, *Efficient Modelling of an RF MEMS Capacitive Shunt Switch with Artificial Neural Networks*, Proc. of URSI-B 2013 International Symposium on Electromagnetic Theory, Hiroshima, Japan, May, 2013, accepted for presentation.

Membrane Supported D-Band Antenna Processed on Low-Resistivity Silicon

Alina-Cristina BUNEA[1], Andrei AVRAM[1],
Dan NECULOIU[1], Christian RUSCH[2]

[1]National Institute of R&D in Microtechnologies (IMT), Micromachined Microwave and Millimeter Wave Circuits Laboratory, 126 A (32B)
Erou Iancu Nicolae, 077190, Bucharest, Romania
Tel: +40-21-269-0775
[2]Karlsruhe Institute of Technology (KIT), Institut fuer Hochfrequenztechnik und Elektronik, 12 Kaiserstrasse, 76131, Karlsruhe, Germany
Tel: +49-721-608-46253

Abstract. This paper presents the results obtained for a *Double Folded Slot* (DFS) antenna array supported by a thin dielectric membrane (with a total thickness of 2.1 μm), released by the deep *Reactive Ion Etching* (DRIE) of low resistivity silicon (ρ = 10 Ω×cm). The measurement results demonstrated a good matching ($|S11| < -10$ dB) between 136 GHz and 170 GHz, with a measured calibrated gain of 4.2 dBi at 160 GHz and a simulated efficiency of 67%. The 2D radiation characteristics for the E and H planes were also measured and are presented for 155 GHz, 160 GHz and 165 GHz.

1. Introduction

The numerous applications which are starting to take advantage of the D-band (110–170 GHz) include: high resolution active/passive imaging, high-speed wireless communications, guided navigation and military applications [1].

The main issue in obtaining a fully integrated on-chip front end is related to the low performances and large sizes of antennas. This is mainly due to the lossy substrates used in standard silicon technologies. In this paper, we propose an on-chip antenna using low-resistivity silicon micromachining compatible with BiCMOS processes with an additional *Localized Back-side Etch* (LBE) module.

The micromachined *Double Folded Slot* (DFS) antenna has proven suitable for millimeter wave applications [2], being easily scalable, since it operates in a

medium with an equivalent permittivity close to 1. It has shown good matching and radiation behavior at different frequencies when processed on high resistivity silicon. This paper investigates for the first time the behavior of a DFS antenna array operating at 160 GHz processed through low-resistivity silicon micromachining.

2. Electromagnetic Modeling and Design

The antenna was fabricated on a thin dielectric membrane consisting of a 1.5 μm SiO_2 layer grown through thermal oxidation and a 0.6 μm thick Si_3N_4 layer, deposited through LPCVD on a 525 μm thick low resistivity (ρ = 10 Ω×cm) silicon wafer. The membrane was released using the Bosch Deep Reactive Ion Etching (DRIE) process in the ICP-RIE PlasmaLab100 (Oxford Instruments) equipment. The metallization consisted of a thin Cr layer for adherence and a 1 μm thick Au layer.

A 3D electromagnetic model was developed using the CST Microwave Studio software package and took into account the technological process [2]. For example, the bi-layer dielectric membrane was modeled as a single layer with the equivalent permittivity of 4.66. Due to the very thin membrane, the antenna behaves as if it were suspended in air.

The 3D model developed for the membrane supported antenna structure, surrounded by the low resistivity silicon bulk is presented in Fig. 1.

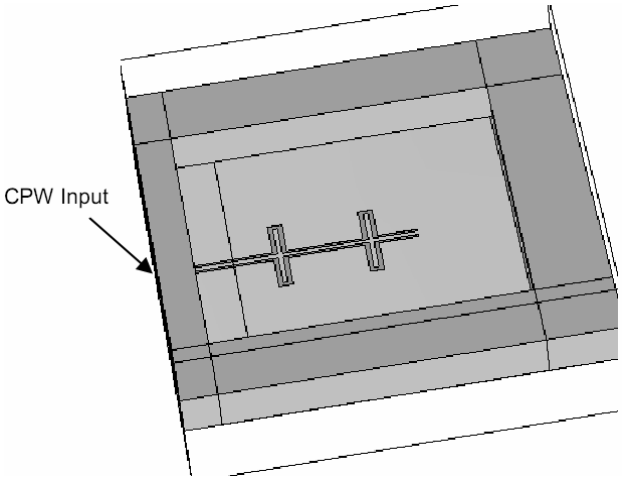

Fig. 1. 3D view of the electromagnetic model.

The antenna consists of two folded slots with a total length of about $1/2 \bullet \lambda_0$ (where λ_0 is the wavelength in free space at 160 GHz). The distance between the folded slots is about $1/2 \bullet \lambda_0$, in order to obtain a high directivity broadside radiation. The shorted stub added in the opposite side of the feed line is used to equilibrate

the radiation pattern and can be used in some applications as a DC return path. Using this information as the initial guess for the design, the antenna structure was optimized.

The structure was simulated using the time domain solver and a multipin rectangular waveguide port to excite the QTEM mode on the CPW feed. The model is fully parametric, allowing for optimization through parametric studies, setting the matching and the directivity as the main goals. Using this approach, the user is the one that takes the decisions during the optimization process, considering the intermediary results, instead of letting the machine-based optimization routine make the choices. In the end, the designer settles for a tradeoff between the main goals.

The EM simulation includes the influence of the EM coupling between the two folded slots as well as the influence of the low-resistivity substrate.

The 2D vector plot of the electric field distribution for a cutting plane aligned with the vertical axis (z axis), placed right beneath the metal layer, is shown in Fig. 2. The orientation of the arrows in the double folded slots indicates that both radiate in-phase, leading to a maximum broadside radiation.

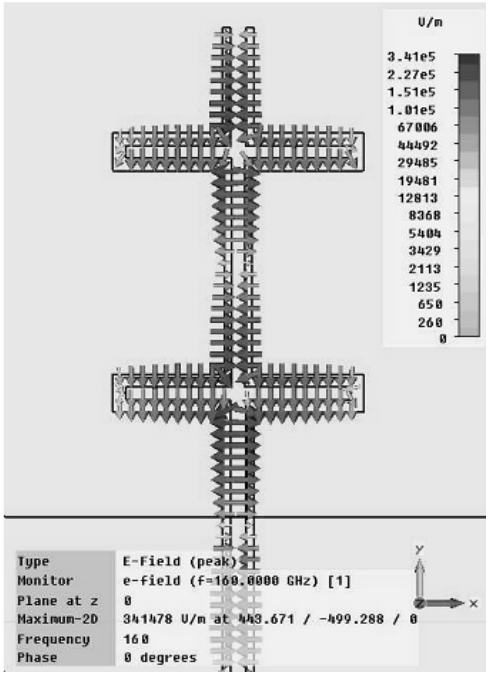

Fig. 2. Electric field distribution at 160 GHz.

The simulated 3D radiation pattern of the DFS antenna at 160 GHz is shown in Fig. 3. Due to the very thin membrane, the antenna behaves as if it were suspended in air and the radiation pattern exhibits two almost symmetrical main lobes.

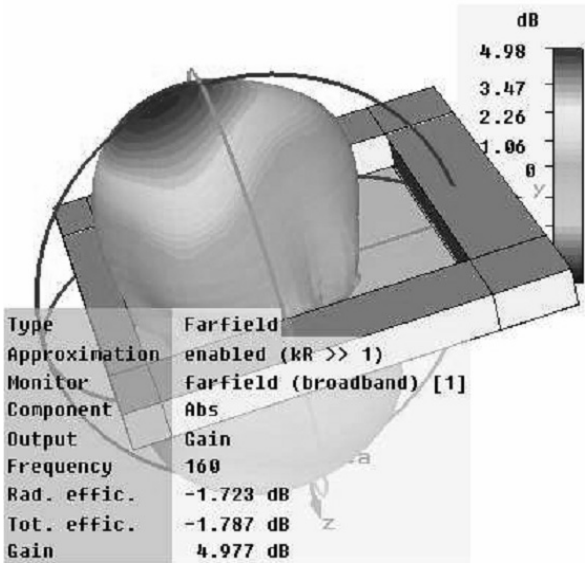

Fig. 3. 3D radiation pattern of the DFS antenna at 160 GHz.

The direction for maximum radiation is almost normal to the antenna plane for both lobes. Simulations show a radiation efficiency higher than 50% for the 140–170 GHz frequency range, with 67% efficiency at 160 GHz.

3. Experimental Results

The structure was characterized with the probe based setup available at the Karlsruhe Institute of Technology [3], with a Millimeter Wave VNA Extender (V06VNA2–T/R–A) 110–170 GHz.

Due to the fact that the membrane supported antenna has a bidirectional, almost symmetrical, radiation pattern (see Fig. 3), the structure must be suspended on a low loss material with the permittivity close to 1, so as not to influence the lower lobe radiation.

First, the reflection losses were measured using the one port, on wafer *Short – Open–Load* (SOL) calibration. A comparison between the measured and simulated reflection losses is shown in Fig. 4. The measured operating bandwidth ($|S11| < -10$ dB) is between 136 GHz and 170 GHz, with a matching better than – 20 dB at 160 GHz.

In order to completely characterize the *Antenna Under Test* (AUT), calibrated radiation measurements were also performed. The transmission characteristic was measured using the AUT as emitter and a D-band horn antenna as a receiver. The signal captured by the horn antenna was processed by a standard sub-harmonic mixer. The whole system was controlled by a computer and the results were processed using a MatLab routine.

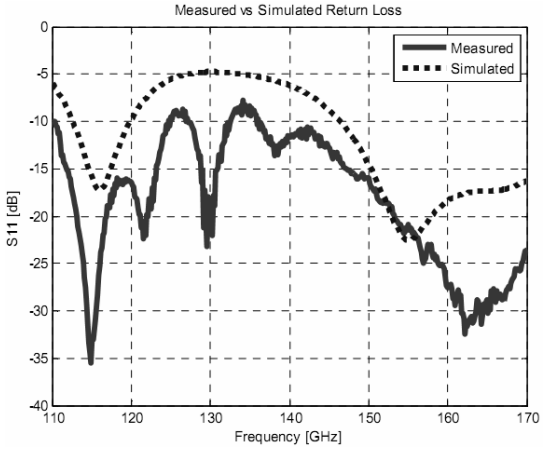

Fig. 4. Measured *vs.* simulated reflection losses of the DFS antenna.

A comparison between the measured and simulated gain for the broadside direction is presented in Fig. 5. There is a very good agreement and the antenna demonstrates a measured gain of about 4.2 dBi at 160 GHz, which can be considered the current State of the Art for low-resistivity silicon on-chip antennas operating at frequencies higher than 110 GHz [4].

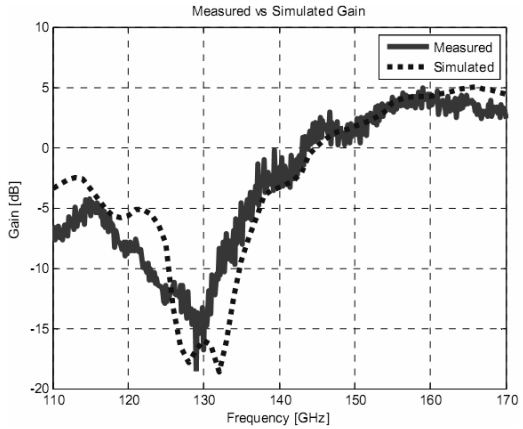

Fig. 5. Measured *vs.* simulated gain as a function of frequency in the D band.

4. Radiation Pattern Measurements

For this antenna structure, the E-plane is defined along the CPW transmission line that feeds the structure (as demonstrated by the electric field distribution presented in Fig. 2), while the H-plane is parallel to the folded slots.

Figure 6. shows the measurement (red solid lines) *vs.* simulation (blue dotted lines) results for the 2D radiation characteristics for the H and E planes at

155 GHz, 160 GHz and 165 GHz. The H plane measurements show a very good symmetry, with very low ripples. In the case of E plane, the measurements are affected by the feeding port.

The results show a very good agreement between simulations and measurements for the H plane, and a fair agreement for the E plane, with some sidelobes appearing due to the experimental setup.

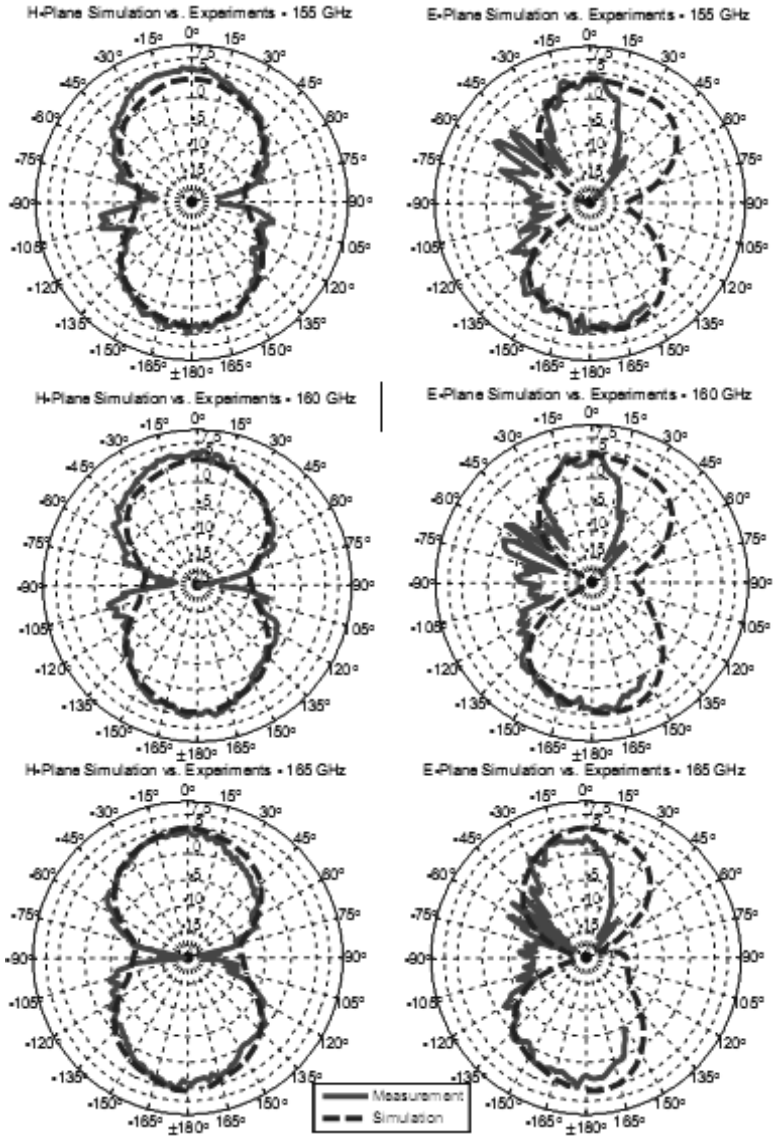

Fig. 6. Measured *vs.* simulated 2D radiation patterns for the E and H planes at 155 GHz, 160 GHz and 165 GHz.

4. Conclusion

The modeling and experimental results obtained for a double folded slot antenna working in the D-band were presented in this paper. The structure is supported by a thin dielectric membrane and was fabricated by DRIE micromachining of low-resistivity silicon. The measurement results show a wide band for the reflection losses with a very good matching around the target frequency of 160 GHz. The antenna exhibits good radiation behavior, with a measured gain of 4.2 dBi at 160 GHz. This research opens up the way of integrating this type of antenna in low resistivity silicon technologies (*e.g.* SiGe BiCMOS technology) with localized back-side etch module.

Acknowledgements. This work was supported by the European Union 7th Framework Program, under the project NANOTEC and the Romanian Ministry of National Education, under the project no. PN-II-ID-PCE-2011-3-0830.

References

[1] *Special Issue on Millimeter-Wave Circuits and Systems*, IEEE Transactions on Microwave Theory and Techniques **60**(3), March, 2012.

[2] A.-C. BUNEA, D. NECULOIU, A. AVRAM, T. KIURU, T. VAHA-HEIKKILA, A. TAKACS, P. CALMON, *160 GHz silicon micromachined folded slot antenna array*, Asia-Pacific Microwave Conference Proceedings (APMC), pp. 896–898, 4-7 December, 2012.

[3] S. BEER, T. ZWICK, *Probe based radiation pattern measurements for highly integrated millimeter-wave antennas*, Proceedings of the Fourth European Conference on Antennas and Propagation (EuCAP), pp. 1–5, 12-16 April 2010.

[4] H.M. CHEEMA, A. SHAMIM, *The Last Barrier: On-Chip Antennas*, IEEE Microwave Magazine **14**(1), pp. 79–91, January-February, 2013.

Analysis of RF MEMS Switches With Metal-Metal Contacts

Steffen KURTH[1], Sven VOIGT[2], Andres BERTZ[2], Sven HAAS[2],
Jörg FRÖMEL[1], Thomas GESSNER[1], Akira AKIBA[3], Koichi IKEDA[3]

[1]Fraunhofer ENAS, Technologie-Campus 3, Chemnitz, D-09126, Germany
[2]Chemnitz Univ. of Tech., Center for Microtechnologies, Reichenhainer Str. 70,
Chemnitz D-09126, Germany
[3]Sony Corporation, Core Device Development Group, 4-14-1, Asahi-cho,
Atsugi-shi Kanagawa, 243-0014 Japan

1. Introduction

MEMS switches are becoming key components in mobile communication for the reconfiguration of filters, of antennas and of front end modules. Low insertion loss (< 0.5 dB), high isolation (> 30 dB), fast response time (< 50 µs), low actuation voltage (< 10 V), low actuation power consumption, and long life time (> 1 Billion switch cycles) need to be achieved. The contact force is playing an important role for low contact resistance and insertion loss as well as for high reliability as to be stated in previous work [1]–[2]. Adhesion forces, van der Waals bonds, metal bonds [3], thin water films, and contact necking [4] have been identified to be the main reasons for reliability issues in case of too low contact force or contact separation force. A strong contact separation force is necessary to prevent contact sticking [5].

This contribution reports on the analysis of metal-metal contacts of MEMS switches. A novel high aspect ratio MEMS fabrication sequence in combination with wafer level packaging is applied for fabrication of an RF MEMS switch with lateral motion. It allows for a relatively large actuation electrode area in a small package, and for high actuation force even with an actuation voltage of 5 V. The focus of this contribution is on the contact behavior. It is shown how operation conditions as like as actuation voltage, RF power, and DC bias influence the contact resistance. The power handling capability and its influence on the contacts, and the intermodulation were investigated also.

2. Design and Fabrication

This paper deals with RF MEMS switch with lateral motion that are fabricated by a novel high aspect ratio MEMS fabrication sequence in combination with wafer level packaging. Deep reactive ion etching and isotropic release etching of the movable parts from the crystalline silicon substrate are applied. Comb drives are used for providing the actuation force. The thickness of the movable part and of the electrode combs are 30 µm.

Fig. 1 shows that the concept of this series switch is based on a double series switch. The contact tips are electrically connected in series. The elasticity of contact beams compensate the differences in the contact gap between both contacts within a chip that may occur by technology tolerances. If one contact is closed earlier than the other, the elasticity of the contact beams allow for further travel of the push rod to close the other contact subsequently. The contact area is coated by the contact metal (barrier/Au layer stack) applying a shadow mask and sputter deposition as the last process step before wafer packaging. It contributes to low contamination of the contact surface and should lead to high reliability and low non-linearity of the contact. A wafer level hermetic sealing process (0-level packaging) is applied for keeping an inner pressure of approximately 20 mbar. More details on the fabrication sequence are given by references [6], [7].

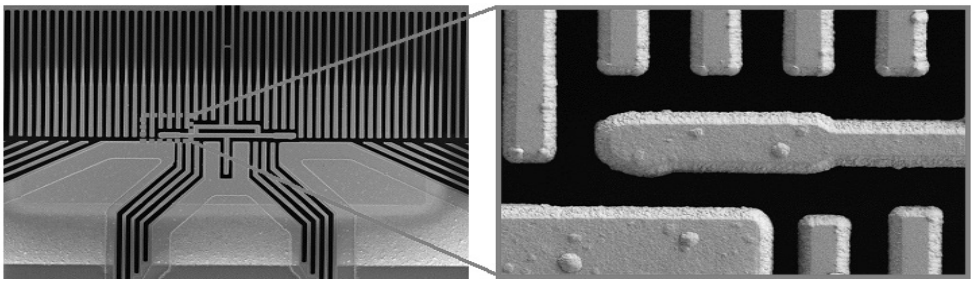

Fig. 1. SEM photograph – contact area of the SPST switch and detailed view of the contact beam.

3. Contact Investigation

The electrically active electrode area is larger than the area that is occupied by the comb drives because of the 30 µm deep electrodes. It leads to a large actuation force (< 200 µN) at low actuation voltage (5 V) and allows for strong restoring springs (500 N/m) and high contact separation force.

In case of MEMS switches, it appears that the contacts have dimensions in the single µm range, *e.g.* 2 µm × 0.5 µm. However, because of the roughness of the contact metal, the contact area that really leads the current is much smaller (Fig. 2).

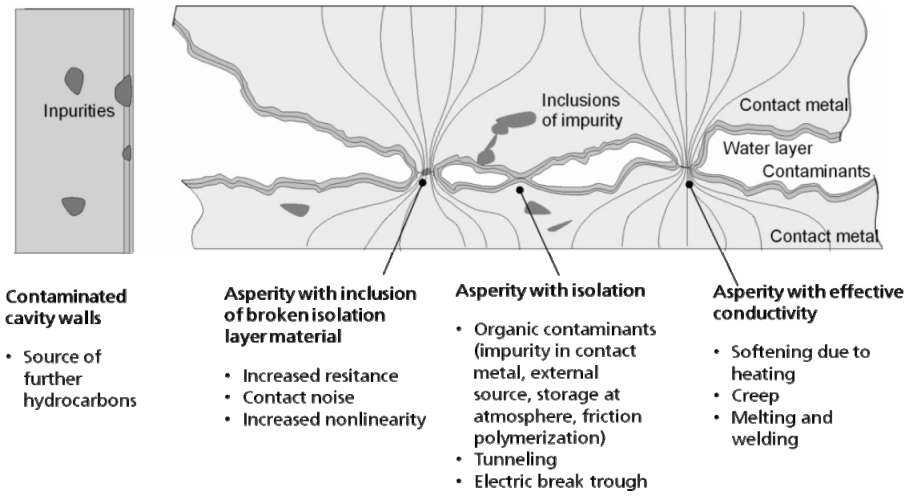

Fig. 2. Schematic view of the contacts and detrimental effects.

Only the outmost asperities of the both contacts come into touch to the counterpart and contribute to the current path. The current spreads on both sides of the asperities in the contact material. Hence, the specific resistivity, the area of the asperities, and the number of asperities influence the resistance between the contacts. It is experimentally shown by a measurement. The results are depicted by Fig. 3. From the stepwise decreasing of the contact resistance or contact voltage at a given contact current during the contact closing, one can derive that very view or even a single asperity contributes to the current path in case of the investigated contacts.

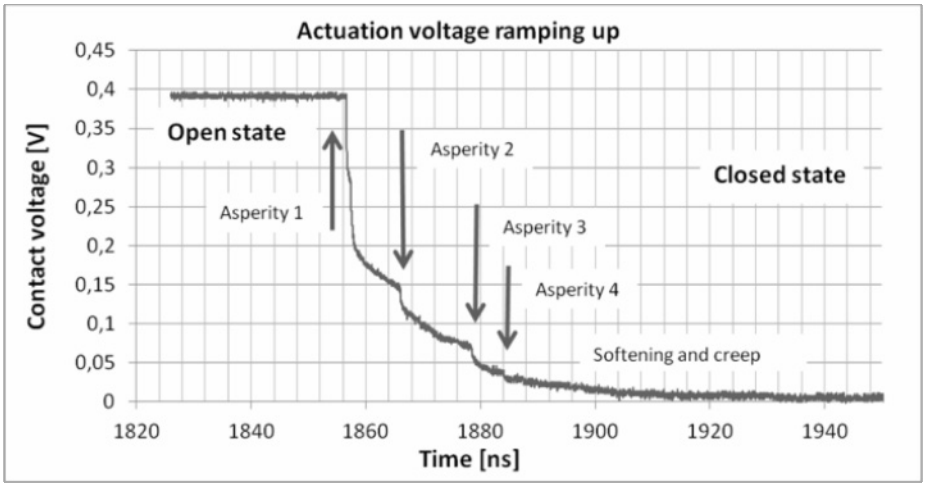

Fig. 3. Contact voltage in the closing process.

Moreover, a dependency of the contact resistance on the actuation voltage is expected because the actuation voltage determines the contact force and the area of the asperities increase with increased contact force and the contact resistance decreases. In addition, it may contribute to mechanical breaking of contamination layers at the contact metal surface. The number of zones that lead the electric current and the conducting area of each single asperity may be increased as a result. Fig. 4 shows a typical contact behavior when the contact is closed for a first time and the actuation voltage is increased in a first part of the experiment and decreased in a second part. The contact starts the forming process with the weak contact force and shows a larger contact resistance. With increased actuation voltage, the contact force becomes higher and a higher number of asperities and a larger area contribute to the current path. This situation holds even when the actuation voltage is reduced in the second part of the experiment.

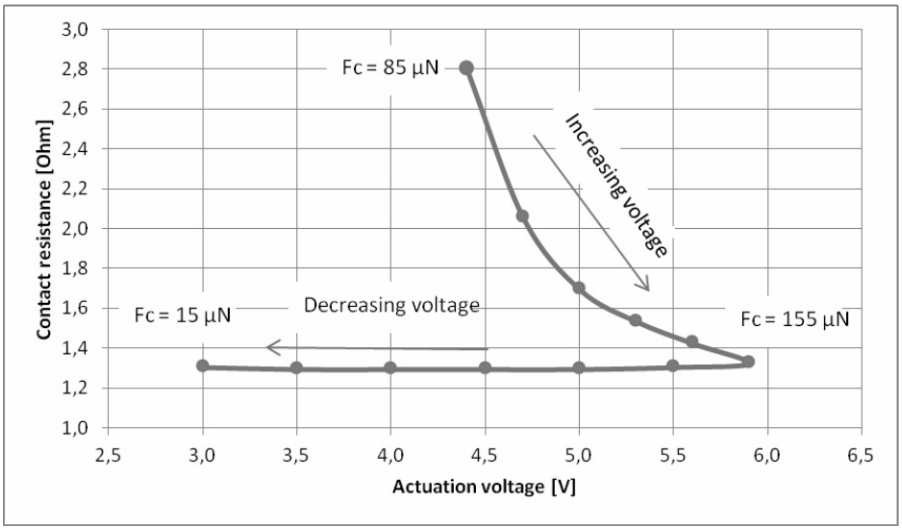

Fig. 4. Typical contact resistance when varying the actuation voltage from the pull in voltage to higher values and subsequently to lower voltage down to r elease voltage (typical behavior).

Non-linearity is tested by intermodulation product measurement. We used a set up containing a vector network analyzer with two independent signal sources and high quality internal directional couplers. In the current case, the first fundamental frequency was chosen to be 1200 MHz and the second fundamental frequency to be 800 MHz. The power at fundamental frequencies and the power at the intermodulation frequency as well as the slope equation of this graph give a third order intercept point of 90 dBm which represents the vertical coordinate of the cross section of both lines (Fig. 5).

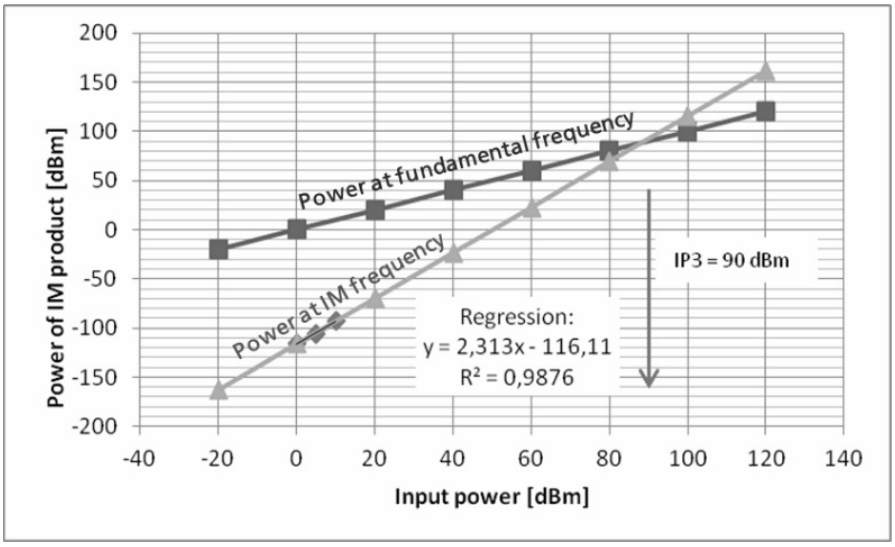

Fig. 5. Results from measurement of intermodulation product intercept point IP3. Diamonds: measurement data of intermodulation product. Triangels: regression of measurement data. Squares: output power at fundamental frequencies.

4. Conclusions

In case of noble metal contacts made of soft material that are working in dry vacuum atmosphere absorbed film layers and metal softening by Joules heating does not play the dominant role in contact formation. Only a few asperities contribute to the current path and the mechanical flattening of the asperities by the contact force are most important. The excellent intermodulation product of approximately 90 dBm indicates that there are no insulating layers or semiconducting material residuals at the contact surface after.

References

[1] Q. MA, T. TRAN, J. CHOU, H. HECK, R. BAR, R. KANT, V. RAO, *Metal contact reliability of RF MEMS switches*, Proc. SPIE **6463**, pp. 646305-1–646305-13, 2007.

[2] C.D. PATEL, G.M. REBEIZ, *An RF-MEMS Switch with mN contact forces*, Microwave Symposium Digest MTT-S, pp. 1242–1245, 2010.

[3] B.D. JENSEN, K. HUANG, L.W. CHOW, K. KURABAYASHI, *Adhesion effects on contact opening dynamics in micromachined switches*, Journal of Applied Physics **97**, pp. 103535 1–9, 2005.

[4] S.T. PATTON, J.S. ZABINSKI, *Fundamental studies of Au contacts in MEMS RF switches*, Tribology Letters **18**(2), pp. 215–229, 2005.

[5] J. TRINGE, W. WILSON, J. HOUSTON, *Conduction properties of microscopic gold contact surfaces*, Proc. SPIE **4558**, pp. 151–158, 2001.

[6] A. AKIBA, S. MITARAI, S. MORITA, I. IKEDA, S. KURTH, S. LEIDICH, A. BERTZ, M. NOWACK, J. FROEMEL, T. GESSNER, *A fast and low actuation voltage MEMS switch for mm-wave and its integration*, IEEE International Electron Devices Meeting, pp. 828–831, 2010.
[7] S. KURTH, S. LEIDICH, A. BERTZ, M. NOWACK, J. FRÖMEL, C. KAUFMANN, W. FAUST, T. GESSNER, A. AKIBA, K. IKEDA, *Reliability enhancement of Ohmic RF MEMS switches*, Proc. SPIE **7928**, pp. 79280C, 2011.

Long-Term Reliability of RF-MEMS Dielectric-Less Capacitive Switches

Viviana MULLONI, Flavio GIACOMOZZI,
Giuseppe RESTA, Benno MARGESIN

Fondazione B. Kessler (FBK-CMM) Via Sommarive 18,
I-38123 Trento Italy
Tel: +39 0461 314432
E-mail: giaco@fbk.eu, mulloni@fbk.eu

Abstract. Long-term switch reliability is one of the issues that so far prevented the widespread use of RF-MEMS switches. In this paper a detailed analysis of long-term actuation properties of a MEMS capacitive switch is presented, together with a framework for the data interpretation and for failure time prediction. Due to the lack of a solid theoretical background, the modeling function is however not univocal, and this leads to a wide interval of possible lifetimes. However, also in the worst case examined, the predicted device lifetime is at least of the order of several years.

1. Introduction

In the last few years RF-MEMS switches have demonstrated outstanding performances in terms of RF characteristics, but switch reliability is still an issue which so far prevented a very broad use of these devices. In particular, in satellite redundancy networks [1], the challenging performance of keeping the switch in on (or off) state without performance degradation for very long time, typically of the order of several years, still has to be demonstrated. These characteristics are challenging for RF-MEMS switches because dielectric charging and micro-welding, the most common switch failure modes, cause stiction of the membrane in down-state, compromising the switch functionality.

Dielectric charging has been recently extensively studied [2] and the effect of charge injection was modeled as a superimposition of exponential charging mechanisms [3], or by means of a stretched exponential law [4], mostly in the case of short stress times, in analogy with charging in dielectrics. In other literature sources, dielectric charging under long-time continuous bias was addressed

adopting a power law of time [5, 6], basing this choice mainly on phenomenological evidence. In spite of this effort, a comprehensive theoretical understanding of the physical mechanisms governing the long-term charging behavior in MEMS switches is still missing, as well as a reliable charging acceleration method, probably because of the complex interplay of electrical and mechanical factors.

In this work, charging in RF-MEMS capacitive dielectric-less switches is investigated, addressing in particular the problem of the failure time prediction of these devices under continuous actuation conditions. Different physical models are compared and discussed, showing that the choice of the fitting law is of paramount importance in the determination of the device lifetime, which is a fundamental parameter for the assessment of switch reliability.

2. Switch Design and Fabrication

The switch investigated is a shunt capacitive switch with enhanced Con/Coff ratio [7, 8]. A picture of the device is reported in Fig. 1.

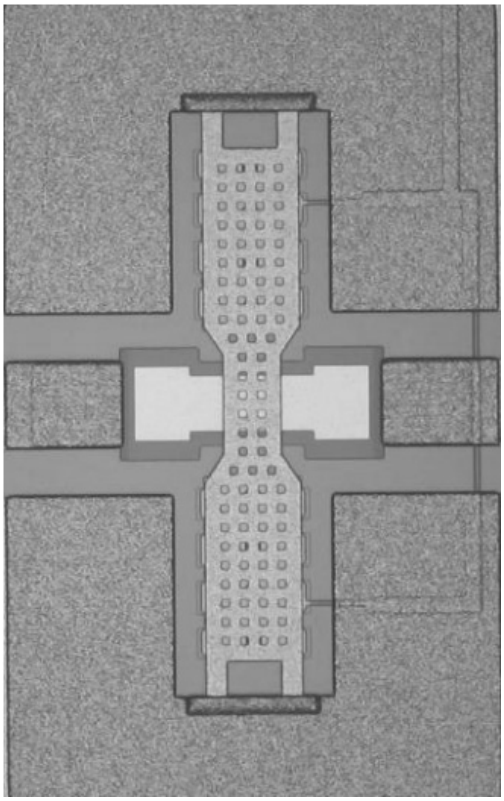

Fig. 1. Micrograph of the investigated capacitive switch.

The switches were manufactured on high resistivity 525-μm thick and 4-inch wide silicon wafers. Actuation electrodes are made in lightly-doped polysilicon, while the underpass line is realized in a sputtered multilayer metal composed by a 500 nm-thick aluminum layer sandwiched between two thin (about 80 nm) bi-layers of titanium and titanium nitride. Polysilicon dimples are included in the switching region to improve the electrical contact. The clamped-clamped membrane is realized by using a 2-μm thick gold layer and is 620 μm long and 100 μm and 60 μm wide above the electrodes and the contact area respectively (see Fig. 1). The switch is dielectric-less, with stopping pillars which prevent the contact between actuation electrodes and mobile membrane. The detailed fabrication scheme and process are reported in ref. [9].

The actuation electrodes without dielectric combined with stopping pillars have proven to be the best solutions in order to minimize charging, while the flatness of the mobile membrane should reduce the non-uniformity of charge injection.
The electromechanical properties of such a device have been deeply analyzed by using ANSYS™ Multiphysics software and then experimentally validated. The membrane resulted quite planar in the off (unbiased) state, both from simulation and from experimental measurements made with an optical profiler. The actuation voltage of a relevant number of switches was measured to verify their correct functioning. The experimental values were found to be in the range 43 ± 2 V, in fairly good agreement with the simulation data, which gave a value of 44 V.

3. Long-Term Actuation

Long-term stress measurements have been performed measuring the actuation and de-actuation voltages of the switch after long actuation times. Fig. 2 reports an example of the capacitance-voltage characteristics at t = 0 and t = 12 hours for the investigated switch, where t is the continuous stress time. It is clearly noticeable that, although the dielectric has been removed from the top of the actuation electrodes, some change in the CV curve due to charging still occurs, involving probably the dielectric around or underneath the electrodes. Two different phenomena can be identified [10, 11] from the CV variations: a shift of the central value of the CV curve and the narrowing of the CV window. The shift is normally considered a direct effect of charge injection, while the narrowing can be caused by a non-uniform charge distribution [10], though other effects can contribute [12]. The most likely candidates for additional contributions are inelastic mechanical deformations and creep. This effects are unfortunately non easily distinguishable from true charging effects in this type of measurement.

In order to better characterize the results a modeling frame has been employed where the two phenomena reported above can be separated taking into account the time evolution of both positive and negative pull-in (V^{+}_{PI} and V^{-}_{PI}) and pull-out (V^{+}_{PO} and V^{-}_{PO}) voltages.

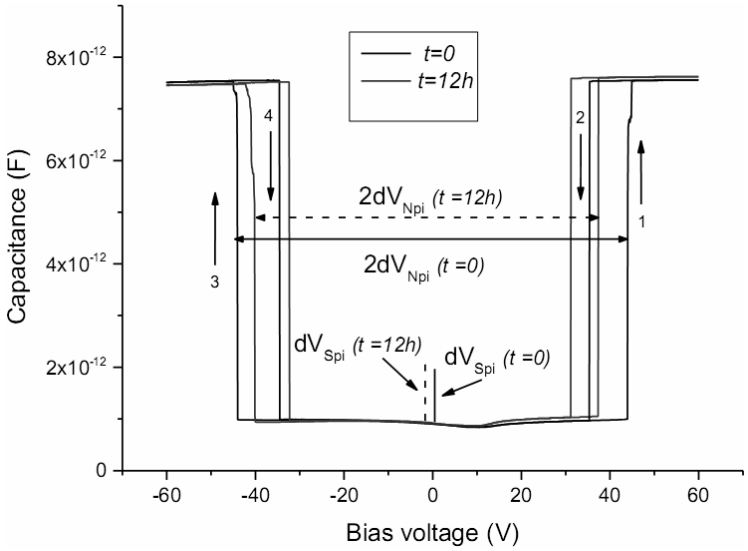

Fig. 2. Capacitance-voltage characteristics of the investigated switch, shown at t = 0 and after 12 hours of continuous actuation. The relation between pull-in (V_{PI}), dV_{NPI} and dV_{SPI} is shown graphically. The same relation holds for pull-out (V_{PO}), d_{VNPO} and dV_{SPO}.

The following parameters have been defined:

$$\mathrm{d}V_{Sx}(t) = \frac{V_x^+(t) + V_x^-(t)}{2} \tag{1}$$

$$\mathrm{d}V_{Nx}(t) = \frac{V_x^+(t) + V_x^-(t)}{2} \tag{2}$$

where the subscript x stands for PI or PO. dV_{Sx} quantifies the asymmetry of the CV curve, whereas dV_{Nx} determines the width of the CV window. After a time t the variations with respect to t = 0 are:

$$\Delta V_{Sx}(t) = \mathrm{d}V_{Sx}(0) - \mathrm{d}V_{Sx}(t) \tag{3}$$

$$\Delta V_{Nx}(t) = \mathrm{d}V_{Nx}(0) - \mathrm{d}V_{Nx}(t) \tag{4}$$

ΔV_{Sx} express the curve translation due to increasing injected charge, while ΔV_{Nx} measures the CV window narrowing, related to other effects. The narrowing value has been found to be always positive [6], that is the CV windows always shrinks with increasing time, whereas the shift can be either positive or negative,

depending on the sign of the total injected charge. This approach to data analysis is a generalization of other analysis techniques employing only positive or negative sweeps.

4. Experimental Results and Discussion

In order to quantify ΔV_{Sx} and ΔV_{Nx} as a function of actuation time, a constant bias, higher than the actuation voltage, has been continuously applied to the device under test for increasing time intervals, starting from a minimum of 5 minutes up to a maximum of several hours. Between two actuation intervals the instrument provided a positive and negative voltage sweep and the capacitance was measured to detect $V_{\pm PI}$ and $V_{\pm PO}$. The total time of the sweep was about one minute, and it has been verified that this interruption does not affect the results for stress times longer than $\sim 10^3$ s. The time intervals were chosen in order to have a constant number of points per decade in a logarithmic plot. The overall actuation time varied from 12 hours to six days, on different samples tested.

While shift due to carrier injection is the dominant effect in switches with dielectric, narrowing is expected to give the major contribution to V_{PI} and V_{PO} changes in this case, being the switch dielectric-less. This was experimentally verified, as shown in Fig. 3. The shift is not negligible, but normally it settles around a stable value after a relatively short time, while ΔV_{NPI} and ΔV_{NPO} increase markedly with time, and this can lead to switch failure if the stress time is long enough.

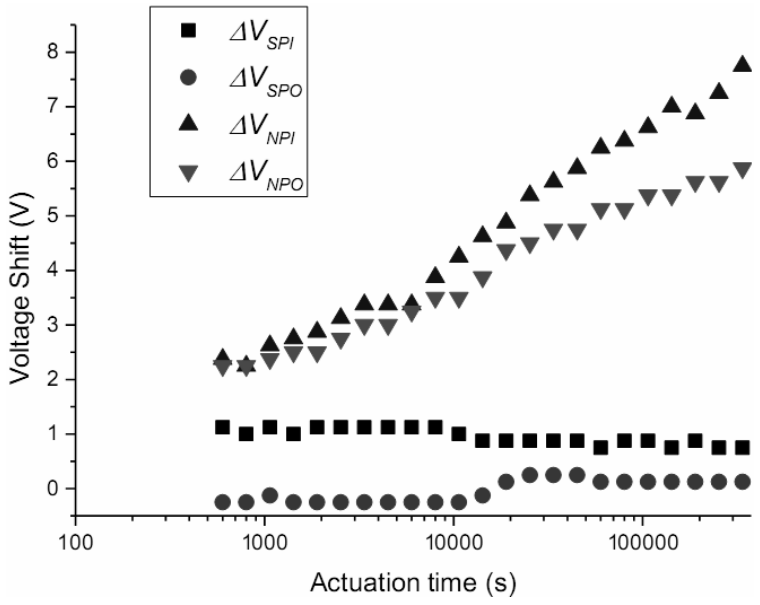

Fig. 3. Example of measured evolution of voltage shift parameters for the investigated switch. The bias voltage is 60 V.

Among the different failure conditions [13], the most important in our case is reached when the V_{PO} value (either positive or negative) crosses zero voltage and the switch can no longer de-actuate, that is when

$$V^{\pm}_{PO}(t_{fail}) = \pm \Delta V_{NPO}(t_{fail}) - \Delta V_{SPO}(t_{fail}) + V^{\pm}_{PO}(0) = 0 \quad (5)$$

where t_{fail} is the time of failure and $V^{\pm}_{PO}(0)$ is the $V^{\pm}_{PO}$ value at $t = 0$. If we assume that t_{fail} is long enough for ΔV_{SPO} to reach a constant value, it can be calculated making a reasonable hypothesis on the physical law governing the ΔV_{NPO} voltage shift. Unfortunately, the choice of the fitting law is not irrelevant for the determination of t_{fail}. In the literature [4, 5], both a power law and a stretched exponential law have been proposed. We have included among the possible fitting functions also a logarithmic law, because this is apparently suggested by the experimental trend of the data. The fitting equations considered are reported in Table 1, while an example of this fit is reported in Fig. 4.

Table 1. Equations of the three fitting law considered

Fitting curve	Equation
Power Law	$\Delta V_{NPO} = a \cdot t^{b}$
Stretched exponential	$\Delta V_{NPO} = \Delta V_{PO}(0) \cdot [1-\exp(-k \cdot t)^{d}]$
Logarithmic	$\Delta V_{NPO} = a - b \cdot \ln(t)$

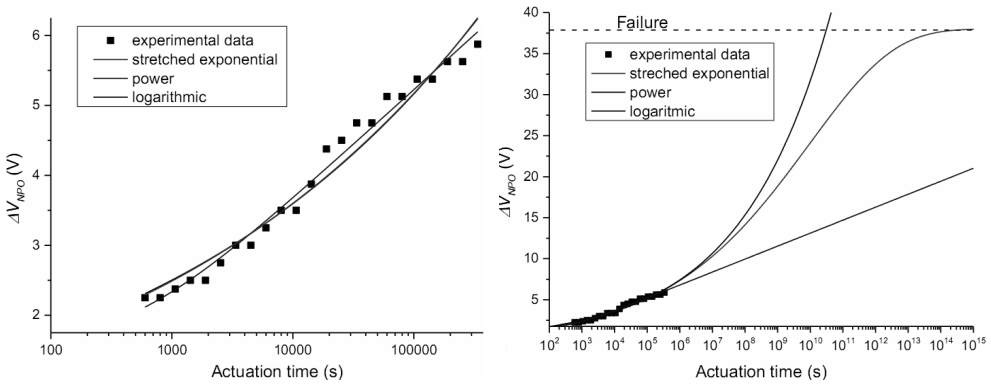

a) b)

Fig. 5. Fitting of ΔV_{NPO} parameter with a power, a stretched exponential and a logarithmic law: a) Fit of experimental data b) Extrapolated long-term forecast.

As can be seen, the best fitting power and stretched exponential laws are perfectly overlapping in Fig. 4 a). This phenomenon can be easily understood considering that in the limit of low values of t, the first order approximation $1-\exp(-k \cdot t)^{d} \approx (k \cdot t)^{d}$ can be used, giving b = d and $a = \Delta V_{PO}(0) \cdot k$. The two equations

are therefore equivalent in the time range explored experimentally. This approximation is however no longer valid when a long-term forecast is made from the short-term data, as shown in Fig. 4 b), where the two curves differ markedly for long stress times. Needless to see, a much longer actuation time (~10^8 s) is needed to discriminate among them, and it is unlikely this time can be reached in a testing laboratory.

Table 2 reports values of t_{fail} calculated for three samples stressed with different total actuation times, where the points at $t < 10^3$ s are excluded from the fit to avoid measurements artifacts. For all samples, t_{fai} increases going from power to stretched exponential and from stretched exponential to logarithmic fitting. In all cases the logarithmic law gives the best fit (higher R^2 value), even though the difference is not big enough to ensure that this function is the most appropriate. Another noteworthy results is that the calculated failure times increase with increasing the experimental stress time, whatever is the fitting law employed. This last observation is somehow positive, because, as far as we can see, it seems that we are not overestimating t_{fai} because of the short experimental stress time. Even in the worst case, the lifetime of the investigated switch typology is at least of the order of several years, and possibly, much longer.

Table 2. Estimated failure times for identical devices but for different total experimental stress time

Dev. n.	Stress Time	ΔV_{SPO} (V)	t_{fail} (y) power	t_{fail} (y) s. exp.	t_{fail} (y) log.	V_{bias}
#1	12h	0.25	6.4	$2 \cdot 10^6$	$2 \cdot 10^{13}$	60 V
#2	94h	0.125	388	$1 \cdot 10^7$	$2 \cdot 10^{18}$	60 V
#3	132h	0.40	926	$2 \cdot 10^7$	$6 \cdot 10^{21}$	60 V

5. Conclusion

Charging in dielectric less switches is a complex phenomenon, which still needs to be better understood especially in relation with long-term reliability tests. In this paper some long-term experimental data and a methodology for their interpretation has been presented for what concern a defined typology of MEMS capacitive switch. The study evidenced some critical aspects due to the lack of a clear theoretical knowledge of the physical mechanism governing charging effects, and a consequen uncertainty in the choice of the best fitting law, which reflects in a large variation of the expected switch failure times. Nonetheless, even in the worst case scenario, the switches investigated can survive for at least several years, and it is likely that their real lifetime is in facts much longer. However, it should be noted that the encouraging result obtained does not in principle exclude the occurrence of other unpredicted failure conditions or mechanisms, that can turn out given the large forecasted lifetime.

Acknowledgements. This work has been partially supported by ESA/ESTEC within the contract ESA ITT AO/1-5288/06/NL/GLC *High Reliability MEMS Redundancy Switch*. The authors are also grateful to the MTLab-FBK personnel for technical help and to Dr. Francesco Solazzi and Dr. Paola Farinelli for the switch design.

References

[1] M. DANESHMAND and D.R. MANSOUR, *Redundancy RF MEMS Multiport Switches and Switch Matrices*, IEEE Journal of MEMS **16**, pp. 296–303, 2007.

[2] W.A. de GROOT, J.R. WEBSTER, D. FELNHOFER, E.P. GUSEV, *Review of Device and Reliability Physics of Dielectrics in Electrostatically Driven MEMS Devices*, IEEE Transaction on Device and Materials Reliability **9**, pp.190–202, 2009.

[3] X. YUAN, Z. PENG, J.C.M. HWANG, D. FOREHAND, C.L. GOLDSMITH, *Acceleration of Dielectric Charging in RF MEMS Capacitive Switches*, IEEE Trans. on Device and Materials Reliability **6**(4), pp. 556–563, 2006.

[4] G. PAPAIOANNOU, M.-N. EXARCHOS, V. THEONAS, G. WANG, J. PAPAPOLYMEROU, *Temperature study of the dielectric polarization effects of capacitive RF MEMS switches*, IEEE Trans. on Microwave Theory and Techniques **53**(11), pp. 3467–3473, 2005.

[5] D. MARDIVIRIN A. POTHIER, A. CRUNTEANU, B. VIALLE, P. BLONDY, *Charging in Dielectricless Capacitive RF-MEMS Switches*, IEEE Trans. on Microwave Theory and Techniques. **57**(1), pp. 231–236, January, 2009.

[6] A. GRICHENER and G. REBEIZ, *High-Reliability RF-MEMS Switched Capacitors With Digital and Analog Tuning Characteristics*, IEEE Trans. on Microwave Theory and Techniques **58**(10), pp. 2692–2701, October, 2010.

[7] X. ROTTENBERG, H. JANSEN, P. FIORINI, W. De RAEDT, H.A.C. TILMANS, *Novel RF-MEMS capacitive switching structures*, Proc. European Microwave Conference, pp. 809–812, September 24-26, Milan, Italy, 2002.

[8] G. BARTOLUCCI, R. MARCELLI, S. CATONI, B. MARGESIN, F. GIACOMOZZI, V. MULLONI, P. FARINELLI, *An Equivalent Circuital Model for Shunt Connected Coplanar RF MEMS Switches*, J. Appl. Phys **104**(8), pp. 84514-1–8, 2008.

[9] F. GIACOMOZZI, V. MULLONI, S. COLPO, J. IANNACCI, B. MARGESIN, A. FAES, *A Flexible Fabrication Process for RF-MEMS Devices*, Rom. J. Inform. Sci. Tech. **14**(3), pp. 259–268, 2011.

[10] X. ROTTENBERG I. De WOLF, B.K.J.C. NAUWELAERS, W. De RAEDT and H.A.C. TILMANS *Analytical model of the DC actuation of electrostatic MEMS devices with distributed dielectric charging and nonplanar electrodes*, IEEE JMEMS **16**, pp. 1243–1253, 2007.

[11] F. SOLAZZI, G. RESTA, V. MULLONI, B. MARGESIN, P. FARINELLI, *Influence of beam geometry on the dielectric charging of RF MEMS switches*, Proc. 6th European Microwave Integrated Circuits Conference, pp. 398–401, Manchester, Oct 10-11, UK, 2011.

[12] X. YAN, W.L. BROWN, Y. LI, J. PAPAPOLYMEROU, C. PALEGO, J.C.M. HWANG, R.P. VINCI, *Anelastic Stress Relaxation in Gold Films and Its Impact on Restoring Forces in MEMS Devices*, IEEE JMEMS **18**, pp. 570–576, 2009.

[13] P. CZARNECKI, X. ROTTENBERG, P. SOUSSAN, P. NOLMANS, P. EKKELS, P. MULLER, H.A.C. TILMANS, W. De RAEDT, R. PUERS, L. MARCHAND, I. De WOLF *New Insights into Charging in Capacitive RF MEMS Switches*, IEEE 46th Annual International Reliability Physics Symposium, Phoenix, pp. 496–505, 2008.

Nonlinearity Determination and Linearity Degradation in RF MEMS Multi-Device Circuits

U. SHAH, M. STERNER and J. OBERHAMMER

Micro and Nanosystems, KTH Royal Institute of Technology,
Stockholm, Sweden

Abstract. This paper reports for the first time on RF nonlinearity analysis of complex multi-device RF MEMS circuits. The nonlinearity analysis is done for the two most commonly-used RF MEMS tuneable-circuit concepts, *i.e.* digital MEMS varactor banks and MEMS switched capacitor banks. In addition, the nonlinearity of a novel MEMS tuneable capacitor concept by the authors, based on a MEMS actuator with discrete tuning steps, is discussed. This paper presents closed-form analytical formulas for the IIP3 (nonlinearity) of the three MEMS multi-device circuit concepts, and an analysis of the nonlinearity based on measured device parameters (capacitance, gap), of the different concepts. Finally, this paper also investigates the effect of scaling of the circuit complexity, *i.e.* the degradation of the overall circuit linearity depending on the number of stages/bits of the MEMS-tuning circuit.

1. Introduction

RF MEMS components are especially of interest for reconfigurable/tuneable circuits for frequency-agile front end applications, due to their near-ideal signal handling behaviour, ultra-low power consumption, large bandwidth and easiness of integration, since fabrication is compatible to integrated circuits. The parallel-plate capacitive tuning principle is very widely used implementation for RF MEMS tuneable devices. Such MEMS tuneable capacitors are near-ideal tuning elements in filters, phase shifters, voltage-controlled oscillators, antennas and impedance-matching networks. RF circuits, including mobile phones, often operate up to power levels of 1W [1], and thus require high linearity to avoid signal degradation, in particular for the complex modulation schemes in modern, high data throughput, communication systems. High RF power implies high electrostatic forces on the mechanically-compliant MEMS-tuning mechanisms, which introduces intermodulation distortion (nonlinearity). Although these distortions may be quite small for a single device, they grow significantly for complex, multi-device RF

MEMS circuits. For instance, WiSpry's current generation mobile phone antenna tuner has an 80-element MEMS-switched capacitor bank [2].

The present paper reports for the first time on RF nonlinearity analysis of complex multi-device RF MEMS circuits. Previous nonlinearity reports were done for single-stage devices only [1], [3]. However, state-of-the-art RF MEMS circuits are composed of an increasing number of MEMS tuneable/switched stages, and it is important to analyse the overall nonlinearity of the entire RF MEMS circuit. In addition to digital MEMS varactor bank [4] and MEMS switched capacitor bank, the nonlinearity of a novel MEMS tuneable-capacitor concept by the authors [5], based on multiple discrete and well-defined steps, implemented by in-plane moving of the ground side-walls of a 3D micromachined coplanar waveguide transmission line is discussed. The paper also presents the closed-form analytical formulas for determining the overall IIP3 for any operation state the three discussed multi-device RF MEMS circuit concepts.

2. Analytical Formulas

This section includes the derivations of the IIP3 for the most commonly used multi-device RF MEMS capacitor circuits. The analytical derivation of IIP3 of a single RF MEMS shunt capacitor loaded on a transmission line is provided in [1]

$$IIP3 = \frac{2kg^2}{\phi C Z_0} = \frac{4kg^2}{\omega C^2 Z_0^2} \tag{1}$$

where k is the spring constant, g is the gap between the electrodes, ω is the angular frequency, C is the capacitance and Z_0 is the characteristic impedance. Since modern RF MEMS circuits are composed of many MEMS tuneable/switched stages, the above model need to extended to describe RF MEMS circuits with multiple devices, each contributing to the overall circuit nonlinearity. Firstly, the model is extended to two equal stages having similar capacitance, spring constant and gap values loaded on the same transmission line (*i.e.* both tuneable capacitances having the same configuration) which reduces the overall IIP3 by half compared to the previous case

$$IIP3 = \frac{2kg^2}{\phi C Z_0} = \frac{2kg^2}{\omega C^2 Z_0^2} \tag{2}$$

This case is then extended to a more general case of two capacitors with unequal stages, *i.e.* unequal capacitance, spring constant and gap values, resulting in

$$IIP3 = \frac{4kg_1 g_1^2 k_2 g_2^2}{\left[\omega C_1^2 \left(k_2 g_2^2\right) + \omega C_2^2 \left(k_1 g_1^2\right)\right] Z_0^2} \tag{3}$$

This leads to the derivation of the closed form analytical formula for *IIP3* calculations utilizing N-stage capacitor with unequal stages, or stages in different operation states:

$$IIP3 = \frac{4}{\omega Z_0^2}\left(\frac{1}{\sum_{i=1}^{N}\frac{C_i^2}{k_i\, g_i^2}}\right) \tag{4}$$

This can then be used as the basis for the derivation of *IIP3* for another most common circuit type where N-stages switched capacitors with fixed series capacitors are loaded on the transmission line to have a better control of the capacitance achieved in various states of the RF MEMS circuit.

$$IIP3 = \frac{4}{\omega Z_0^2}\left(\frac{1}{\sum_{i=1}^{N}\frac{C_{Si}^2}{k_i\, g_i^2}\left(\frac{C_{Fi}}{C_{Si}+C_{Fi}}\right)}\right) \tag{5}$$

3. Analysis of Circuit Examples

Figure 1 shows the three investigated RF MEMS-tuneable circuit concepts, (A) digital MEMS varactor bank which is used in distributed MEMS transmission line (DMTL) circuits, (B) MEMS switched capacitor bank which is extensively used in tuneable filters, and (C) multi-step MEMS capacitor which is a novel capacitor concept developed by the authors.

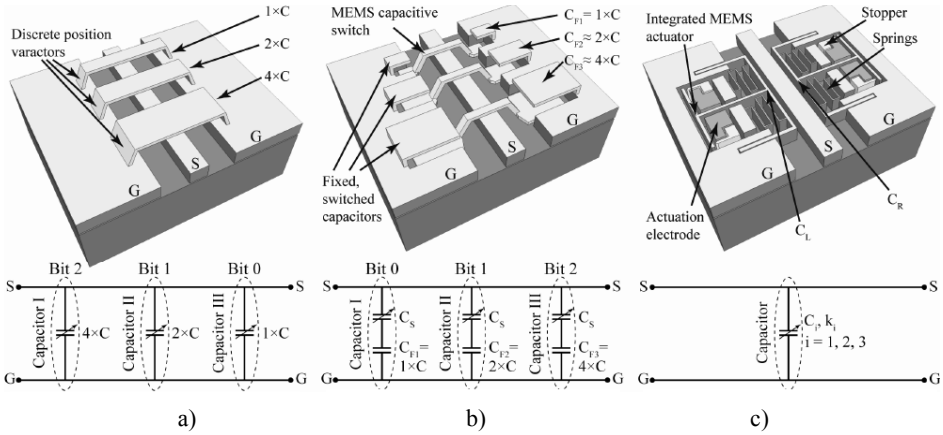

Fig. 1. 3D illustration and equivalent capacitor model: (a) Digital MEMS varactor bank; (b) MEMS switched capacitor bank and (c) multi-step MEMS capacitor.

A. Digital MEMS Varactor Bank

The data for the analysis of digital MEMS varactor bank is based on a published RF MEMS circuit from [4]. The varactors have two discrete positions each with a capacitance ratio of around 3. The total capacitance of the circuit can be tuned from 146 fF to 430 fF in eight discrete states. Table 1 shows the device parameters used for the calculation of the IIP3 for each state. Equation (4) is used to calculate the *IIP3* of the varactor bank in each of the 8 states. Figure 2 show the calculated *IIP3* at 2.5 GHz for all 8 states of the two 3-bit MEMS-tuneable circuit concepts.

The non-linearity is increasing (*i.e. IIP3* is decreasing) with increasing number of activated stages, weighted by the capacitance/gap (C/g) ratio of the individual stages.

Table 1. Summary of parameters of digital MEMS Varactor bank (circuit type a) used for linearity Analysis, based on [4].

Parameter	Capacitor I	Capacitor II	Capacitor III
C_{up} (fF)	63	45	38
C_{down} (fF)	205	145	80
g_{up} (μm)	1.5	1.5	1.5
g_{down} (μm)	0.5	0.5	0.5
k_{up} (N/m)	12	12	12
k_{down} (N/m)	55	55	55

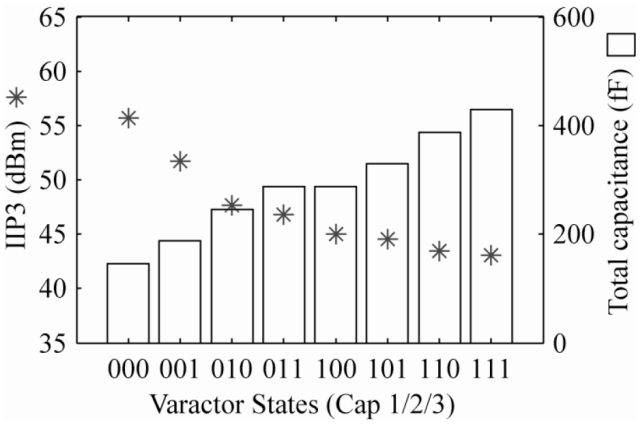

Fig. 2. *IIP3* analysis and measured capacitance for each state of the digital MEMS varactor bank (circuit type A).

B. MEMS Switched Capacitor Bank

The MEMS switched capacitor bank with a metal-air-metal fixed capacitor in series with each MEMS capacitive switch is shown in Fig. 1(b). This example uses a 3-bit MEMS switched capacitor bank where three MEMS switch and fixed

capacitor combinations are arranged along the length of the transmission line. The values of the fixed capacitors are binary coded, *i.e.* doubled from the smallest to the next higher stage. The device parameters used for the nonlinearity analysis are shown in Table 2. Equation (5) is used to calculate the *IIP3* of the switched capacitor bank in each of the 8 states. Fig. 3 shows the calculated *IIP3* for various states of the bank. It can be seen here that the non-linearity is increasing with increasing number of activated stages, weighted by the capacitance/gap (C/g) ratio of the individual stages.

Table 2. Summary of parameters of digital MEMS varactor bank used for linearity analysis (circuit type b)

Parameter	Capacitor I	Capacitor II	Capacitor III
$C_{S,up}$ (fF)	88.5	88.5	88.5
$C_{S,down}$ (fF)	885	885	885
C_F (fF)	160	320	640
$g_{S,up}$ (μm)	2	2	2
$g_{S,down}$ (μm)	0.2	0.2	0.2
k_{up} (N/m)	32	32	32
k_{down} (N/m)	586.5	586.5	586.5

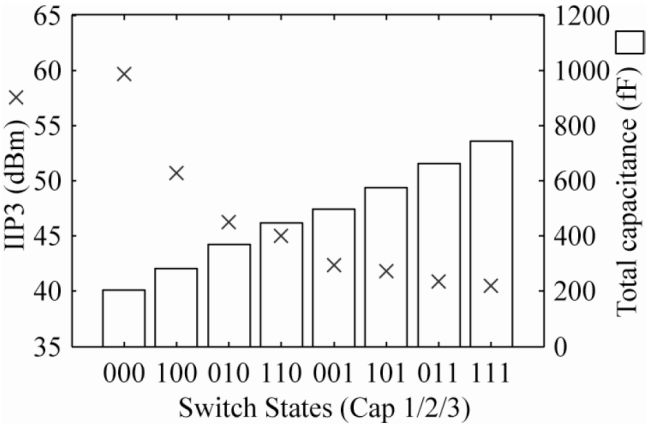

Fig. 3. *IIP3* analysis and capacitance for each state of the MEMS switched capacitor bank (circuit type B).

C. Multi-step MEMS Capacitor

For the discrete multi-step MEMS capacitor previously published by the authors [5] and shown in Fig. 1(c), the non-linearity analysis is shown in Fig. 4, based on the measured parameters given in Table 3 [5]. This capacitor utilizes a 3D-micromachined transmission line embedded tuning mechanism, where integrated MEMS actuators are moving the sidewalls of the 3D-transmission line, resulting in

a modulation of the capacitive loading of the line. The mechanical springs are completely decoupled from the RF signal, *i.e*., the RF ground signal is coupled capacitively from the fixed ground layer to the moving ground sidewall, and the mechanical springs are connected to isolated islands behind the moving sidewalls.

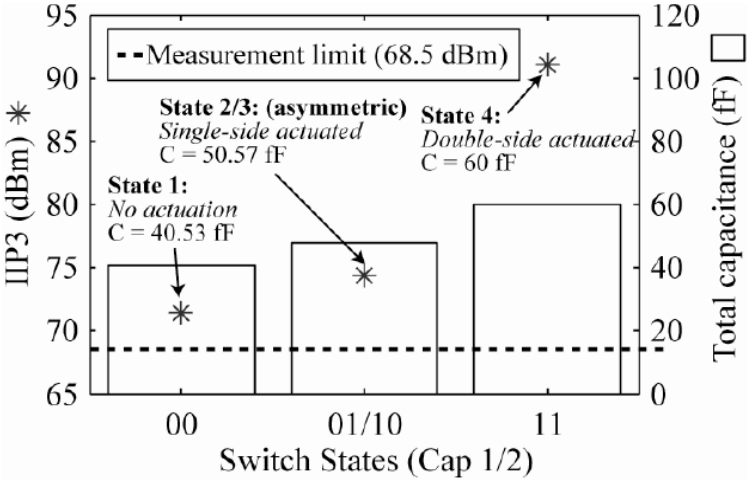

Fig. 4. *IIP3* analysis and measured capacitance for each state of the multi-step MEMS capacitor (circuit type C).

Table 3. Summary of parameters of multi-step MEMS capacitor used for linearity analysis (circuit type C)

Parameter	State I	State II/III	State IV
C_L (fF)	20.27	20.27	30
C_R(fF)	20.27	30	30
g_L (µm)	4.4	4.4	2
g_R (µm)	4.4	2	2
k_L (N/m)	5.8	5.8	5650
k_R (N/m)	5.8	5650	5650

This result in low series resistance, and thus low insertion loss and high Q of 88 measured at 40 GHz in a weakly-coupled transmission line resonator, which is very high for a tuneable device. The ground sidewall section is moved uniformly over its entire length. The device is actuated by applying a voltage between the actuation electrode and the anchors connected to the springs, *i.e*. no DC bias or reference ground is shared with any RF potential, neither the RF ground nor the signal line. More actuator stages can also be integrated for this design resulting in additional states of the capacitor and extended tuning range [6]. The fabricated prototype is

shown in Fig. 5. For this circuit, the calculated *IIP3* values at 2.5 GHz are much higher due to the much smaller C/g ratio of this concept. In addition to the calculated *IIP3* from the measured RF capacitances, the *IIP3* of this device was measured using dual-tone measurement technique, but the measurement setup had an upper limitation of 68.5 dBm for all states as shown in Fig. 6, and the expected *IIP3* are clearly above that limit.

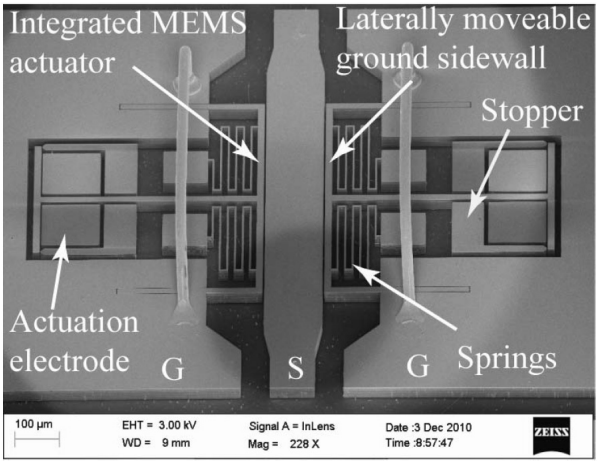

Fig. 5. SEM picture of the fabricated multi-step MEMS capacitor (circuit type C).

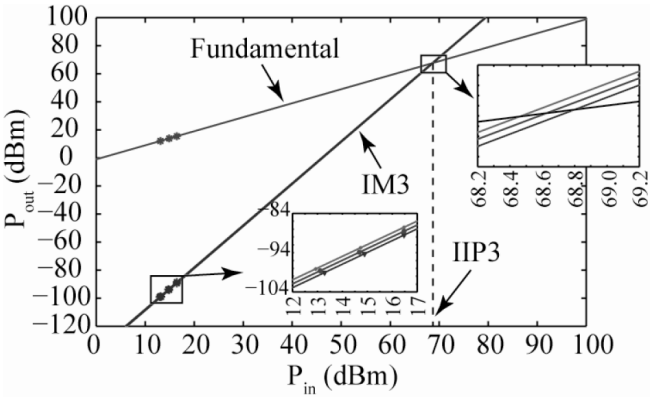

Fig. 6. Measured dual-tone fundamental and intermodulation levels with *IIP3* point of the two-stage multi-step MEMS capacitor (circuit type C).

4. Scaling of Linearity With Circuit Complexity

Finally, the effect on the IIP3 when scaling the circuit complexity was analysed for the digital MEMS varactor bank and MEMS switched capacitor bank. Fig. 7

shows the signal power limit for tolerating a nonlinearity degree of 1% intermodulation for circuits with 1 to 5 stages (=bits), shown for the worst-case bit combination *i.e*. shown for the operation state of the circuit which has the worst linearity. The signal power allowed for limiting the non-linearity distortion is significantly decreasing with increasing number of stages, which has to be taken into account in multi-devices RF MEMS circuit designs.

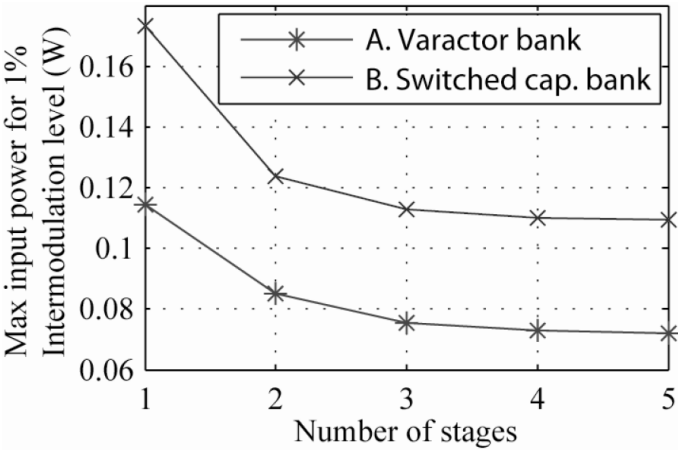

Fig. 7. Scaling of 1%-intermodulation power (for worst-case state), for increasing circuit complexity from 1 to 5 bits (for A, B).

5. Conclusion

Closed form analytical formals have been derived and presented for calculating the IIP3 for various multi-device RF MEMS circuits. The RF nonlinearity analysis for three different multi-device RF MEMS circuits *i.e*. digital MEMS varactor bank, MEMS switched capacitor bank and multi-step MEMS capacitor, was performed along with IIP3 measurements on the prototype of a novel multi-step MEMS capacitor. Finally, the scaling of the linearity with the circuit complexity was analysed.

Acknowledgements. The authors would like to thank Jan Åberg from Micro-Comp Nordic AB, Stockholm, Sweden, for his help with the nonlinearity measurement setup and for providing essential equipment.

References

[1] L. DUSSOPT and G.M. REBEIZ, *Intermodulation distortion and power handling in RF MEMS switches, varactors and tunable filters*, IEEE Trans. Microw. Theory Tech. **51**(4), pp. 1247–1256, Apr. 2003.

[2] A.S. MORRIS, Q. GU, M. OZKAR and S. P. NATARAJAN, *High performance tuners for handsets*, IEEE MTT-S Int. Microwave Symp. Dig., pp. 1–4, Baltimore, June, 2011.

[3] C.D. PATEL and G.M. REBEIZ, *A high-reliability, high-linearity, high power RF MEMS metal contact switch for DC-40 GHz applications*, IEEE Trans. Microw. Theory Tech. **60**(10), pp. 3096–3112, October, 2012.

[4] L. DUSSOPT and G.M. REIBEIZ, *An X- to Ku-band 3-bit digital MEMS varactor*, IEEE Microw. Wireless Compon. Lett. **13**(9), pp. 361–363, September, 2003.

[5] U. SHAH, M. STERNER and J. OBERHAMMER, *Basic concepts of moving sidewall tuneable capacitors for RF MEMS reconfigurable filters*, Proc. European Microw. Conf., pp. 1087–1090, Manchester, December, 2011.

[6] U. SHAH, M. STERNER, G. STEMME and J. OBERHAMMER, *Multi-position large tuning-range digitally tuneable capacitors embedded in 3D micromachined transmission lines*, IEEE Int. Conf. Micro Electro Mechanical Systems, pp. 165–168, Cancun, March, 2011.

Comparative Study of Contacted and Contact Less Charging in RF MEMS Capacitive Switches

M. KOUTSOURELI[1], L. MICHALAS[1], P. MARTINS[2],
E. PAPANDREOU[1], A. LEULIET[2], S. BANSROPUN[2],
G. PAPAIOANNOU[1], A. ZIAEI[2]

[1]University of Athens, Physics Department, 15784,
Panepistimiopolis Zografos, Athens, Greece
Phone:+302107276817
[2]Thales Research & Technology, F91767,
Palaiseau Cedex, France
Phone: +33 1 69415777

Abstract. The dielectric charging in MEMS capacitive switches is complex effect. The high electric field during pull-down causes intrinsic free charge migration and dipole orientation sa well as charge injection. The macroscopic dipole moment of the first two mechanisms is opposite to the one arising from charge injection. This cause partial compensation hence mitigates the overall charging and increases the device lifetime. The charging due to intrinsic free charge migration and dipole orientation in the pull-up state. The paper investigates the characteristics of contactless charging and compares them with the ones of contacted charging. The impact of electric field intensity and stress time duration on the contactless charging are also investigated.

1. Introduction

Micro-Electro-Mechanical-Systems (MEMS) technology has already emerged as an enabling technology for a new generation of high-performance RF components such as RF MEMS switches, tunable capacitors and inductors. In addition, RF MEMS components can be fully integrated with monolithic microwave integrated circuits and therefore can potentially lead to systems with small size, lighter weight, low power consumption and mass production [1, 2]. Among the mentioned RF MEMS devices, the MEMS capacitive switch is a key device due to its unique RF performance compared to the current existing devices. The unique characteristics of MEMS capacitive switches makes them ideal candidates for integration into passive circuits, such as phase shifters or tunable

filters, for implementation in many terrestrial and space applications, including portable telecommunication, wireless computer networks, reconfigurable antennas and others.

However, the commercialization of the electrostatic MEMS capacitive switch is still hindered by reliability issues, especially the dielectric charging phenomenon [3, 4]. The dielectric charging has been principally monitored through the number of switching cycles for different operating bias [5] and ambient conditions [6, 7] and dielectric materials and substrates, a detailed presentation of all these being given in [8, 9].

Regarding the dielectric charging mechanisms two mechanisms have been identified up to now, the contacted charging where charges are injected under the presence of high electric field during the pull-down state and the contactless one where charging is induced under the presence of much lower electric field intensity with the moving armature being still in the pull-upstate[10]. The later has been shown to have polarity opposite of the contacted one [10] thus giving rise to a compensation mechanism, but the effect has not been further investigated.

Taking these into account the present paper aims to provide a better knowledge of the characteristics of the two mechanisms presenting information on the characteristic time constants and charging/discharging current magnitudes. This in turn will allow the understanding of the degree of compensation process, hence the mitigation of dielectric charging by proper engineering of the dielectric material.

2. Theoretical Background

A. Charging Mechanism

In principle the charging/polarization of a dielectric material is achieved through two basic processes: i) the contact-less, termed as blocking contacts polarization [11], where the electrodes generating the electric field are not in contact with the film, hence no charge is injected and ii) the contacted one where the dielectric film is in contact with the electrodes generating the electric field allowing charge injection (Fig. 1). In the first case the charging arises only from dipole orientation and intrinsic free charge displacement while in the second case the charge injection provides an additional mechanism to overall charging (Fig. 1). The two mechanisms that is the dipole orientation and intrinsic free charge displacement give rise to same polarity charging and the contribution of each mechanism can be identified with methods based on DC and AC characterization.

In a MEMS capacitive switch the first mechanism, the contact-less charging, is monitored under low electric field intensities because the moving armature has to be in the pull-up state [11] in order to avoid charge injection. Both mechanisms, the contact-less and contacted charging occur under the presence of the high electric field intensities during pull-down state. In the specific case of capacitive switches with stiff bridge and therefore with large pull-down voltage, the case of power

devices operating at bias levels close but below pull-down, field emission may occur. Then charges may be inject into dielectric film and give rise to "contacted" charging while the moving armature is still in the pull-up state [12, 13]. Here it must be pointed out that this condition can be achieved by the superposition of power RF signal and under due to the different work functions of the moving armature metal and dielectric film composition may give rise to charging current that will affect the rate of the shift of pull-down and pull-up voltages with the number of cycles and therefore the lifetime of switches.

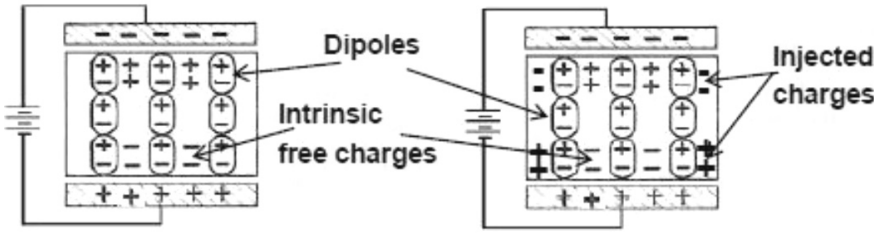

Fig. 1. (a) Contact-less and (b) contacted charging.

B. Kelvin Probe Method in MEMS

The bulk discharge current transient in a MEMS capacitive switch is determined using the device model proposed in [14, 15], which includes a fixed non-flat metal plate of area A covered with a dielectric film of uniform thickness $d\varepsilon$, dielectric constant ε_r. In the general case of distributed equivalent charge and air gap [16], the bias at which the up-state capacitance attains its minimum (V_{min}) is the one for which the electrostatic force attains minimum. For small bridge up-state deformation the capacitance variance can be considered low the bias for capacitance minimum is given by:

$$V_{\min} = \frac{\mathrm{d}_{\varepsilon}}{\varepsilon_r \, \varepsilon_0} \, \mu_{\psi} + V_{offset} \tag{1}$$

where μ_{ψ} represents the mean value of the equivalent surface charge distribution of the dielectric film and V_{offset} arises from background charging of substrate [17], ESD etc. The value of V_{min} will shift after each stress step, the shift being determined by the stressing time or number of cycles and the applied electric field intensity. The value of Vmin will shift will also shift during discharge.

Taking all this into account the calculated net charging (J_{ch}) or discharging (J_{disch}) current density will be given by:

$$J_{ch,disch} = \frac{\mathrm{d}\mu_{\psi}}{\mathrm{d}t} = \frac{\varepsilon_r \, \varepsilon_0}{\mathrm{d}_{\varepsilon}} \cdot \frac{\mathrm{d}V_{\min}(t)}{\mathrm{d}t} \tag{2}$$

which describes the average value of current density due to charge injection and storage or charge collection by the bottom electrode. Moreover, the stored or

collected charge density σ_{ch} or σ_{disch}, can be calculated by integrating the discharge current density within the time window of observation:

$$\sigma_{ch,disch} = \int_{to}^{t} J_{ch,disch} \cdot \mathrm{d}t \tag{3}$$

3. Experimental Procedure

The switches measured are bridge-type capacitive switches with 70 nm thick SiNx dielectric film, deposited with PECVD method at 350°C. The membrane is suspended about 2 μm above the dielectric in the unactuated position and the active area is about 1.3×10^{-4} cm^2. The devices used in the present work were selected for low pull-down voltage, $V_{pd} \cong 13$ V, in order to avoid excess charging during contacted stress. For the contacted charging the devices were stressed for a total time of 1020 sec in steps of 30 sec at 15 V. The contactless charging was performed under bias of +8 V and for a total time of 7200 sec in steps of 900 sec. After stress the devices were assessed by obtaining the C-V characteristics in the up state for 5500 s in order to monitor the shift of the bias for minimum capacitance towards the pre-stress level.

The charging and discharging processes have been monitored through the bias for up-state capacitance minimum with the aid of a with a Boonton 72 B capacitance meter while sweeping the voltage in 50 mV steps and the acquired bias was applied by a 6487 Keithley voltage source-picoampere meter. Here it must be pointed out that the measured capacitance included the parasitic one induced by the low frequency probes. The minimum was determined by fitting a parabola to the experimental data, assuming a small capacitance variance in order to take advantage of [16] to derive Eqs. 1, 2. Finally, all measurements have been performed in vacuum with the sample annealed in vacuum at temperature of 140°C for two hours in order to avoid any interference from humidity.

4. Results and Discussion

The shift of the capacitance-voltage characteristic with stress time for contactless charging is shown in Fig. 2.

The contactless charging was performed under a of +8 Volt that corresponds to applied electric field of the order of 4×10^4 V/cm resulting in a shift to more negative voltages. For contacted charging the devices have been stressed under bias of +15 Volt that corresponds to electric field of the order of 2.1×10^6 V/cm.

The shift of the bias for capacitance minimum for contactless and contacted charging is shown in Fig. 3a and 3b respectively. Due to the large difference of stressing electric fields the shift is larger and faster for contacted charging with respect to the shift for contactless charging. It is important to emphasize that during contactless charging the dipole orientation and charge translation will decrease the

internal electric field intensity that in turn will decrease the dipoles alignment and free charge translation rate with time (Fig. 3a).

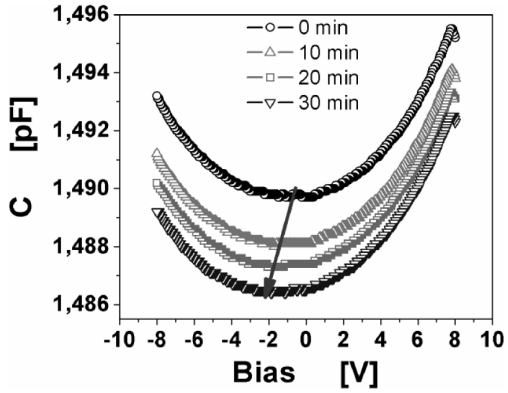

Fig. 2. Shift of capacitance-voltage characteristic after successive contactless charging.

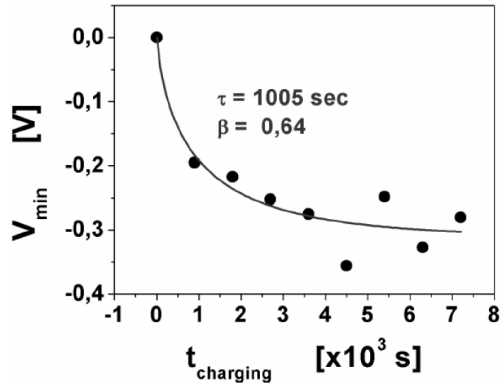

a)

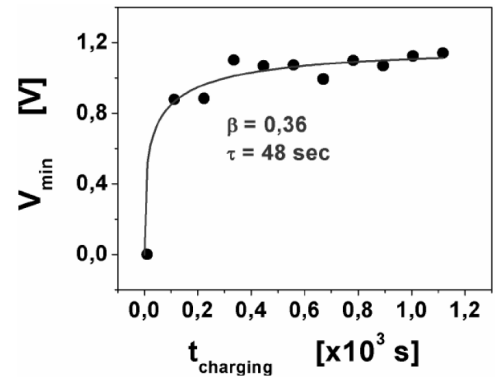

b)

Fig. 3. Shift of the bias for capacitance minimum for (a) contactless and (b) contacted charging.

On the other hand in the case of contacted charging the electric field at the dielectric-metallic contact decreases with charging time hence decreasing the rate charge build-up in the dielectric (Fig. 3b). These charging processes including the effect of charge trapping, hopping [18] and percolation will lead to a macroscopic behavior that macroscopically obeys the stretched exponential law [14, 15] with time constants of 48 sec and 1005 sec for the contacted and contactless charging respectively. The low value of charging time can be attributed to the large applied electric field and mainly to the short observation time window. According to these the charging current for each process will decrease exponentially with time with corresponding time constants of 104 sec and 4425 sec for the contacted and contactless charging respectively (Fig. 4). The total equivalent charge has been calculated from Eq. 3 and leads to 8.85×10^{-8} C/cm^2 and 2.45×10^{-8} C/cm^2 for the contacted can contactless charging.

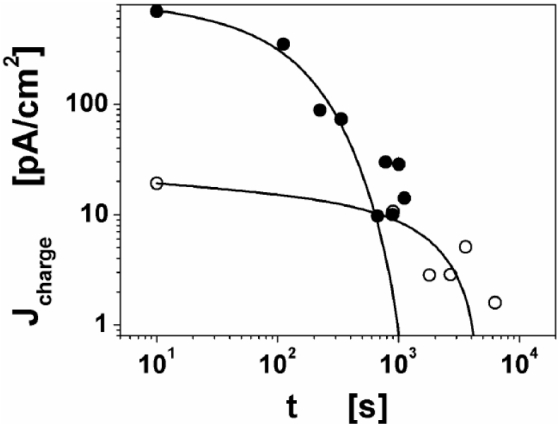

Fig. 4. Charging current densities for (o) contactless and (●) contacted charging.

It is interesting to notice that the equivalent charge for the contactless charging, although accumulated in a long time ~ 7200 sec, is non negligible compared to the one from contacted one. Although in a long term contacted charging it is expected to accumulate large amount of charge the calculated one for contactless charging raises the question of for the prospect of an effective compensation that would result in a longer lifetime. This can only be achieved if the contactless charging will arise from dipole orientation or ion translation since the charging from free charge translation will be immediately annealed.

6. Conclusion

The present paper investigates and correlates the properties of contacted and contactless charging that occurs in the dielectric films of MEMS capacitive

switches. Charge accumulation follows stretched exponential law for both contacted and contactless charging processes. The characteristic time of contacted charging has been found to be much smaller than the corresponding time of contactless charging and the magnitude of the charging current is much larger for the case of contacted charging. Despite these, the equivalent charge density for the two processes has been found to be similar in magnitude. Finally, the discharge process that follows contactless charging has the same characteristics with the one that follows contacted charging, since the charge collection mechanism depends on the properties of the dielectric material and both take place under relatively low electric fields.

Acknowledgements. The present work has been supported by FP7 project: *Nanostructured materials and RF-MEMS RFIC/MMIC technologies for highly adaptive and reliable RF systems*, NANOTEC Grant agreement no: 288531.

References

[1] Z. YAO, J. Micromech. Microeng. **10**, pp. R9, 2000.

[2] G.M. REBEIZ, (Ed.) RF MEMS Theory, Design and Technology, Hoboken, NJ: Wiley, 2003.

[3] J. WIBBELER, G. PFEIFER and M. HIETSCHOLD, *Parasitic charging of dielectric surfaces in capacitive microelectromechanical systems (MEMS)*, Sensors Actuators **A71**, pp. 74–80, 1998.

[4] C. GOLDSMITH, J. EHMKE, A. MALCZEWSKI, B. PILLANS, S. ESHELMAN, Z. YAO, J. BRANK and M. EBERLY, *Lifetime Characterization of Capacitive RF MEMS Switches*, IEEE International Microwave Symposium **1**, pp. 227–230, May, 2001.

[5] P. CZARNECKI, X. ROTTENBERG, R. PUERS, I. De WOLF, *Effect of gas pressure on the lifetime of capacitive RF MEMS switches*, 19th IEEE International Conference on Micro Electro Mechanical Systems, MEMS, pp. 890–893, Istanbul, 2006.

[6] U. ZAGHLOUL, B. BHUSHAN, P. PONS, G.J. PAPAIOANNOU, F. COCCETTI and R. PLANA, *On the influence of environment gases, relative humidity and gas purification on dielectric charging/discharging processes in electrostatically driven MEMS/NEMS devices*, Nanotechnology **22**, pp. 035705, 2011.

[7] J. RUAN, E. PAPANDREOU, M. LAMHAMDI, M. KOUTSOURELI, F. COCCETTI, P. PONS, G. PAPAIOANNOU, R. PLANA, *Alpha particle radiation effects in RF MEMS capacitive switches*, Microelectronics Reliability **48**, pp. 1241–1244, 2008.

[8] G. PAPAIOANNOU, *Advanced RF MEMS*, Ch. 6, S. Lucyszyn (Ed.) The Cambridge RF and Microwave Engineering Series, August, 2010.

[9] WM. van SPENGEN, *Capacitive RF MEMS switch dielectric charging and reliability: a critical review with recommendations*, J. Micromech. Microeng. **22**, pp. 074001, 2012.

[10] G. PAPAIOANNOU, G. WANG, D. BESSAS and J. PAPAPOLYMEROU, *Contactless Dielectric Charging Mechanisms in RF-MEMS Capacitive Switches*, European Microwave Week, pp. 513–516, 11-13 Sept., 2006.

[11] J. VANDERSHUEREN and J. CASIOT, In: Braunlich P (Ed.) Topics in Applied Physics: *Thermally stimulated relaxation in solids*, Springer-Verlag **37**, ch. 4, pp. 135, Berlin, 1979,

[12] A. GARG, A. VENKATTRAMAN, A. KOVACS, A. ALEXEENKO, D. PEROULIS, *Direct measurements of field emission currents in e-static MEMS structures*, IEEE MEMS Conf, pp. 412–5, 2011.

[13] L. MICHALAS, A. GARG, A. VENKATTRAMAN, M. KOUTSOURELI, A. ALEXEENKO, D. PEROULIS and G. PAPAIOANNOU, *A study of field emission process in electrostatically actuated MEMS switches*, Microelectronics Reliability **52**, pp. 2267–2271, 2012.

[14] M. KOUTSOURELI, G. PAPAIOANNOU, *Determination of long time discharge current in microelectromechanical system capacitive switches*, Appl Phys Lett. **99**, pp. 103503, 2011.

[15] M. KOUTSOURELI, L. MICHALAS, G. PAPAIOANNOU, *Temperature effects on the bulk discharge current of dielectric films of MEMS*, Microelectronics Reliability **52**, pp. 2240–2244, 2012.

[16] X. ROTTENBERG, I. De WOLF, B.K.J.C. NAUWELAERS, W. De RAEDT, H.A.C. TILMANS, *Analytical Model of the DC Actuation of Electrostatic MEMS Devices With Distributed Dielectric Charging and Nonplanar Electrodes*, J Microelectromech Syst **16**, pp. 1243–53, 2007.

[17] P. CZARNECKI, X. ROTTENBERG, P. SOUSSAN, P. EKKELS, P. MULLER, P. NOLMANS, W. DE RAEDT, H.A.C. TILMANS, R. PUERS, L. MARCHANDC and I. De WOLF, *Effect of substrate charging on the reliability of capacitive RF MEMS switches*, Sensors and Actuators **A**: Physical **154**, pp. 261–268, 2009.

[18] M. KOUTSOURELI, L. MICHALAS, G. PAPAIOANNOU, IEEE international reliability physics symposium (IRPS), Anaheim, CA, USA, April 15–19, 2012.

Sensitivity, Repeatability and Lateral Scanning Resolution of Micromachined Near-Field Millimeter-Wave Probe for Skin Cancer Diagnosis

Fritzi TÖPFER, Sergey DUDOROV and Joachim OBERHAMMER

KTH Royal Institute of Technology, Stockholm, Sweden

Abstract. This paper reports for the first time on the 2-dimensional scanning performance of a micromachined millimeter-wave (100 GHz) near-field probe with a substantially reduced tip size which is designed for skin cancer diagnosis. Furthermore, it introduces a novel concept of creating inhomogeneous test samples with tailor-made and locally altered permittivity which mimick skin tissue with small anomalies and are used for characterizing the probe. A probe prototype with a tip size of 300 × 600 μm^2 and test samples with permittivity in the range of cancerous and healthy skin tissue were fabricated by micromachining and used for evaluating the sensitivity and resolution of the probe. This paper reports for the first time on 2-dimensional scanning performance, resolution, repeatability, long-term stability, and sensitivity, which are important for qualifying such measurement probes for medical applications. The resolution of the prototype, which is important for early detection of small tumor speckles, was found to be better than 200 μm, *i.e.* 1/6 of the medium-normalized wavelength. The reproducibility of the probe setup including operator uncertainty is 1.36% (1σ) and the long term stability of reference measurements is 0.59% (1σ) over hours.

1. Introduction

A. Medical Motivation

Skin cancer is the most common cancer in North America and Europe. More than two million cases of basal cell carcinoma and squamous cell carcinoma and more than 75.000 new cases of melanoma and 9000 deaths from melanoma are estimated for the USA alone in 2012. Deaths from melanoma, the skin tumor most likely to metastasize, increases with the highest rate of all cancer types [1], [2].

It is estimated that to diagnose one melanoma 50 to 250 people need to be screened. As of today, there exists no reliable skin cancer sensor technology and diagnosis is still done by visual inspection, which is time consuming and can only

be done by highly trained specialists. This results in long waiting times for the patients, thus late diagnosis and high mortality, besides high costs for the public health care systems.

B. Measurement Principle

Cancer tissue has a higher water content than healthy tissue [3] resulting in a different microwave signature. Therefore, microwave reflection (S11) measurements have been found to be able to discriminate cancer tissue [4], including skin cancer [5]. Conventional open-and waveguide probes have proven the measurement concept on skin [6], but have an insufficient resolution for detecting skin cancer at an early stage.

C. Need for Miniaturized Probe

Detection at an early state, when the tumor is small and its thickness has still not exceeded several hundred micrometers, is crucial, because the probability of metastasis and thus mortality increases drastically with increasing tumor size. The size of an open rectangular waveguide probe in the W-band is of the same magnitude as the wavelength and thus often too large for significantly discriminating inhomogeneous skin cancer speckles. Beside insufficient lateral resolution, the large size also results in a too deep main interaction volume and the measurement of the average properties of several skin layers impedes the discrimination of shallow tumor layers (Fig. 1). Therefore there is a need for a miniaturized near-field probe which achieves high resolution, both laterally and vertically, and at the same time high energy-coupling into the dielectric test material, *i.e*. high sensitivity.

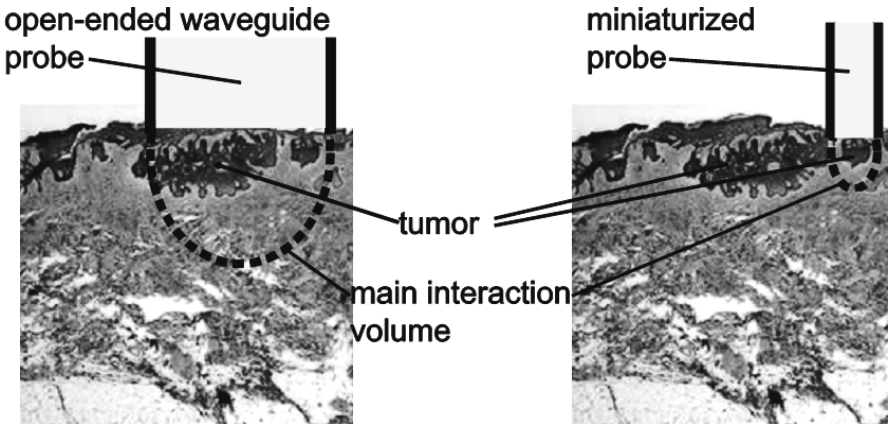

Fig. 1. Microwave interaction volume for different probe sizes: (left) conventional probe, not resolving small tumor speckles; (right) proposed miniaturized probe: high lateral resolution and penetration depth adapted to early-stage skin-cancer size.

2. Micromachined Millimeter-Wave Probe Design and Fabrication

The millimeter-wave near-field probe consists of a metallized high-resistivity silicon-core dielectric-rod waveguide, which is tapered towards the probe tip (Fig. 2). The tapering results in a tip size of 600 μm × 300 μm, which is only 6% of the area of an open-end waveguide probe in the same frequency range. The dielectric-rod waveguide is fed through an optimized dielectric wedge transition from a standard WR-10 waveguide connected to a 75–110 GHz vector network analyzer. It is held in place in the center of the WR-10 waveguide by a holder, which is fabricated by micromachining to assure high precision in the positioning of the probe within the waveguide, which is important for a good transmission of the electromagnetic wave. The design results in high resolution without compromising in sensitivity, *i.e.* energy-coupling into the dielectric test material. The basic probe concept was recently presented by the authors [7]. For the measurements presented in this paper a new prototype with improved tolerances resulting in higher measurement reproducibility was fabricated.

Both the probe and the holder are fabricated from a 600 thick high-resistivity silicon substrate wafer by through-wafer deep reactive ion etching and subsequent 4-side metallization in an electron-beam evaporator utilizing a shadow mask (Fig. 3).

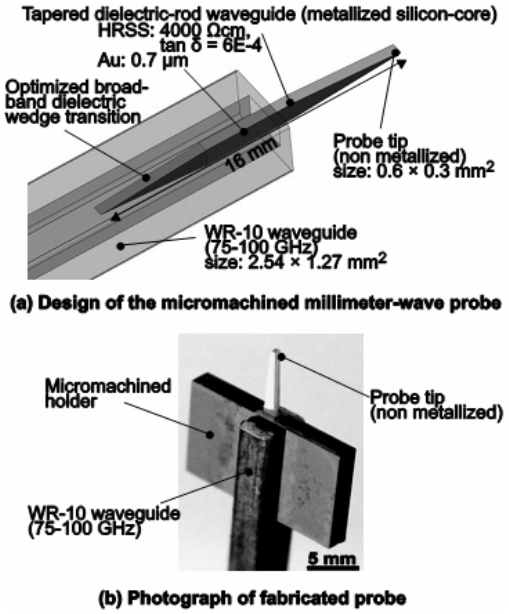

Fig. 2. Near-field measurement probe design for W-band (75 to 110 GHz); fed from a waveguide *via* a dielectric wedge transition, and fixated with a micromachined holder. The tapered probe tip combines high sensitivity and sub-wavelength resolution.

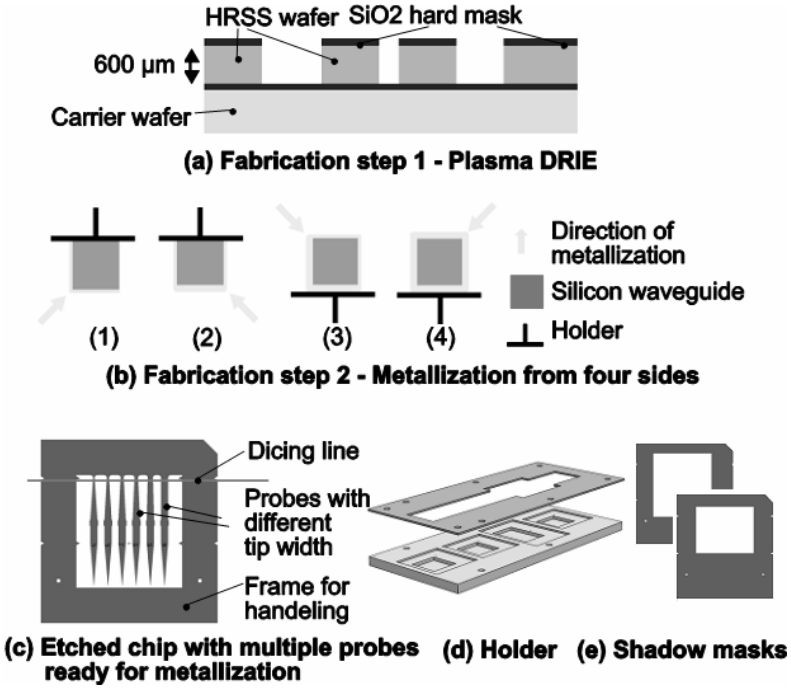

Fig. 3. Fabrication: The two major steps are: (a) through-wafer deep reactive ion etching using SiO_2 hard mask; (b) 4-side shadow-mask gold metallization by evaporation; metallization is accomplished by: (c) single probes are on a connecting frame during metallization and diced out subsequently; (d) special sample holder for shadow-mask metallization; (e) shadow masks for metallization.

3. 2d-Scanning Measurement Setup and Micromachined Test Samples

For probe characterization, special micromachined test and calibration samples with tailor-made effective permittivity were fabricated from 350 µm thick Si-wafers by etching a periodic pattern (pitch p) of sub-wavelength sized holes. The size of the holes (h) determines the relative permittivity of the sample and by using wafers with different conductivity different loss factors can be obtained. These test samples allow for mimicking the microwave properties of tissue of varying water content, and, in contrast to conventional phantom materials or tissue samples, guarantee for high reproducibility which is important especially for initial sensor development.

Furthermore, with this new method micromachined test samples can be created with any given pattern of locally modulated permittivity, which can be used for investigating the 2-dimensional scanning performance.

For the measurements the WR-10 waveguide with the inserted probe is connected to an Agilent E8163A *Vector Network Analyzer* (VNA) with

measurement heads up to 110 GHz. The probe tip is put in contact with the sample and the reflections S11 are measured. Sample and probe are placed on an x-y-z stage and can be moved in a precise manner for instance to scan the probe tip over the test sample with locally varied permittivity (Fig. 4).

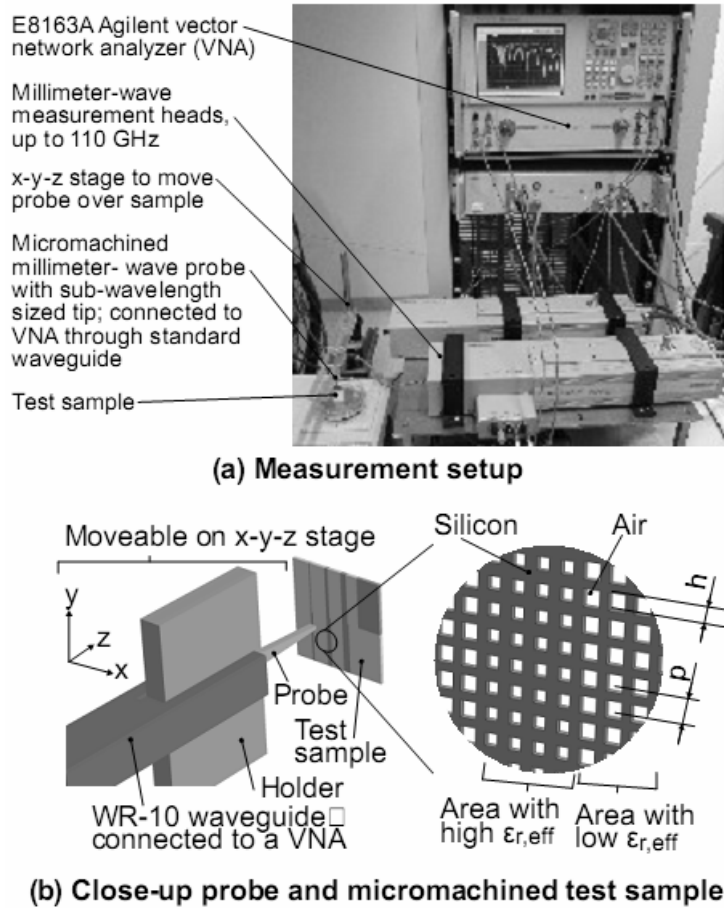

Fig. 4. (a) Setup for reflection (S11) measurement: the WR-10 waveguide with probe tip, connected to a vector network analyzer, is moveable on x-y-z stage, and scanning in contact over the sample surface; (b) probe and permittivity test samples; the samples are fabricated from a 350 μm thick silicon wafer; a regular pattern of holes is etched by DRIE for tailer-made, locally modulated permittivity, determined by the ratio between hole size h and pitch p, mimimicking skin anomalies.

4. Measurement Results

Reflection measurements were performed on uniform micromachined test samples with tailor-made permittivity ranging from $\varepsilon_{r,eff} = 3.5$ to $\varepsilon_{r,eff} = 6.7$ at

100 GHz. Ten measurements were done per sample and the probe tip was positioned at a different spot on the test sample for every single measurement. Reference measurements against air were taken after every fifth measurement.

Figure 5 shows the measured reflections S11 on the different test samples. Test samples with different permittivity have different reflection levels and samples with permittivity in the range of skin-cancer tissue ($\varepsilon_r = 6.5$ according to 2nd-order Debye-model [8]) and healthy tissue ($\varepsilon_r = 5.5$), can clearly be distinguished. The differences between the measurements of one sample are mainly operator-influenced and caused by insufficient contact between sample and probe tip. The operator-influenced short-term repeatability on test samples was characterized to 1.36% (1σ) of the power level. Figure 6 shows the long-term repeatability of the setup over 8 hours for operator-independent air-reference measurements performed between sample measurements, which is 0.59% (1σ) of the power level.

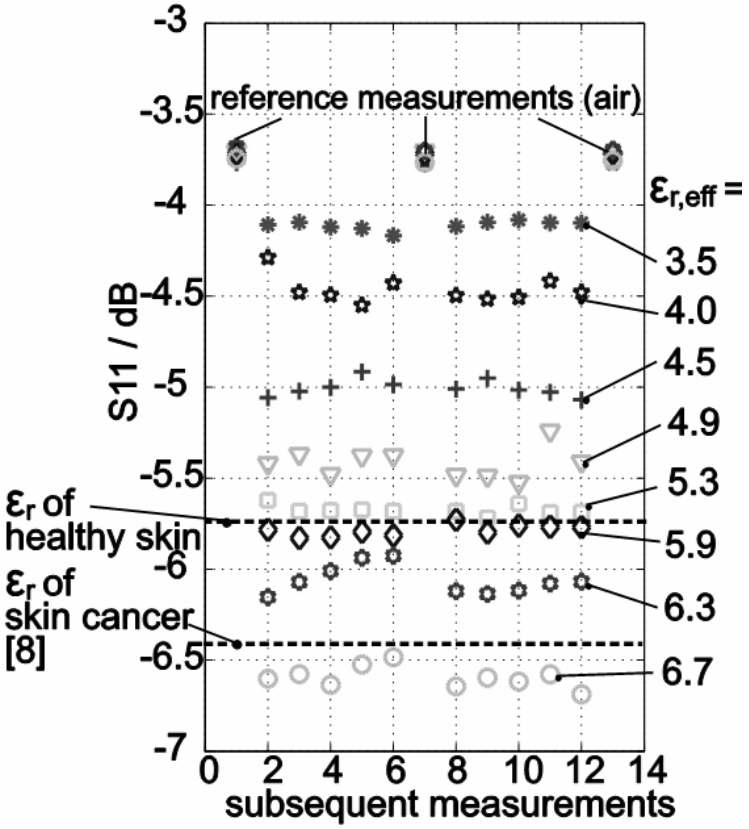

Fig. 5. Measured reflection (S11) at 100 GHz on 8 test samples of different effective relative permittivity $\varepsilon_{r,eff}$ with 10 subsequent measurements each, which are clearly distinguishable; reference measurements (air) after five measurements. Operator-influenced repeatability is 1.36% (1σ).

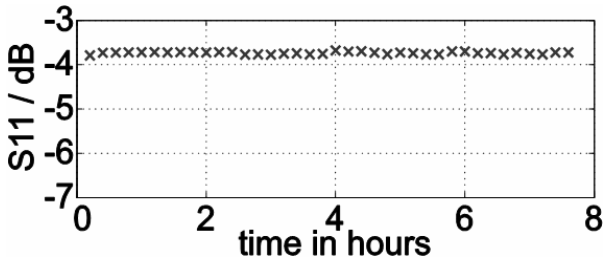

Fig. 6. Long-term stability: reference measurements against air performed between the measurements show a repeatability with a standard deviation of the power of 0.59% (1σ) over 8 hours.

To evaluate the resolution of the probe measurements on a test sample with locally altered permittivity were performed with the prototype with a tip size of 300 µm × 600 µm. The used test sample with a relative permittivity of $\varepsilon_{r,}e_{ff}$= 4.9 has lines of higher permittivity ($\varepsilon_{r,}e_{f\ f}$= 6.6) of varying width ranging from 100 µm to 600 µm.

Additionally, the sample comprises dedicated reference calibration points with a permittivity of $\varepsilon_{r,}e_{ff}$ = 4.9 and $\varepsilon_{r,}e_{ff}$ = 6.6. The sample was scanned in 100 µm steps along two paths in x and y orientation, as shown in Fig. 7(a). Reference measurements against air were taken after every ten measurement points.

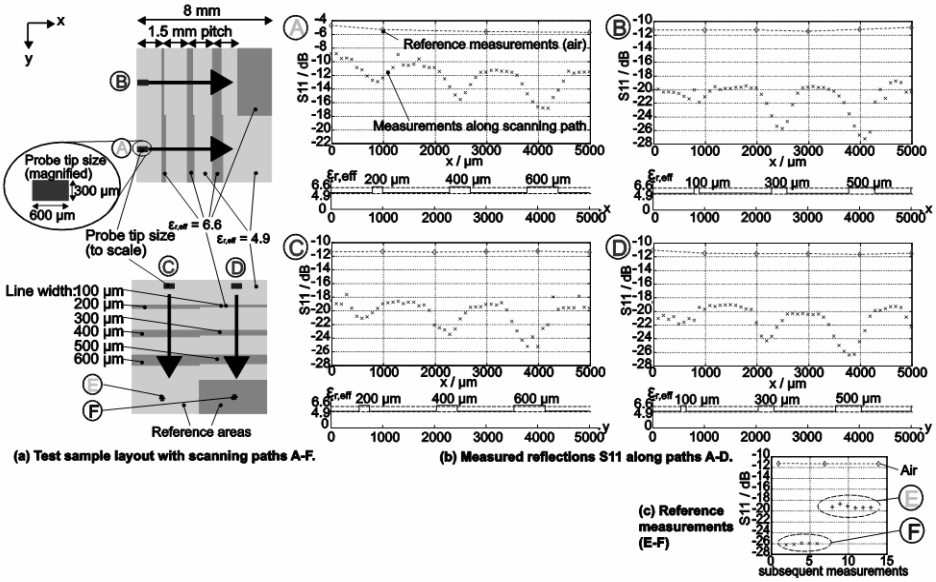

Fig. 7. 2D near-field scanning on micromachined test-samples (at 103.2 GHz): (a) micromachined test samples with locally modulated effective permittivity εr,eff ;different line widths for investigating x-y scanning resolution; (b) measured signal along the scanning paths A-D in 100 µm steps, with plot of sample permittivity εr,eff modulation along the scanning path; (c) reference measurements at sample calibration points.

The measured reflections S11 along the scanned paths (A)-(D) are shown in Fig. 7(b). Figure 7(c) shows the reflection S11 measured on the reference areas (E, F), which corresponds well to the reflection levels on the scanning path. The different reflection levels for the measurement along path (A) result from a different calibration.

The scanning measurements show that the high-permittivity lines of a width of 200 μm can clearly be identified by the probe in both x and y direction, whereas the 100 μm lines are barely resolved. This means that the micromachined tapered-tip probe has a 2-dimensional scanning resolution at least as small as 1/6 of the medium-normalized wavelength.

5. Conclusion

This paper reports on the sensitivity, repeatability and 2-dimensional scanning resolution of a micromachined millimeter-wave near-field dielectric-rod waveguide probe designed for skin cancer diagnosis. Measurements on test samples of different permittivity prove the potential of the probe to discriminate cancerous skin tissue. The repeatability and long term stability of the measurement setup was proven. Two-dimensional scanning measurements were performed on sample with lines of altered permittivity. A probe with a tip size of 300 × 600 μm^2 operating at 100 GHz was found to resolve lines of 200 μm width in both x and y direction. The presented micromachined millimeter-wave near-field probe combines high resolution and high sensitivity, which is important for the diagnosis of small, early-stage skin tumors.

Acknowledgements. This work is supported by The Swedish Governmental Agency for Innovation Systems (VINNOVA) through the Future Health Care Programme. Furthermore, we would like to acknowledge the help by Jan Åberg, MicroComp Nordic, providing the WR-10 waveguides for the measurement setup.

References

[1] K. NOURI, Skin cancer. New York: McGraw-Hill Medical, 2008.

[2] N. HOWLADER, *et al.*, *SEER Cancer Statistics Review, 1975-2008*, National Cancer Institute. Bethesda, MD, 2011.

[3] V. STUNTZEFF, C. CARRUTHERS, *The water content in the epidermis of mice undergoing carcinogenesis by methylocholanthrene*, Cancer Res. **6**, pp. 574–577, 1946.

[4] J.L. SCHEPPS AND K.R. FOSTER, *The UHF and microwave dielectric properties of normal and tumour tissues: variation in dielectric properties with tissue water content*, Phys. Med. Biol. **25**(6), pp. 1149–1159, November, 1980.

[5] V.P. WALLACE, A.J. FITZGERALD, E. PICKWELL, R.J. PYE, P.F. TADAY, N. FLANAGAN and T. HA, *Terahertz Pulsed Spectroscopy of Human Basal Cell Carcinoma*, Appl. Spectrosc. **60**(10), pp. 1127–1133, October, 2006.

[6] P. MEHTA, K. CHAND, D. NARAYANSWAMY, D.G. BEETNER, R. ZOUGHI and W.V. STOECKER, *Microwave Reflectometry as a Novel Diagnostic Tool for Detection of Skin Cancers*, IEEE Trans. Instrum. Meas. **55**(4), pp. 1309–1316, August, 2006.

[7] F. TÖPFER, S. DUDOROV, J. OBERHAMMER; *Micromachined 100GHz near-field measurement probe for high-resolution microwave skin-cancer diagnosis*, Microwave Symposium Digest (MTT), IEEE MTT-S International, pp. 1–3, 17-22 June, 2012.

[8] E. PICKWELL, A.J. FITZGERALD, B.E. COLE, P.F. TADAY, R.J. PYE, T. HA, M. PEPPER and V.P. WALLACE, *Simulating the response of terahertz radiation to basal cell carcinoma using ex vivo spectroscopy measurements*, J. Biomed. Opt. **10**(6), p. 064021, 2005.

Design and Multiphysics Analysis of Low-Loss 60-GHz SPNT RF-MEMS Switches

M.W. ROUSSTIA and M.H.A.J. HERBEN

Eindhoven University of Technology, Department of Electrical Engineering,
Electromagnetics Group, P.O. Box 513, 5600 MB, Eindhoven, The Netherlands
Tel: +31 (0)40 247 5287

Abstract. A design of a capacitive-shunt RF-MEMS switch for 60-GHz ISM-band application is proposed and analyzed. A 0/1-level RF-MEMS packaging technique is used here where via technologies are needed to pass the RF signal through the sealed package. The analysis and characterization of the RF-MEMS switch system include the solder bumps and vias in addition to the switch and the substrate losses in the 60-GHz frequency band. In this condition, a SP9T switch system still exhibits low insertion loss, *i.e.* around 1.5 dB. The isolation for the 60-GHz ISM band (*i.e.* 57–66 GHz) is better than 25 dB. Further, the impedance bandwidth is larger than 20 GHz which means that the switch can also be used for V-band applications. This proposed RF-MEMS switch system is suitable for various applications, such as antenna sectoring, signal routing, and phase shifting. This switch can also be improved to realize a NPNT RF-MEMS switch.

1. Introduction

RF *MicroElectroMechanical Systems* (MEMS) switch increases its popularity since last two decades [1]. It is because of its higher performance than p-i-n diode and field-effect transistor (FET) switches [2]. In this paper, a high performance SPNT switch based on the capacitive-shunt RF-MEMS is designed and analyzed.

In the application of switched-beam antenna, the uniform performance for different output ports of the RF-MEMS switch ensures the uniform performance for different scan direction of the antenna array. Moreover, the advantages of utilizing this switch system for realizing the mentioned application are its less complexity, less losses in the switching section (*e.g.* compared to Butler matrix network in [3]), and no scan blindness (*e.g.* compared to phased-array approach). Further, the proposed RF-MEMS switch system is also suitable for realizing various functions, a.o. signal routing and phase shifting.

2. RF Analysis and Design of the Spnt RF-MEMS

A. RF Analysis

Basically, the RF-MEMS switch has two different types, namely the ohmic-series switch and the capacitive-shunt switch. The capacitive-shunt switch is suitable for millimeter-wave applications because its capacitance is low in the up state (*e.g*. 10–50 fF). Unlike the ohmic-series switch, no induction and resistance in the up-state beam position may exist owing to no contact metal needed. A low reflection coefficient can be obtained because of the low capacitance as expressed in [2]:

$$\left|S_{11}\right|^2 = \frac{\omega^2 C_u^2 Z_0^2}{4} \tag{1}$$

where C_u is the up-state capacitance, Z_o the characteristic impedance, and the angular frequency. Especially at millimeter-wave frequencies, C_u should be designed to have a low or close to zero value to minimize the reflection coefficient. The equivalent circuit of this switch is depicted in Fig. 1.

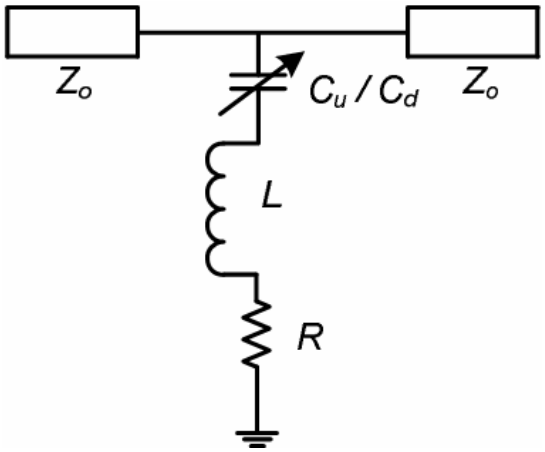

Fig. 1. Circuit model of the capacitive-shunt switch.

The low up-state capacitance can be conveniently achieved by creating a small dimension of the beam, *i.e*. by trading off the surface area or the electrostatic force for a low up-state capacitance. However, the electrostatic force can still be improved by means of the higher actuation voltage and/or lower height of the beam (h_b).

The capacitance in the down-state position (C_d) is higher (*e.g*. hundreds of fF) but does not influence much the isolation except for the inductance. This inductance has to be sufficiently low to achieve a high isolation at millimeter-wave frequencies. This isolation is expressed in

$$|S_{21}|^2 \cong \begin{cases} \dfrac{4}{\omega^2 C_d^2 Z_0^2}, & \text{for } f << f_0 \\ \dfrac{4R_s^2}{Z_0^2}, & \text{for } f = f_0 \\ \dfrac{4\omega^2 L^2}{Z_0^2}, & \text{for } f >> f_0 \end{cases} \tag{2}$$

where $f_0 = 1/(2\pi\sqrt{LC_d})$. Further, L is the inductance, and R_s is the series resistance. It can be clearly observed that at the resonant frequency (f_o) the isolation is independent of the down-state capacitance and is limited by the series resistance of the beam material. This series resistance has to be low enough to give a high isolation at the resonant frequency. Clearly from (2), the resonant frequency of the capacitive-shunt MEMS switch is determined by the LC product.

A t_{sn} thin silicon nitride (Si_3N_4) is deposited on the conductor strip to prevent the short contact between two electrodes. Consequently, the capacitance of the MEMS capacitor will be different for the up and down states dependent on the relative permittivity and the thickness of the dielectric material. Si_3N_4 has relative permittivity (ε_r) of 7.6 and loss tangent (δ) of 0.003. The thickness of Si_3N_4 is 0.15 μm which is sufficient enough to produce very high capacitance to give a high isolation for frequencies lower than the resonant frequency.

Finally, the MEMS component behaves like a RLC circuit with negligible R and L. Thereby, the up-state capacitance, C_u, is given in [4]:

$$C_u = 1.4\frac{\varepsilon_0 A}{h_b + t_{sn}/\varepsilon_r} \tag{3}$$

where C_u is assumed to be 40% larger than the parallel plate value due to fringing fields. A is the area of the electrode under the beam. From RF perspective, it is the area of the signal strip under the beam. Furthermore, the down-state capacitance, C_d, is given by:

$$C_d = R_A \frac{\varepsilon_0 \varepsilon_r A}{t_{sn}} \tag{4}$$

where C_d is assumed as for the parallel plate value and there is no influence due to surface roughness (6/) of the dielectric. In reality, the dielectric surface is not flat. In this case, 6/ can be defined as e.g. 0.65.

B. SPNT RF-MEMS Design

The 0/1-level packaging technique is employed to provide full-solution of the

RF-MEMS design (see Fig. 2(a)). 0-level Liquid Crystal Polymer (LCP) is implemented, while 1-level Sapphire (Al_2O_3) is utilized for the laminate of the MEMS. LCP has relative permittivity (ε_r) of 3.16 and loss tangent (δ) of 0.002. Sapphire has relative permittivity (ε_r) of 9.4 and loss tangent (δ) of 0.000158. The diameter of the solder ball is 60 μm whereas the through-Sapphire-*via* has the diameter of 36 μm.

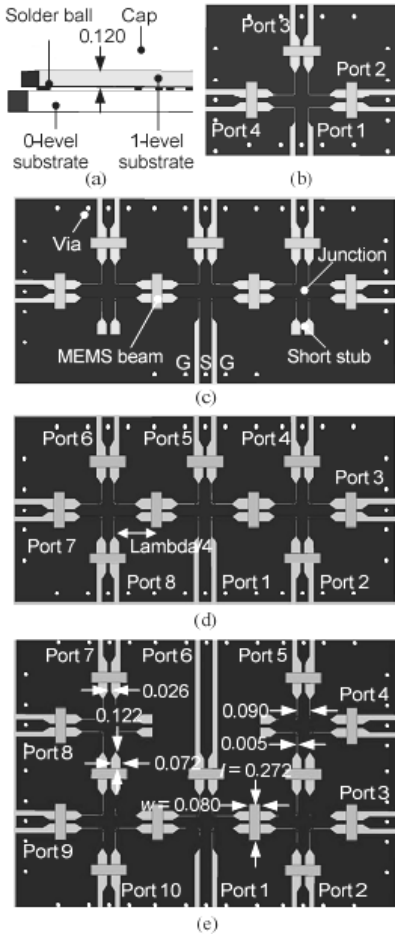

Fig. 2. Structure of the RF-MEMS capacitive-shunt switch: (a) 0/1-level RF-MEMS packaging, (b) SP3T or basic switch element, (c) SP5T, (d) SP7T, and (e) SP9T on the CPW transmission line. All dimensions are in mm. f_0 = 61 GHz.

In Fig. 2(b), the structure of the SP3T RF-MEMS is shown. It can easily be developed further into SPNT or NPNT RF-MEMS switch. The quarter-wave transformer is extensively used for realizing a good matching.

3. Electromechanical analysis of the RF-MEMS

The fixed-fixed membrane in this switch type is modeled as a mechanical spring, with an equivalent spring constant (k). This k is given by [5]:

$$k = 32Ew\left(\frac{t}{l}\right)^3 \left(\frac{27}{49}\right) + 8\sigma(1-\nu)w\frac{t}{l}\left(\frac{3}{5}\right), (\mathrm{N/m}) \tag{5}$$

where E is the Young's modulus, σ the residual stress, and v the Poisson ratio of the beam material. l and w are the dimensions of the beam as depicted in Fig. 2. t is the thickness of the beam. The effective mass of the beam is [4]: $m = 0.4\,plwt$ is the mass density of the beam material. Because the beam is fixed at both ends, the mass of the beam is reduced by 60%.

To collapse the switch to the down-state position, the pull-down voltage (V_h) is given by [4]:

$$V_p = \sqrt{\frac{8kh_b^3}{27\varepsilon_0 A}} \tag{6}$$

where h_b is the initial height of the beam. Moreover, the bias voltage necessary to hold down the voltage (V_h) is given by:

$$V_h = \sqrt{\frac{2k(h_b - t_{sn})t_{sn}^2}{\varepsilon_0 A}} \tag{7}$$

Therefore, the switching time (t_s) is defined as [5]:

$$t_s = 3.67\frac{V_p}{V_s\sqrt{k/m}} \tag{8}$$

where V_s is the drive voltage and $\sqrt{k/m}$ is actually the resonant frequency of the beam.

In this design, the 1.5 μm-thick MEMS beam is made of aluminum, and the copper metal traces are used to realize the CPW transmission line. The summary of the material parameters for electromechanical analysis is shown in Table 1.

Table 1. Material parameters for electrostatic and mechanic problems

Materials	Young's modulus, *E* (GPa)	Poisson's ratio, *v*	Material density, *ρ* (kg/m^3)	Thermal conductivity (W/K/m)	Thermal expansion coefficient (1e-6/K)	Electric conductivity (S/m)
Aluminum	69	0.33	2700	237	23	3.56e7
Copper	117	0.34	9000	401	17	5.8e7
Sapphire	345	0.28	4000	35	5.8	-
Si_3N_4	2.8	0.27	3300	23	3.3	-

4. Simulation Results

A. High-Frequency Analysis

The 3D electromagnetic simulator CST Microwave Studio (MWS) is used to perform the full-wave analysis of the switch structure. In Fig. 3, the S-parameters of SP9T switch are illustrated. The signal path is switched to port 4 in this result. The obtained insertion loss (S41) has included the loss contribution from the solder bumps and vias in addition to the switch and the substrate loss at 61 GHz. Every solder bump contributes 0.114 dB loss whereas every via contributes 0.07 dB loss. Each RF-MEMS itself only contributes 0.06 dB loss. The subtrates (LCP and Sapphire) contribute 0.95 dB loss for the taken path as illustrated in the surface current animation in Fig. 4.

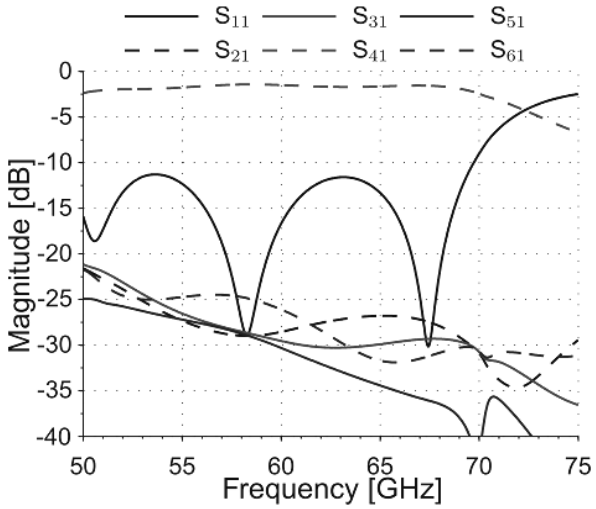

Fig. 3. S-parameters of SP9T RF-MEMS for the signal path switched to port 4.

The obtained isolation for most of the inactive ports is better than 25 dB. Both obtained insertion loss and isolation promise improvements from the design in [6]. The 10 dB-impedance bandwidth covers almost the whole V-band frequencies in this SP9T. Multiple dips in the S_{11} trace are caused by coupled resonant circuits consisting of three basic switch elements.

As mentioned earlier, Fig. 4 illustrates the surface current. Air bridges are applied around the junction to obtain an equipotential between surrounding ground strips. The grounding vias have to be carefully positioned around the signal via to ensure a proper matching.

In Fig. 5, the S-parameters of the SP9T RF-MEMS switch for different switched signal paths are illustrated.It can be observed that the uniform performance is retained for different cases. The insertion loss for all the cases is

approximately less than 2 dB from 57-66 GHz ISM band. The identical group delay is obtained with variation less than 5 ps for the frequency band.

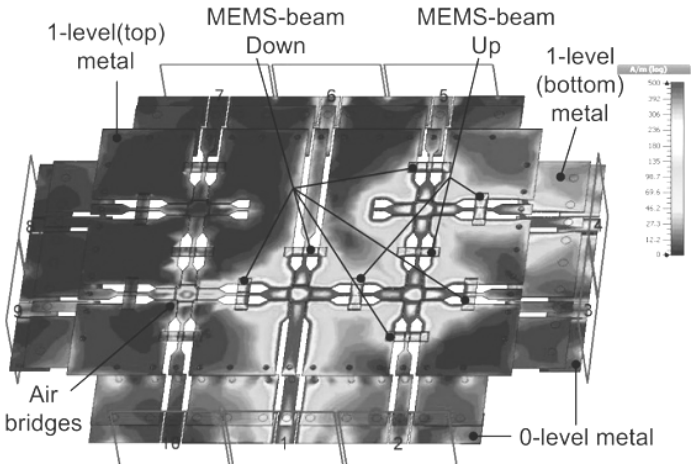

Fig. 4. Surface current of SP9T RF-MEMS at 61 GHz for the signal path switched to port 4 (see also Fig. 2(e)).

The identical performances for each switched path allow the realization of the switched-beam antenna, *e.g.* for radar and commercial applications at 60 GHz. Moreover, similar performances are also observed in SP3T, SP5T, and SP7T RF-MEMS switches.

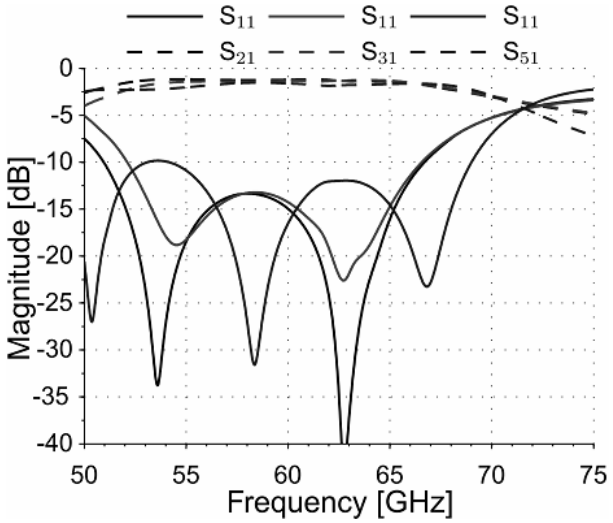

Fig. 5. S-parameters of SP9T RF-MEMS for the signal path switched to port 2 (black), port 3 (red), and port 5 (blue).

A minor difference in S_{11} results (*i.e.* larger dips for the black trace) between signal paths switched to port 2 and port 3 results from the non-uniformity of the junction performance between the straight and perpendicular path.

B. Electrostatic and Mechanical Analyses

In this section, the electrostatic and mechanic problems of this RF MEMS design are investigated using CST MPhysics Studio. To analyze these problems, the material properties from Table I are incorporated.

The DC voltage (V_{dc}) has to be defined which will actuate the aluminum beam through actuation pads right under that beam as shown in Fig. 6. The zero displacement area is the area nearby the beam holder where no beam's deformation exists.

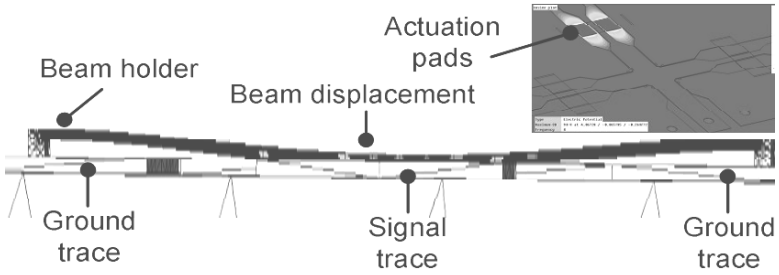

Fig. 6. Mechanical and electrostatic simulation of the MEM beam.

The actuation pads are connected to a simple biasing network in the bottom part of the 1-level substrate. From (8), 90 V_{dc} results in 7.6-μN electrostatic force and thus 5.4-μs fast switching time. The residual stress, C, is approximated as zero when the aluminum beam is etched on the ground substrate. This zero approximation is possible since the beam structure always returns to the initial position (when it is not actuated) owing to the fixed position of the etched beam holder. This switching time is an acceptable value for a MEMS switch [2]. The resulting beam displacement of 2.82 μm suffices to create a contact between two electrodes since the initial height of the beam is 2 μm.

From the analysis, it follows that the capacitance ratio (C_d/C_u) is approximately 32 which is an acceptable value ($20<C_d/C_u<100$) for a design of the MEMS switch [2].

5. Fabrication

Fabrication processes start with the deposition of the metal layers, *i.e.* copper and/or gold, on the Sapphire wafer using evaporation method. The layers are patterned using the mask and etched to create the CPW lines. The Plasma-Enhanced Chemical Vapour Deposition (PECVD) can be used to deposit the Si_3N_4 on the metal layer [7]. The sacrificial layer is employed here where the aluminum

will be deposited on to form the MEMS beam. The XLIM lab in [8] and DIMES lab at TU Delft can accommodate the fabrication processes.

6. Conclusion

The high-performance SPNT RF-MEMS switch based on the capacitive-shunt switch has been designed. The analysis of the switch system which includes the solder bumps, vias, and RF-MEMS switches in addition to the substrate losses in the 60-GHz frequency band still results in low insertion loss, *i.e*. around 1.5 dB for SP9T. The isolation is better than 25 dB, and this SPNT switch exhibits a wideband performance. Uniform performances are observed for different switched signal paths. The proposed RF-MEMS switch is suitable for applications, such as antenna sectoring/switching, signal routing, and phase shifting.

References

[1] G.M. REBEIZ, C.D. PATEL, S.K. HAN, C.-H. KO and K.M.J. HO, *The search for a reliable MEMS switch?*, IEEE Microwave Magazine **14**(1), pp. 57–67, Jan./Feb., 2013.

[2] G.M. REBEIZ and J.B. MULDAVIN, *RF MEMS switches and switch circuits*, IEEE Microwave Magazine **2**(4), pp. 59–71, Dec. 2001.

[3] C.-H. TSENG, C.-J. CHEN and T.-H. CHU, *A low-cost 60-GHz switched-beam patch antenna array with Butler matrix network*, IEEE Antennas and Wireless Propagation Letters **7**, pp. 432–435, 2008.

[4] G.M. REBEIZ, *RF MEMS Theory, Design, and Technology. Hoboken*, NJ: Wiley, 2003.

[5] K. van CAEKENBERGHE, *RF MEMS on the radar*, IEEE Microwave Magazine **10**(6), pp. 99–116, Oct. 2009.

[6] S. GONG, H. SHEN and N.S. BARKER, *A 60-GHz 2-bit switched-line phase shifter using SP4T RF-MEMS switches*, IEEE Transactions on Microwave Theory and Techniques **59**(4), pp. 894–900, April 2011.

[7] A. SINJARI and S. CHOWDHURY, *High performance 77 GHz single pole triple throw (SP3T) MEMS switch*, Joint IEEE Nort-East Workshop on Circuits and Systems and TAISA Conference (NEWCAS-TAISA), 28 June-1 July, Toulouse, France, 2009.

[8] B. BÉLENGER, B. ESPANA, S. COURRÈGES, P. BLONDY, O. VENDIER, D. LANGREZ and J.-L. CAZAUX, *A high-power Ka-band RF-MEMS 2-bit phase shifter on Sapphire substrate*, Proceedings of the 6th European Microwave Integrated Circuits Conference, 10-11 October, Manchester, UK, 2011.

3D Micromachined Ka (30 GHz) Band RF MEMS Filter for On-Board Satellite Communication Systems

Abdul Qader Ahsan QURESHI[1], Luca PELLICCIA[2], Sabrina COLPO[1], Flavio GIACOMOZZI[1], Paola FARINELLI[2], Benno MARGESIN[1]

[1]Fondazione Bruno Kessler (FBK), MEMS Group, Via Sommarive 18, Trento (38123), Italy
Tel.: 39-0461-314490
[2]University of Perugia, Department of Electronic & Information Engineering, Italy

Abstract. This paper describes the development of Ka band microwave filters on silicon substrates based on micromachining techniques and multiple wafer stacking. On this concept a 4th order pseudo elliptic Ka band filter based on TEM mode resonators was designed from which test structures have been derived to allow at the same time the technology development on simpler structures and to test the key element of the filter, *i.e*. the resonator.

Measured results show a quality factor of the single resonator of 500 and frequency shifts as good as 0,1%. Compact size filters with excellent RF performance seem to be within the reach of this technology.

1. Introduction

Numbers of fabrication techniques and materials have been proposed for the realization of low loss, high Q-factor micromachined filters over the last years. The most common topology by which Ka band filters are realized is the resonant cavity. Resonators made by low-loss micromachined cavities are relatively easy to integrate with monolithic circuits, smaller in size and weight, and provide high Q-factor (*i.e*. > 3500). On the other hand Ka band filters have also been realized in microstriplines [1], dielectric membranes [2], coaxial transmission lines or waveguides [3, 4] which are only some of the alternative approaches by using micromachining techniques [5, 6] for obtaining high Q-factor. In the millimetre and sub millimetre wave range planar technology can be adopted to reduce weight and size, as well as to make the integration with monolithic circuits easier.

Despite their advantages, conventional planar solutions show relatively high

losses (*i.e*. low Q-factor) with respect to 3D structures (*e.g*. waveguide filters), mainly due to the losses in the substrate. Micromachining techniques can allow for realizing innovative structures presenting a good trade-off in terms of resonators Q-factor, size and integrability with monolithic or printed circuits. This paper briefly introduces the design of a 4th order Ka band filter based on TEM mode resonators and focuses on the design and development of the fabrication process of the test structures derived from the filter design in order to test the technology and to test the basic element (*i.e*. resonator) of the filter.

2. Filter Design

The choice of suitable filtering functions and the corresponding filter topologies, as well as the identification of the needed quality factor and physical realization of the resonators, are the key aspects of microwave filter design especially in case of bandpass filters. A common issue in filter design is the reduction of the passband insertion loss; the insertion loss of a bandpass filter largely depends on the insertion loss of the single resonator (unloaded Q-factor of the resonators), and it is directly related to the physical realization of the resonator. In addition, the passband insertion loss is inversely related to the filter bandwidth and directly related to the filter order. Therefore, for a prescribed bandwidth, filters employing a minimum number of resonators are to be preferred. Another advantage of using a minimum number of resonators is that the sensitivity with respect to manufacturing tolerances is reduced. On the contrary, the higher the filter order, the higher the sensitivity and the higher the required manufacturing accuracy.

Thus, for better selectivity in filter design advanced filtering functions, such as elliptic or quasi-elliptic functions [7], that exploit finite frequency transmission zeros, are essential to satisfy the filter requirements with a minimum number of resonators.

A 4th order pseudo elliptic Ka band filter based on TEM mode resonators is presented in Fig. 1. While the expected performance of the 4th order pseudo-elliptic filter realized by stacking four 500μm thick Si wafers is depicted in Fig. 2(a, b). The simulated λ/2 TEM mode Q-factor is 750.

3. Test Structures

Even the simulated properties of the filter presented in Fig. 1 matches with desired specifications it was decided to make a technology development run before trying to fabricate this complex structure. This approach on one hand allow to verify the process architecture but on the other hand allow to evaluate the assembly and fabrication tolerances.

Therefore, to keep the effort and complexity as low as possible some simple but significative test structures shown in Fig. 3(a, b, c, d) were designed.

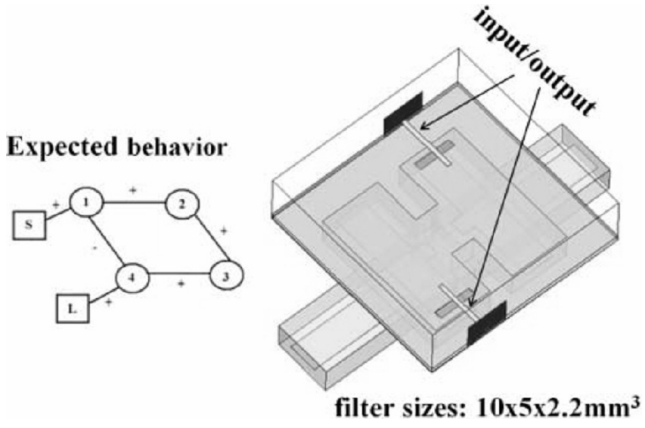

Fig. 1. HFSS model of a 4th order filter.

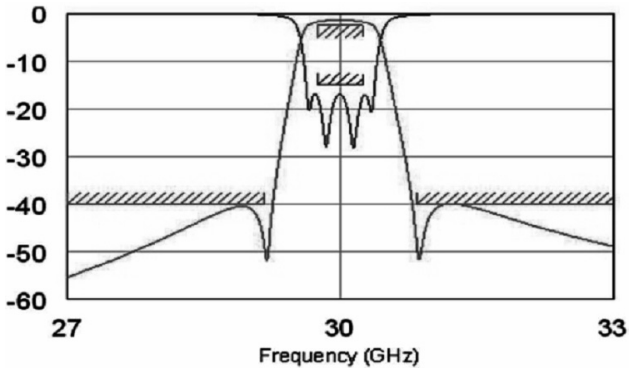

a)

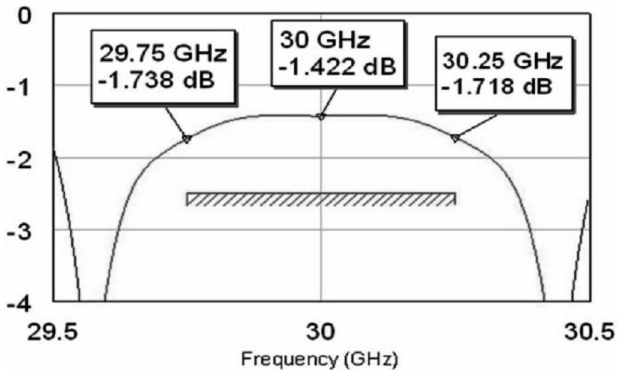

b)

Fig. 2. Performance of the 4th order filter: (a) S-parameters (dB) and (b) in-band S_{21} (dB).

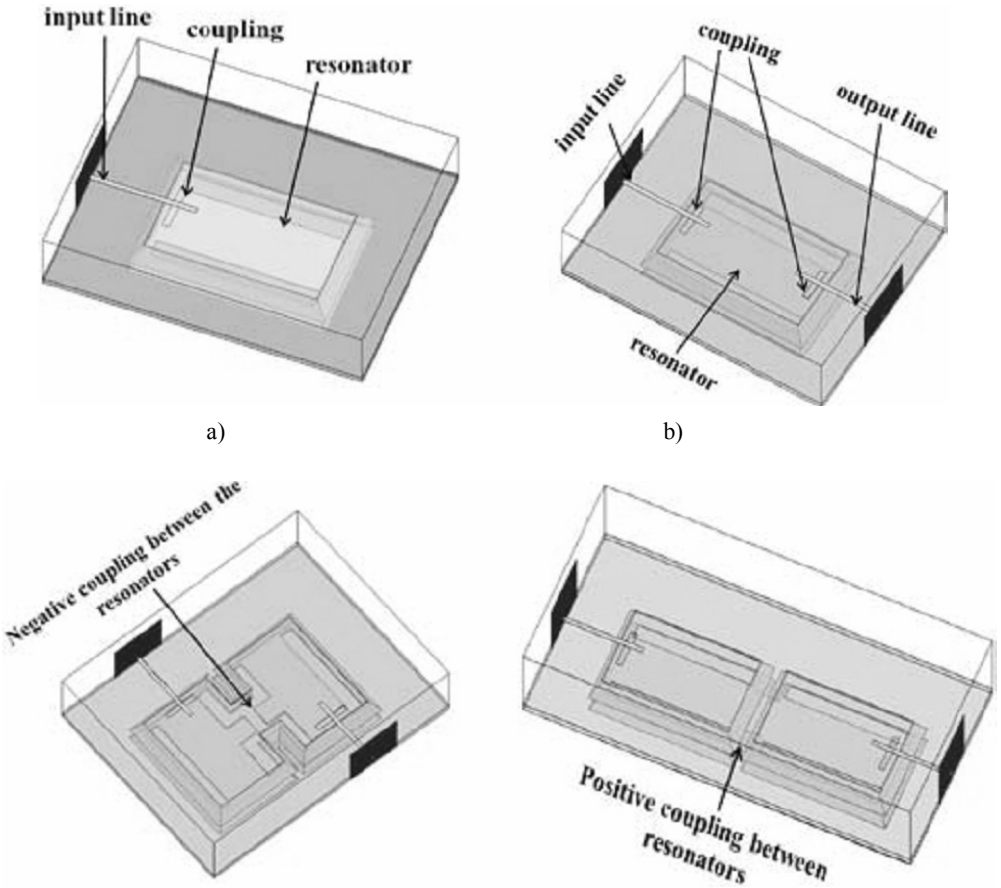

Fig. 3. Layout of test structures: (a) 1-port resonator, (b) 2-port resonator (c) 2nd order filter (A-type) and (d) 2nd order filter (B-type).

4. Fabrication Process

Figure 4 presents a schematic cross section view of the test structures. The technological concept for the 4th order Ka band filter requires a top layer and four different intermediate layers, but two in the reduced test version, with an individual mask set for each. Only the sealing ring mask is common for all.

For the fabrication of the layers two process flows namely Process A and B were developed. "Process A" consists in a 5 mask sequence and deals with the construction of the top and bottom layers of the structure. In this process a 200 μm thick, HR 5000 Ωcm, p -type, <100>, double side polished four-inch silicon wafers are used as starting material. The whole process flow consists in a set of 115

sequential process steps. "Process B" is again a 5 mask fabrication process, employed for the construction of the middle layers of the structure. For creating deep cavities 500 μm thick, HR 5000 Ωcm, <100>, p-type, double side polished silicon wafers are used as substrate. The complete process is composed of 94 individual processing steps.

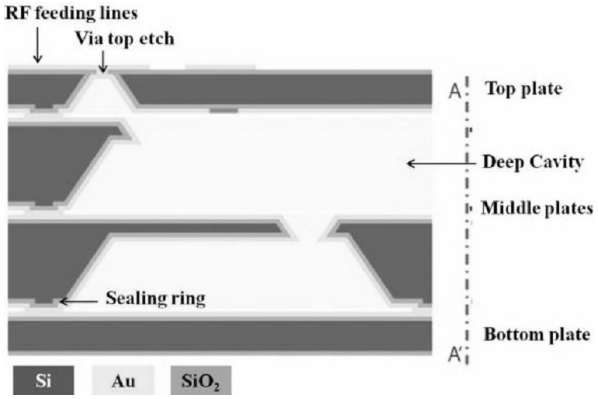

Fig. 4. Simplified cross section view of the structures shown in Fig. 3. Only one half of the structure is shown considering A-A' symmetry plane.

A. Fabrication Process Flow of Top Layer (Process A)

The ''Process A'' fabrication process started with the first lithography step for the definition of the sealing ring on the backside of the wafer. At this point photoresist was spun on the wafer, exposed and developed. The pattern was then transferred to the silicon by a plasma etching with a Deep Reactive Ion Etching (DRIE) technique and a sealing ring with a nominal step height of 2 μm was formed as shown in Fig. 5(a).

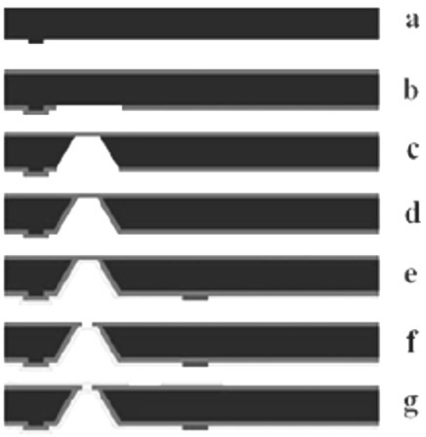

Fig. 5. Process flow for the top layer of the Ka band filter.

After that 1 μm thick thermal oxide was grown at 975°C. Then a 150 nm thick silicon nitride film was deposited by Low Pressure Chemical Vapor Deposition (LPCVD) at 775°C, followed by a LPCVD medium temperature oxide deposition from Tetraethyl orthosilicate (TEOS) at 718°C. This multilayer structure is a so-called hard mask layer and was deposited on both sides of the wafer.

Second lithography defines the via openings on the wafer backside. The mask for the bottom via's was printed and dry etched to form a etch window in the dielectric layer, see Fig. 5(b). As a subsequent step via's opened in the 2nd lithography step were etched in a 25% (TMAH):water solution in two steps. First etching produces a 175 μm deep cavity. In a second step the cavity is deepened to full wafer thickness with a little over etch to exposes the bottom of the front hard mask layer, see Fig. 5(c).

Next, the front side of the wafer was covered by photoresist and the TEOS layer was selectively removed from the backside of the wafer with the help of buffered hydrofluoric acid (HF). After ashing the photoresist the nitride layer was stripped from the backside of the wafer with phosphoric acid (H_3PO4) at 150°C for 30 min. Then the wafers were oxidized again for 385 minute in steam at 975°C in order to grow a 1 μm thick oxide layer on the sidewalls of the Through Silicon Vias (TSVs). After that the wafers were annealed in nitrogen at 975°C for 1 hour.

This completes the isolation of the silicon substrate, see Fig. 5(d). In the subsequent steps the hardmask was removed and then the backside of the wafer was coated with a conductive seed layer composed of (Cr\Au\Cr, 2.5\25\2 nm) for electroplating.

The third lithography step was done with a negative dry film resist and slots were defined on the bottom gold layer, refer to Fig. 5(e). The RF signals are inserted and extracted from the cavity through these slots. In order to connect electrically the top metalized layer with the bottom gold layer via's are needed. Therefore top via holes were defined by a fourth lithography and oxide dry etching as depicted in Fig. 5(f).

The fabrication of the top layer ends with the depositing a second seed layer, identical to the first one, on top of the wafer. Then standard resist (AZ 1050) was span and the fifth lithography was performed to pattern the feeding lines that carry the RF signals. In the following step a 2.5 μm thick Au plating was performed and the seed layer was removed from the unwanted areas as presented in Fig. 5(g). Finally the wafers were annealed at 190°C for 30 min to sinter the gold layers.

B. Fabrication Process Flow of Middle Layer(Process B)

''Process B'' was used to produce cavities in the middle layers of the structure sketched in Fig. 6.

As a first step a 120 nm thick thermal oxide was grown by steam oxidation of Si at 975°C. First lithography is performed to define the lattice alignment marks

followed by dry etching of the thin oxide layer. After ashing the photoresist layer a short bulk micromachining of silicon (20 μm deep) using a 25% TMAH: water solution is carried out to produce small pyramidal cavities in each circular window opening.

RCA cleaning was performed before the 2nd lithography and then photoresist was deposited, exposed and developed to define the 50 μm wide sealing ring. Alcatel (DRIE) system was used to etch the sealing ring with a nominal step height of 2 μm, see Fig. 6(a).

Subsequently a 120 nm thick thermal oxide is grown with a steam oxidation at 975°C and pre-lithography cleaning was performed. Then with the help of 3rd lithography the etch window for the top cavity on the wafer front side is defined by dry etching the oxide layer as illustrated in Fig. 6(b)

A short bulk silicon etch with a 4:1 TMAH:water solution at 90°C is performed in order to etch a 20 μm deep cavity in the silicon, see Fig. 6(c). At this point as before a multilayer oxide called "hard mask" is used to protect the front and backside of the wafer from the bulk silicon etching (which was employed for the formation of the main cavity), see Fig. 6(d).

The 4th lithography defines the etch window for the main cavity by etching the hard mask layer with plasma etching on the bottom of the wafer as shown in Fig. 6(e). Later the cavities were bulk etched with a 4:1 TMAH:water solution at 90°C in two steps. First step with an etching time of approximately 11 hrs results in a 455 μm deep cavity. In the second step the cavity is deepened in order to meet the smaller cavity etched from the front side as presented in Fig. 6(f).

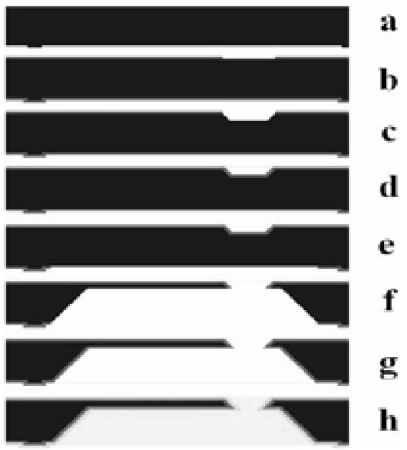

Fig. 6. Process flow for the middle layers of the Ka band filter based on the simplified cross-section of Fig. 4.

Next the dielectric layers are removed with a sequence of three wet etchings: first the residues of the top oxide, followed by the removal of silicon nitride and the

underlying oxide layer, till the bare silicon. After that the wafers are oxidized for 385 minute in steam at 975°C in order to grow a 1 μm thick oxide layer on all silicon surfaces. In order to reduce the trapped oxide charge the wafers are then annealed in nitrogen at 975°C for 1 hour and this completes the isolation of the silicon substrate, refer to Fig. 6(g).

This fabrication process ends with the metallization of both sides of the wafers. For this purpose a seed layer consisting of a 2.5 nm thick chromium layer, followed by a 25 nm thick gold layer is evaporated by Physical Vapor Deposition (PVD) on both front and back side of the wafer. Then electroplating is performed to deposit the 2.5 μm thick gold layer onto the surface of the previously deposited gold seed layer as presented in Fig. 6(h). This provides a continuous coating also around the corners.

Finally the wafers are annealed at 190°C for 30 min in order to sinter the gold layers.

5. Measurements

After assembly the final devices were characterized and tested in order to test both technology and design. The filters were characterized in terms of insertion loss, return loss and group delay in the 20–40 GHz frequency band. The Q-factor was extrapolated from the loss response. This section presents the initial measurements performed on two types of test structures presented in Fig. 3(a, b). In order to estimate the loss contribution of the microstrip line and the coplanar-to-microstrip transition a 3mm microstrip line with two coplanar-to-microstrip (*i.e.* Ka1) interconnection was measured. The measured insertion loss is 0.525 dB at 30 GHz showing a good matching, as shown in Fig. 7.

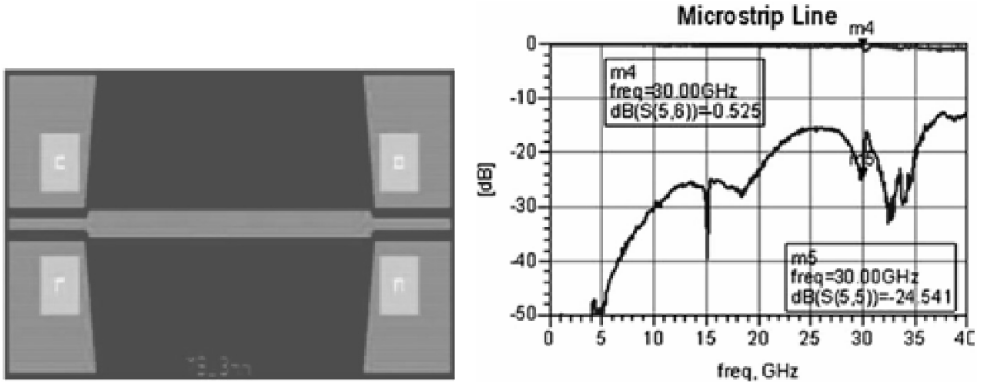

a) b)

Fig. 7. (a) Layout of the 3mm long microstrip line and 1mm long coplanar-to-microstrip via transition. (b) Measured performance, return loss in blue and insertion loss in red.

After evaluating the loss of the coplanar-to-microstrip transition the two-port resonator illustrated in Fig. 3b (*i.e*. Ka2) was measured. The fitted Q factor of the device is about 500 (600 from HFSS simulations, considering:silicon permittivity = 11; silicon tan δ = 0.005; gold conductivity = 4.1×10^7 S/m) and a relative frequency shift of less than 0.1 %. Fig. 8 shows the results of all Ka2 samples, which are plotted in comparison with the simulation. In few samples a frequency shift of 0.7% has been observed which is very likely due to variations in the internal dimensions of the cavities because of the long etching time.

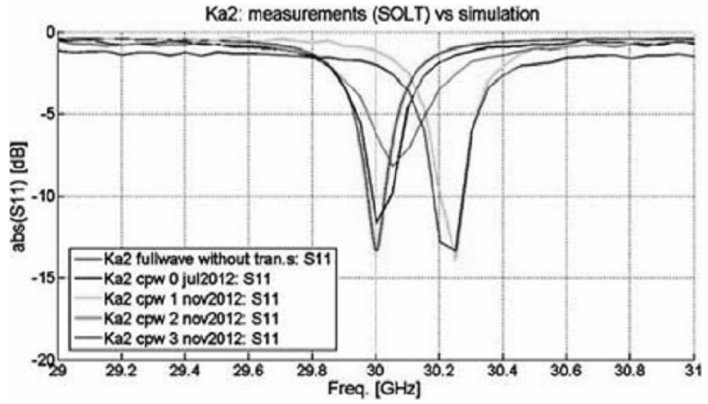

a)

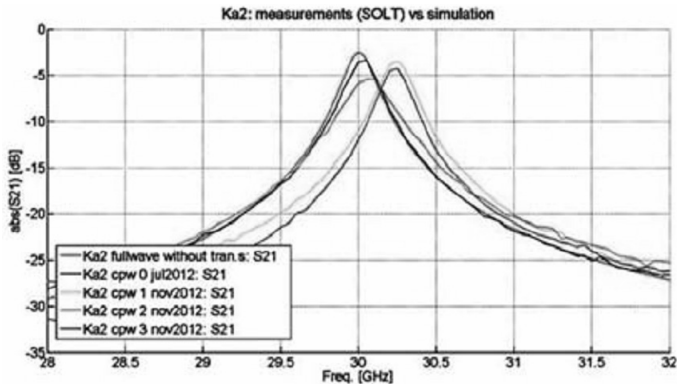

b)

Fig. 8. Ka2 all samples. Comparison between simulation (in red) and measurements. (a) Return Loss, (b) Insertion Loss.

6. Conclusion

Starting from a 4th order pseudo-elliptic filter design a technology concept based on micromachining techniques and multiple wafer stacking was developed. To test both fabrication process and basic filter elements test structures were derived from

the filter design, fabricated and measured. The fabrication requires two process sequences for the two different types of layers that compose the filter. The assembled filter elements showed good performance both in terms of quality factor and frequency matching. Therefore the proposed process seems to suit well the fabrication of the complete four-pole filter. It also shows a good potential in size reduction of the filters and of volume production.

Acknowledgements. This research is funded by European Space Agency. The authors wish to acknowledge their financial support in this work

References

[1] W. ZHAO, Y. ZHANG, Y. GUO, *A novel Ka-band bandpass filter using microstrip closed loop resonators*, Microwave Conference, APMC, Asia Pacific, pp. 1443–1445, 7-10 Dec., 2009.

[2] M. CHATRAS, P. BLONDY, D. CROS, O. VENDIER and J. CAZAUX., *A surface-mountable membrane supported filter*, Microwave and Wireless Components Letters, IEEE, **13**(12), pp. 535–537, Dec., 2003.

[3] J.R. MRUK, D.S. FILIPOVIC, *Micro-coaxial V-/W-band filters and contiguous diplexers*, Microwaves, Antennas & Propagation, IET **6**(10), pp. 1142–1148, 17 July, 2012.

[4] J.R. REID, J.M. OLIVER, K. VANHILLE, D. SHERRER, *Three dimensional metal micromachining: A disruptive technology for millimeter-wave filters*, Silicon Monolithic Integrated Circuits in RF Systems (SiRF), IEEE 12th Topical Meeting, pp. 17–20, 16-18 Jan., 2012.

[5] B. GUILLON, D. CROS, P. PONS, K. GRENIER, T. PARRA, J.L. CAZAUX, J.C. LALAURIE, J. GRAFFEUIL, R. PLANA, *Design and realization of high Q millimeter-wave structures through micromachining techniques*, Microwave Symposium Digest, IEEE MTT-S International **4**, pp. 1519–1522, 1999.

[6] G.M. REBEIZ, *MEMS Theory, Design and Technology, Wiley Intersciences*, John Willy & Sons, 2003.

[7] R.E. Amaya, *A layout efficient, vertically stacked, resonator-coupled bandpass filter in LTCC for 60 GHz SOP transceivers*, IEEE, Radio Frequency Integrated Circuits Symposium (RFIC), pp. 245–248, 23-25 May,2010.

Controllable Essence of Complex Materials Exploiting Two-Hot-Arm Electrothermal Actuators

A.X. LALAS, N.V. KANTARTZIS and T.D. TSIBOUKIS

Department of Electrical and Computer Engineering, Aristotle University of Thessaloniki,
GR-54124, Thessaloniki, Greece
E-mail: tsibukis@auth.gr

Abstract. A complex material with programmable nature, derived from the combination of double two-hot-arm electrothermal actuators with a split-ring resonator (SRR), is introduced in this paper. The proposed design allows transition between conventional and *Mu-NeGative* (MNG) performance, along with bandwidth tunability. Several numerical results, extracted via the *Finite Element Method* (FEM), support its controllable behavior.

1. Introduction

Modern RF technology is mainly based upon artificially engineered complex materials, which exhibit unique electromagnetic properties, not always available in nature. Among them, metamaterials have been involved in numerous interesting designs [1]–[2]. However, their inherent lack of wide spectral bandwidths is deemed prohibitive to real-life implementations. In order to efficiently tackle this limitation, several tuning mechanisms have been proposed, such as magnetically or thermally controlled liquid crystals, and optically reconfigurable silicon apparatus [3]–[5]. Nevertheless, radio-frequency microelectromechanical systems (RF-MEMS) [6] are considered as the most suitable devices to achieve the required bandwidth tunability.

Several electrostatic RF-MEMS components, such as cantilevers, curved membranes and comb drives, have been exploited to accomplish performance controllability in metamaterial designs [7]–[9]. However, the necessary high bias voltages introduce constraints in further utilization of these devices. On the other hand, electrothermally tunable structures [10]–[12] combine low bias voltages with analog control of the material's behavior, due to the lack of snapdown effects. In this context, an interesting implementation of a reconfigurable metamaterial

associates the double two-hot arm electrothermal actuator [13] with a splitring resonator (SRR). This arrangement results in a tunable *Mu-NeGative* (MNG) behavior. Nonetheless, apart from bandwidth enhancement, the capability of altering the essence of a complex material, between *Double-PoSitive* (DPS) and MNG performance, is considered crucial to the development of commercial applications. Furthermore, to the best of our knowledge, an electrothermally controlled transition between different aspects of a complex material has not been yet numerically investigated. Therefore, the goal of this paper is to examine the incorporation of the aforementioned RF-MEMS component into more complicated SRR designs in an effort to achieve the desired essence reconfigurability. The proposed setup successfully exhibits this attribute, as verified by the numerical data acquired by our simulations.

2. Features of the Electrothermal Actuator

The operation of a two-hot-arm electrothermal actuator is based on the asymmetric thermal expansion of the hot and cold arms, when an electric circuit is created by applying a potential difference between them. Specifically, electric current flows along the thinner arms, resulting in resistive heating and thermal expansion, while the thicker arm remains cold. Thus, a deflection occurs due to the expansion difference between hot and cold arms. The geometry and design parameters of the PolySilicon horizontal thermal actuator are shown in Fig. 1. Their values are: $L_1 = 252$ μm, $L_2 = 220$ μm, $L_3 = 1\,62$ μm, $L_4 = 38$ μm, $w_1 = 21$ μm, $w_2 = 14$ μm, $w_3 = 14$ μm, d = 2 μm, and $g = 5$ μm. Also, the height of dimples and anchors is set to 2 μm, while the height of the remaining actuator is 2 μm.

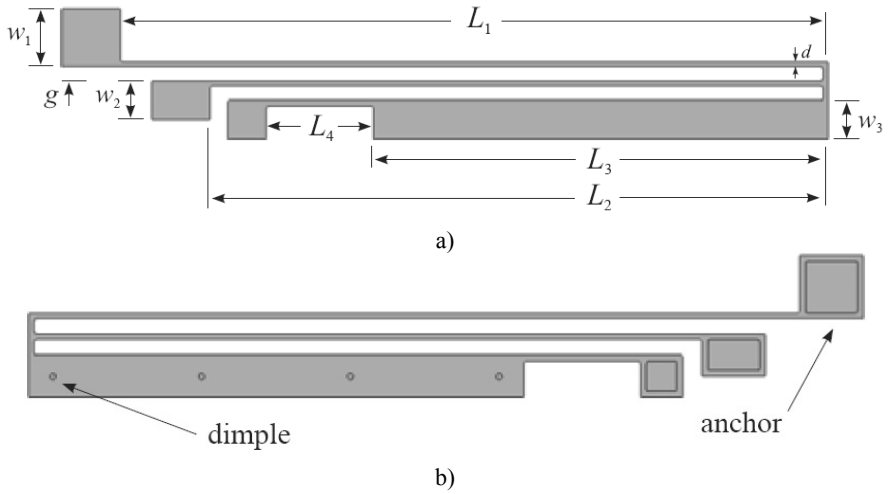

Fig. 1. Geometry and design parameters of the two-hot-arm electrothermal actuator. (a) Front and (b) back side.

A double parallel actuated structure can be designed as depicted in Fig. 2(a). To clarify the basic characteristics of this device, a coupled electric, thermal and structural analysis is conducted. Several media properties of PolySilicon are needed to effectively perform our simulations, as given in Table 1. Moreover, the heat transfer coefficient between air and the upper surface of the actuator is hu = 400 W/(m^{2}K), while this value is modified to h = 20000 W/(m^{2}K) for all remaining boundary surfaces due to their proximity to the substrate. The ambient temperature is considered *Text* = 20°C, which is the reference value for calculating thermal expansion. The analysis is performed via the *Finite Element Method* (FEM), employing 4816 prismatic elements and 141630 degrees of freedom.

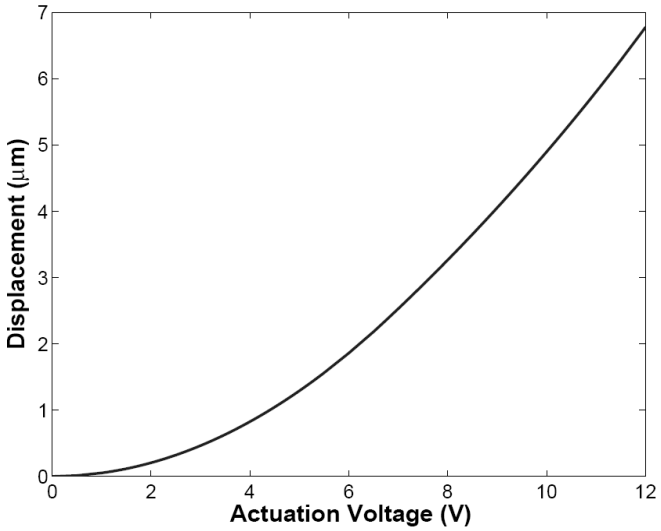

Fig. 2. The double parallel electrothermal actuator. (a) Geometry, (b) total displacement distribution (in μm) at the actuation voltage of 12 V, and (c) maximum tip displacement for different values of the actuation voltage.

Table 1. Electrical, thermal and structural Properties of polysilicon

Properties	Value	Unit
Thermal expansion coefficient α	2.6 x 10^{-6}	1/K
Heat capacity C_p	678	J/(Kg K)
Density ρ	2320	Kg/m^3
Thermal conductivity k	34	W/(m K)
Electrical conductivity σ	5 x 10^4	S/m
Young's modulus E	160 x 10^9	Pa
Poisson's ratio v	0.22	

Under this concept, the deformed geometry of the actuator is depicted in Fig. 2(b), together with its total displacement distribution at the actuation voltage of 12 V. The maximum tip displacement for different values of the actuation voltage is presented in Fig. 2(c). To avoid undesirable short circuits that may degrade the device's performance, the operational range is limited to 12 V.

Hence, a maximum displacement of 6.8 μm is observed. Additionally, the electrical features of the device are derived in terms of the current and total power dissipation as illustrated in Fig. 3. The maximum current intensity is 10 mA, resulting in the maximum power losses of 120.2 mW for an actuation voltage of 12 V.

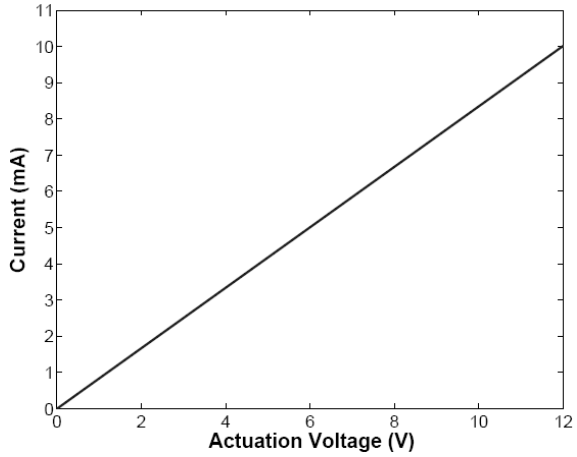

a)

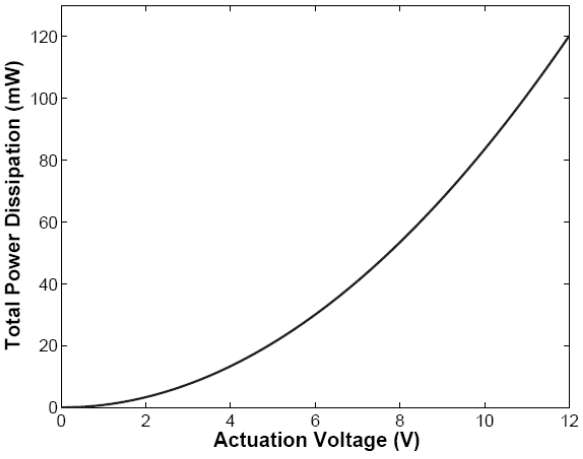

b)

Fig. 3. Electrical characteristics of the double parallel electrothermal actuator: (a) Current and (b) total power dissipation versus actuation voltage.

Furthermore, the thermal characteristics of the actuator are obtained in Fig. 4 via temperature distribution and maximum temperature calculation. It is obvious that the maximum temperature is developed over the middle sections of the outer hot arms exhibiting a value of 1023.8°C. This temperature is near the limit of thermal failure [11] thus, it is considered high and special effort is needed to be reduced into a practical range. Alternatively, a lower voltage could be chosen as a limit for the operation of these devices.

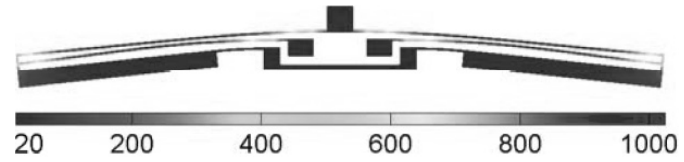

a)

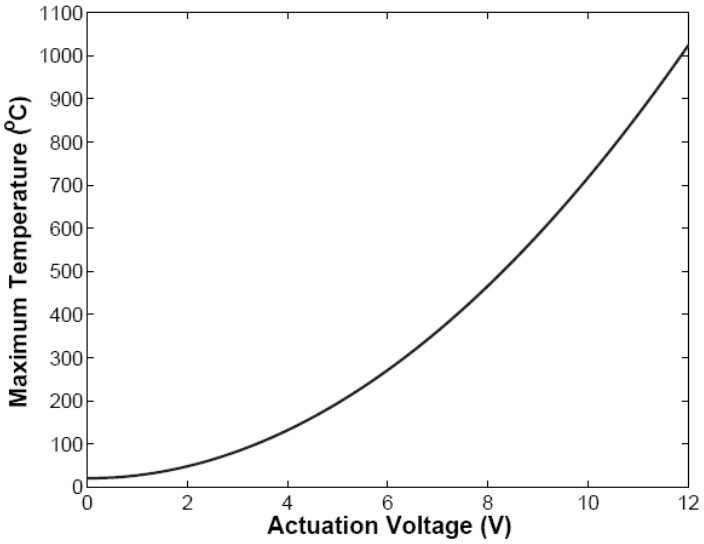

b)

Fig. 4. Thermal characteristics of the double parallel electrothermal actuator. (a) Total temperature distribution (in °C) at the actuation voltage of 12 V and (b) maximum temperature for different values of the actuation voltage.

3. Essence Controllability

A reconfigurable complex medium can be designed by using two double parallel actuated structures. The geometry of the controllable unit cell is shown in Fig. 5. Obviously, two degrees of freedom are eligible in controlling the behavior of this complex material, namely the bias voltage of the upper and lower actuators.

When no voltage is applied to the lower actuator's arms, four distinct gaps are formed, resulting in a conventional DPS material, since no magnetic resonance can be generated.

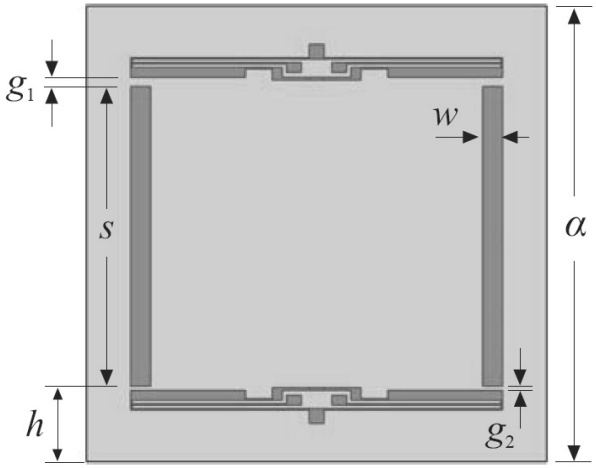

Fig. 5. Geometry and design parameters of the electrothermally controlled in terms of double parallel electrothermal actuators, complex material unit cell.

However, when applying the proper bias voltage, the tips of the lower actuator are in contact with the metal strips and an MNG performance arises. In such a case, the bias voltage of the upper actuator may be employed to deform this structure and shorten the upper gaps. In this manner, variations in voltage levels introduce a tunable gap and thus a reconfigurable SRR. The device's strips are consisted of PolySilicon along with a metal coating on their upper side, such as gold. Moreover, a metal coating is placed over the cold arms of the actuators in order to sustain any resonances. The proposed devices could be fabricated using a surface micromachining technique, such as the Multi-User MEMS Processes (MUMPs) [14]. Nevertheless, in order to successfully control the complex material's behavior a properly designed bias network is indispensable. This network should be carefully designed and optimized, so that it does not modify severely the electromagnetic response of the complex medium. The length and the width of the structure's metal strips are s = 427 μm and w = 28 μm, while their height is 4 μm and h = 108 μm. Moreover, the initial lengths of the upper and lower gaps are set to $g1$ = 13 μm and $g2$ = 6 μm. The cell period is α = 650 μm and the thickness of the Si3N4 substrate is 20 μm. Taking into account these data, all numerical simulations are conducted by means of the FEM. Indicatively, when the actuation voltage of both RF-MEMS components is 12 V, the computational domain is divided into 142895 tetrahedral elements with 909484 degrees of freedom. To extract the *S*-parameters, a parallel-plate waveguide approach is adopted, which requires the use

of perfectly electric and perfectly magnetic conductor boundary conditions instead of the conventional periodic boundary conditions. Also, a robust homogenization method [15] is exploited to retrieve the constitutive effective parameters of the proposed complex materials. In this framework, the magnitude of the *S*21-parameter along with the real part of the effective magnetic permeability are calculated and presented in Fig. 6.

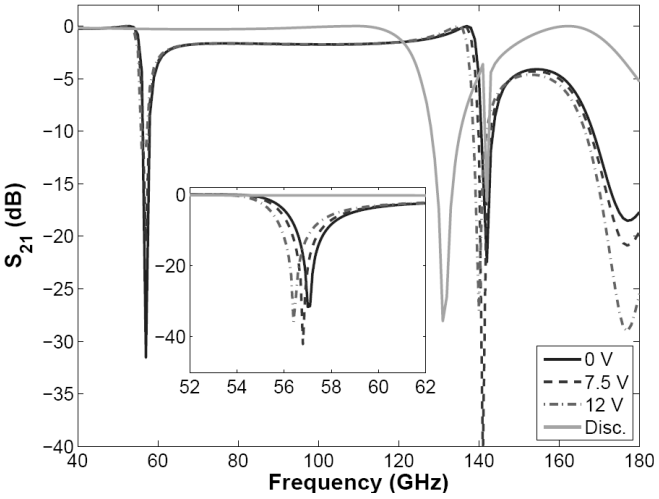

a)

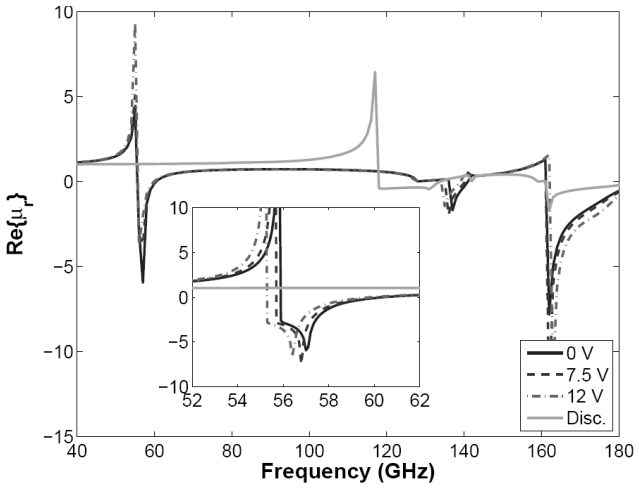

b)

Fig. 6. Tunable behavior at several actuation voltages in terms of (a) S_{21}-parameter and (b) effective magnetic permeability (*Disc*. denotes the state where all tips are disconnected, whereas the inset figures present the performance of the device at the first resonance using a much finer spectral resolution).

Initially, a coarse spectral resolution is adopted to identify the primary resonances and then a fine resolution is utilized to perform accurate bandwidth measurements, as depicted into the inset figures. The analysis is conducted for two discrete cases. In the first arrangement, the tips of all actuators are disconnected from the metal strips, whereas in the others the tips of the lower actuator are only connected. It is evident that in the first state the complex medium exhibits a DPS performance. However, when the lower device is actuated, three distinct negative μ frequency regions appear, but only the first is recognized as a left-handed resonance. This is enforced by the validity condition of the homogenization technique which implies that the operational wavelength must be higher than the cell period by a factor of 8 at least. Therefore, a controllable transition between DPS and MNG behavior is sufficiently proved. Moreover, an enhanced tunability is attained as the actuation voltage of the upper structure in creases from 0 V to 12 V. By inspecting the results of the inset figures of Fig. 6, three frequency regions of interest are denoted, where insertion loss exceeds 20 dB, namely, 56.864–57.253 GHz, 56.63–57.015 GHz, and 56.245–56.632 GHz, for the actuation voltages of 0 V, 7.5 V and 12 V, respectively. So, the narrow bandwidth of 0.389 GHz, is artificially extended to 1.008 GHz, offering an improvement of 159%. Finally, two snapshots of the electric field at two different arrangements of the device are given in Fig. 7.

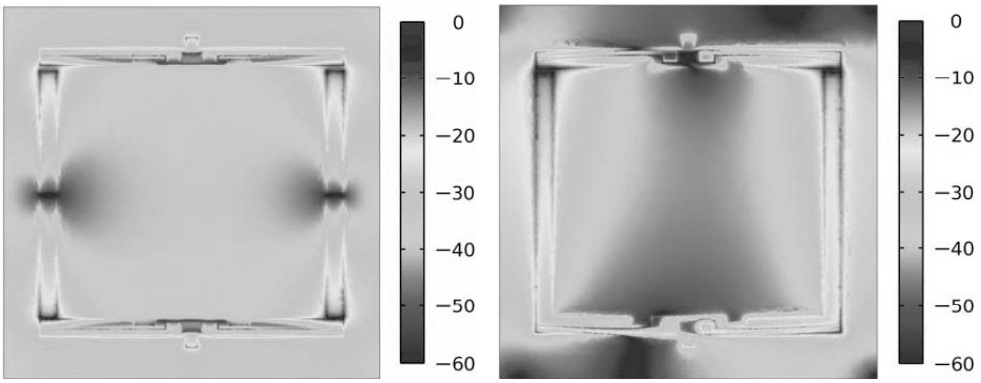

Fig. 7. Electric field snapshots of the electrothermally controlled complex material unit cell at 56.4 GHz, when the actuation voltage of both actuators is (a) 0 V and (b) 12 V.

The maximum values of the electric field intensity are observed at the regions of the gaps in both cases. It is confirmed that the lack of the lower gaps is responsible for the MNG performance of the second setup.

4. Conclusion

The capability of altering the essence of a complex medium utilizing double two-hot-arm electrothermal actuators has been numerically examined in this paper.

Furthermore, an MNG performance with tunable bandwidth has been proposed and accomplished. The proposed component could be advantageous in several millimeter wave applications.

Acknowledgements. This research has been cofinanced by the European Union (European Social Fund−ESF) and Greek national funds through the Operational Program "Education and Lifelong Learning" of the National Strategic Reference Framework (NSRF)−Research Funding Program: Aristeia I. Investing in knowledge society through the European Social Fund.

References

[1] L. SOLYMAR and E. SHAMONINA, *Waves in Metamaterials*, 1st ed., Oxford University Press, Inc., 2009.

[2] R. SINGH, I.A.I. AL-NAIB, M. KOCH and W. ZHANG, *Asymmetric planar terahertz metamaterials*, Opt. *Express* **18**, pp. 13044–13050, 2010.

[3] F.L. ZHANG, L. KANG, Q. ZHAO, J. ZHOU, X. ZHAO and D. LIPPENS, *Magnetically tunable left handed metamaterials by liquid crystal orientation*, Opt. Express **17**, pp. 4360–4366, 2009.

[4] S.M. XIAO, U.K. CHETTIAR, A.V. KILDISHEV, V. DRACHEV, I.C. KHOO and V.M. SHALAEV, *Tunable magnetic response of metamaterials*, Appl. Phys. Lett. **95**, pp. 033115(1–3), 2009.

[5] J.M. MANCEAU, N.H. SHEN, M. KAFESAKI, C.M. SOUKOULIS and S. TZORTZAKIS, *Dynamic response of metamaterials in the terahertz regime: Blueshift tunability and broadband phase modulation*, Appl. Phys. Lett. **96**, pp. 021111(1–3), 2010.

[6] S. LUCYSZYN (Ed.), *Advanced RF MEMS*, 1st *ed*., Cambridge University Press, 2010.

[7] X. HE, Z. LV, B. LIU and Z. LI, *Tunable magnetic metamaterial based multi-split-ring resonator (MSRR) using MEMS switch components*, Microsystem Technol. **17**, pp. 1263–1269, 2011.

[8] D. BOUYGE, D. MARDIVIRIN, J. BONACHE, A. CRUNTEANU, A. POTHIER, M. DURAN-SINDREU, P. BLONDY and F. MARTIN, *Split ring resonators (SRRs) based on micro-electromechanical deflectable cantilever-type rings: Application to tunable stopband filters*, IEEE Microw. Wireless Lett. **21**, pp. 243–245, 2011.

[9] W. ZHANG, W.M. ZHU, Y.H. FUL, J.F. TAO, D.P. TSAI, G.Q. LO, D.L. KWONG and A.Q. LIU, *A THz dual mode switch using MEMS switchable metamaterial*, Proc. 24th Int. Conf. MEMS **21**, pp. 672–675, 2011.

[10] D. YAN, A. KHAJEPOUR and R. MANSOUR, *Modeling of twohot-arm horizontal thermal actuator*, J. Micromech. Microeng. **13**, pp. 312–322, 2003.

[11] L. LI and D. UTTAMCHANDANI, *Modified asymmetric micro-electrothermal actuator: analysis and experimentation*, J. Micromech. Microeng. **14**, pp. 1734–1741, 2004.

[12] H. TAO, A.C. STRIKWERDA, K. FAN, W. PADILLA, X. ZHANG and R.D. AVERITT, *MEMS based structurally tunable metamaterials at terahertz frequencies*, J. Infrared Milli. Terahz Waves **32**, pp. 580–595, 2010.

[13] A.X. LALAS, N.V. KANTARTZIS, T.V. YIOULTSIS and T.D. TSIBOUKIS, *Tunable metamaterial devices by means of two-hot-arm electrothermal actuators*, Proc. 12th MEMSWAVE, Athens, Greece, 2011.

[14] MUMPs (Multi User MEMS Processes) foundry process, MEMSCAP Inc., online at http://www.memscap.com.

[15] X. CHEN, T.M. GRZEGORCZYK, B.I. WU, J. PACHECO and J.A. KONG, *Robust method to retrieve the constitutive effective parameters of metamaterials*, Phys. Rev. **E70**(1), pp. 016608(1–7), 2004.

A Carbon Nanotubes Ridge Gap Resonator

A.M. SALEEM[a,b], S. RAHIMINEJAD[a], V. DESMARIS[b], P. ENOKSSON[a]

[a]Department of Microtechnology and Nanoscience, Chalmers University of TechnologySE-412 96 Gothenburg, Sweden
[b]Smoltek AB, Regnbågsgatan 3, SE-417 55 Gothenburg Sweden
Tel: +46 (0)760-520053

Abstract. The extra ordinary electronic properties of carbon nanotubes have made them a highly attractive material for applications like interconnects and microwave electronics. Their quick fabrication process has given them further advantage to be chosen as a first material for these applications. In this paper we present a novel process to fabricate a microwave device using carbon nanotubes not as the main active part but as a core material coated with a 1 μm aluminum layer. A carbon nanotube based ridge gap resonator was fabricated and demonstrated for the first time for the frequency range 200–325GHz. The process is not limited to these frequencies and enables the fabrication of gap wave based device using carbon nanotubes as core for a wide range of frequencies and applications.

1. Introduction

Carbon nanotubes (CNTs) are tubular structures made up by rolling of graphene sheets. These structures were discovered by Iijima in 1991[1] and since then these have got huge attention due to their extraordinary electronic, thermal and mechanical properties. CNT's are in fact many-fold stronger than steel, harder than diamond, better electrical conductors than copper and better thermal conductor than diamond. The electronic properties depend on how the graphene sheet is rolled up. They can be metallic or semiconducting accordingly. These are very high aspect ratio structures with diameter ranges from < 1 nm up to 50 nm with length exceeding even 1 mm with an approximate growth time of 45 minutes [2]. Due to these combined extra ordinary properties, these structures have potential application in many technologies like interconnect, gas storage, conductive plastics, flat panel displays and super capacitors.

In addition to take advantage of the superior electrical properties of CNTs for RF waveguide application, CNTs have the attracting attribute of their simple and quick fabrication process at the expanse of relatively cheaper resources. The

waveguide and resonator made out of Silicon and copper have been already demonstrated [3, 4]. In first case where structures are made from silicon, the processing includes a thick Aluminum layer metal deposition as well as 280 μm deep dry etching of silicon which can take few hours followed by wet etching of the thick aluminum layer whereas the structures made from Copper involve longer photolithography of SU8, Copper electroplating and etching of the Silicon wafer. In short expensive resources are used, infact, to make waveguides or resonator out of silicon or copper.

In this paper we demonstrate for the first time the use of CNTs to build a ridge gap resonator for the frequency range of 220–325 GHz. For the gap waveguides, the waveguide is made in the gap between two parallel metal plates.

Gap waveguide technology relies on utilizing a metamaterial, in this case a "bed of nails" [5], which forms an *Artificial Magnetic Conductor* (AMC). A parallel-plate stopband is created for a certain frequency band by placing a *Perfect Electrical Conductor* (PEC) opposite to an AMC. Nevertheless if the AMC layer introduces a guiding PEC structure such as ridge, groove or stripes, waves will propagate along these ridges, grooves or stripes without leaking away from the structure and hence such parallel plate structures can be used as transmission lines as shown in Fig. 1. In [3] simulations of the confinement of the wave inside the resonator can be seen. A gap waveguide demonstrator for 10-20 GHz was presented in 2011 [6] and since then many different gap waveguide components have been designed at high frequencies and have already been presented, *e.g*. the ridge gap resonator made in Si for the 220–325 GHz frequency band [3] and the pin-flange adapter [7]. The complete waveguide packaging compatible for THz frequency and also compatible with different THz component technology is also shown in [8].

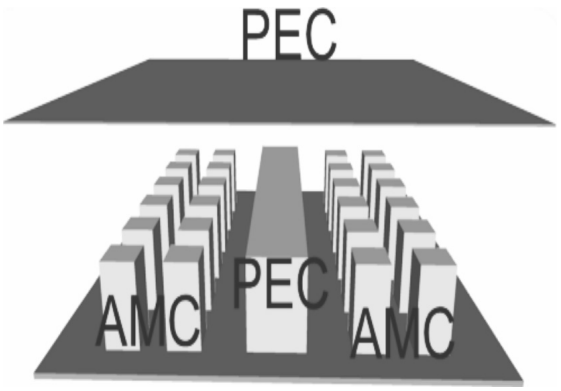

Fig. 1. Illustration of the principle for a ridge gap waveguide [3].

2. Design

The ridge gap resonator is designed for the 220–325 GHz frequency band, based on the ridge-gap resonator presented in [3]. In this work the resonator is

fabricated using CNTs instead of silicon as the core material. The frequency band for the design of this demonstrator was chosen according to the measurement system available for a fair a comparison to the readily existing devices. The ridge and the pins are fabricated at the same time. The pin width is 165 μm with its intended height of 277 μm and the length of the ridge as 2057 μm for the same intended height of 277 μm. It is a bottom up technique where carbon nanotubes are grown on the silicon wafer to obtain carrier and pins instead of top down technique where pins and carrier are obtained by etching down Silicon.

3. Fabrication

The fabrication process scheme of carbon nanotubes based ridge gap resonator is shown in Fig. 2.

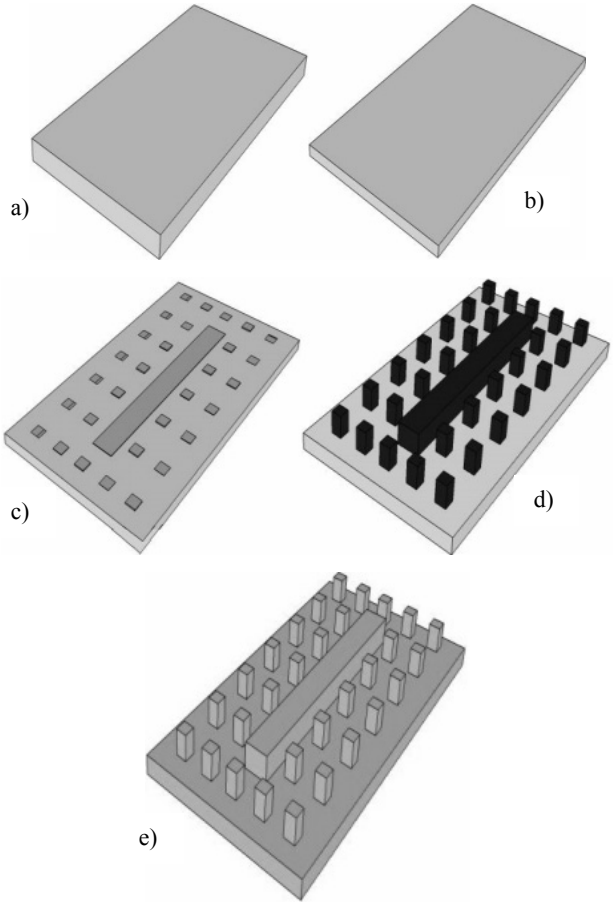

Fig. 2. Process plan of the resonator. a) 2'' N-type silicon wafer of thickness around 280 μm. b) Wafer is thin down to around 200um using SF6 plasma etching. c) Definition of catalyst using lithography. (d) Growth of carbon nanotubes using thermal CVD. f) Deposition of aluminum/titanium/goldconductive seed layer.

A 2'' single side polished silicon wafer is thinned down to about 200–215 μm, Fig. 2a and 2b, from its non-polished side using ICP, in order to achieve the right carrier thickness so that it can be fitted in the measurement equipment of the same fixture as used for the silicon resonator [3].

The catalyst is patterned using lift-off image reversal lithography with AZ5214 photo resist. Either 5 nm aluminum or 30 nm aluminum oxide is evaporated first and then 2 nm iron is evaporated in the same run using an electron beam evaporation machine followed by lift-off in 1165 remover, IPA and water (see Fig. 2c). The wafer was diced and 265–300 μm long carbon nanotubes are grown by thermal chemical vapor deposition in AIXTRON NanoInstruments Black Magic. Bundles of CNTs were grown at 700°C using acetylene and hydrogen gasses as a carbon source and carrier, respectively, as shown in Fig. 2d. First, the catalyst was pretreated at 500°C in the environment of continuous hydrogen flow at around 8 mbar pressure. In next step acetylene was introduced and the temperature was raised to 700°C within a few seconds. After growth, 1 μm of aluminum, 15 nm Titanium and 100 nm gold were sputtered sequentially to fill the gap between carbon nanotubes and to provide a conductive top surface, (see Fig. 2e). The thickness of the metal layer is chosen to more than five times skin depth of the targeted frequency band. The cross section of the silicon base, carbon nanotubes and the metal covering layer is shown in Fig. 3.

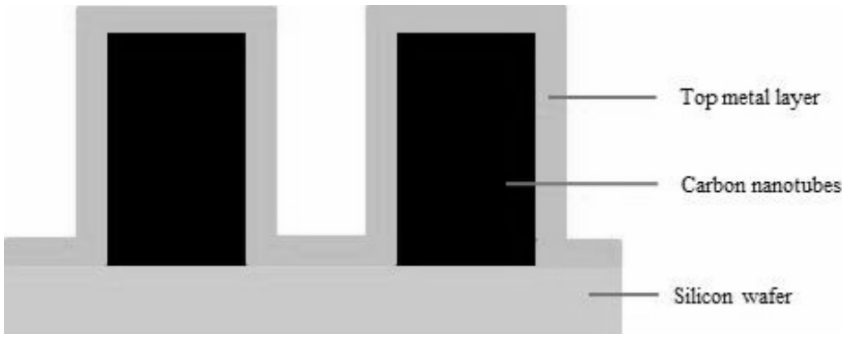

Fig. 3. The cross section of the silicon base, carbon nanotubes and the metal covering layer.

4. Results & Discussion

A carbon nanotube based ridge gap resonator was fabricated. A SEM image of the pins and carrier is shown in Fig. 4. Fig. 5 shows the ridge gap resonator made from carbon nanotubes. Here, the frequency range between 220 to 325 GHz is chosen, due to measurement system limitations, however these structures are not limited to this frequency range only. It is possible to make for higher frequencies by scaling down the structures. In order to make resonators for double frequency range it is only needed to scale it down to half due to linear relationship between frequency and feature size. Similarly in order to make ridge gap resonator for lower

frequencies it is only needed to scale up these structures. The carbon nanotubes of length 1mm are grown commonly now a day so these structures are able to cover a wide range of frequencies. Just looking at the possible dimensions *e.g.* for around 1 mm long CNTs one could target the 60 GHz band and for a single CND as a nail in the bed of nails these can be shrunk by 5 orders of magnitude thus to be appropriate for a staggering 30 000 THz. The full investigation measurements will be presented at the conference.

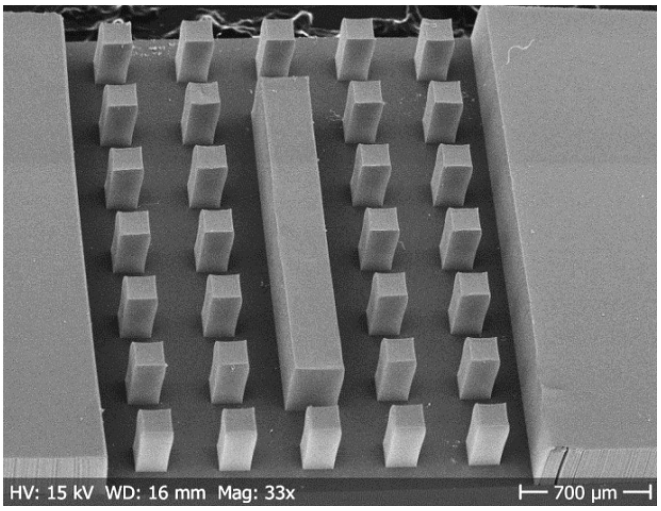

Fig. 4. SEM image of the Carbon nanotubes ridge gap resonator before metal sputtering.

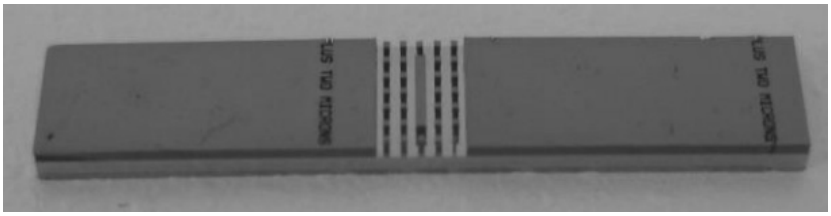

Fig. 5. Ridge gap resonator made out of carbon nanotubes.

5. Conclusion

The fabrication process of a carbon nanotubes tubes based ridge-gap resonator was demonstrated successfully for the first time for the 220–325 GHz frequency band. This structure has the ability to be made for many different frequency ranges both higher and lower than what is manufactured here. They are quick and cheap to fabricate.

Acknoledgements. This work has been supported by SMOLLTEK AB. The authors are grateful to the nanofabrication laboratory at the Chalmers University of Technology for their help with the fabrication process.

References

[1] S. IIJIMA, *Helical microtubules of graphitic carbon*, Nature **354**, pp. 56–58, 1991.

[2] G. XIONG, D.Z. WANG, Z.F. REN, *Aligned millimeter-long carbon nanotube arrays grown on single crystal magnesia*, Carbon **44**, pp. 969–973, 2006.

[3] S. RAHIMINEJAD, A.U. ZAMAN, E. PUCCI, H. RAZA, V.VASSILEV, S. HAASL, P. LUNDGREN, P.-S. KILDAL and P. ENOKSSON, *Micromachined Ridge Gap Waveguide And Resonator For Millimeter-Wave Applications*, Sensors & Actuators **A186**, pp. 264–269, 2012.

[4] V. DESMARIS, D. MELEDIN, A. PAVOLOTSKY, R. MONJE, V. BELITSKY, *All-metal micromachining for the fabrication of sub-millimetre and THz waveguide components and circuits*, J. MICROMECH. MICROENG. 18, PP 095004, 2008.

[5] M. SILVEIRINHA, C. FERNANDES and J. COSTA, *Electromagnetic characterization of textured surfaces formed by metallic pins*, IEEE Transactions on Antennas and Propagation **56**(2), pp. 405–415, 2008.

[6] P.-S. KILDAL, A. UZ ZAMAN, E. RAJO-IGLESIAS, E. ALFONSO and A. VALERO-NOGUEIRA, *Design and experimental verification of ridge gap waveguides in bed of nails for parallel plate mode suppression*, IET Microwaves, Antennas & Propagation. **5**, pp. 262–270, 2011.

[7] S. RAHIMINEJAD, E. PUCCI, S. HAASL and P. ENOKSSON, *Contactless Pin-Flange Adapter For High-Frequency Measurements*, 23RD Micromechanics and Microsystems Europe Workshop, September, Ilmenau, Germany, 2012.

[8] V. DESMARIS, D. MELEDIN, D. DOCHEV, A. PAVOLOTSKY, V. BELITSKY, *Terahertz components packaging using integrated waveguide technology*, IEEE MTT-S International Microwave Workshop on Millimeter Wave Integration Technologies, IMWS, pp. 81–84, 2011.

Design of an UWB Antenna with a Novel Reconfigurable MEMS Band Notch Actuated Without Bias Lines

Arash NEMATI, Bahram Azizollah GANJI

Babol University of Technology, Electrical & Computer Engineering Department
P.O. Box 484, Babol, Iran
E-mail: Arash.Nemati@stu.nit.ac.ir, baganji@nit.ac.ir

Abstract. An *UltraWideBand* (UWB) CPW-fed elliptical monopole antenna with reconfigurable rejection band (band notch) characteristic at the WLAN band (5.15_5.825 GHz) is presented. *Micro-ElectroMechanical System* (MEMS) afloat is used to activate and deactivate the band notch characteristic without the need of extra dc bias lines due to a novel design. When the dc actuation voltage is applied to the CPW center line, the λ/2 long U-shaped afloat moves down and creates a slot (resonating element) in its vacant place. Whereas no voltage is applied, the afloat remains in the up position and serves as a part of antenna. In addition to parametric study, Trans-mission line model and surface current distribution are used to explain the effect of movable afloat. The gain of the antenna is about 3.2 dBi over the entire UWB frequency band (3.1_10.6 GHz), while it is less than 7 dBi at the rejection band.

1. Introduction

In recent years, Due to the attractive features, such as low cost, small size, ease of fabrication, and wide frequency bandwidth, there has been more attention in ultrawideband (UWB) monopole antennas. The Federal Communication Commission (FCC) has allocated 3.1–10.6 GHz for commercial ultrawideband (UWB) commu-nication systems [1]. The frequency range for UWB system will cause interference to the WLAN systems in 5.15–5.825 GHz. In order to solve this problem, hemi-cycle shaped slot created on antenna. This slot caused band rejection in WLAN systems frequency range. To overcome this problem, structures with band-rejection characteristic such as U-shaped slot [2, 3], and arc-shaped slot [4] are proposed to integrate with the former antennas. However none of those antennas had reconfigurable band notch characteristics. The main challenge for

researchers in UWB antenna design is the design of a single antenna that can provide ON=OFF control of the rejected band. A pin diode is used in [5] to switch ON or OFF The notch band. However the switches were actuated using dc bias lines.

In this paper, an UWB monopole antenna with a U-shaped MEMS afloat that can be actuated to place a band notch at the WLAN frequencies is presented. The MEMS afloat is designed so that it does not require extra bias lines; the bias is applied to the RF signal line. The lack of bias lines for the MEMS afloat in the proposed topology improves the radiation performance of the antenna since there is no coupling or leakage from the bias lines.

2. Atenna Design and Analysis

Figure 1 shows the geometry of the reconfigurable WLAN band rejection UWB elliptical monopole antenna. The antenna was designed on a 26 mm×40 mm *Liquid Crystal Polymer* (LCP) substrate with a dielectric constant of 3, tan δ = 0.002, and a thickness of 0.1 mm [6]. Thickness of the antenna and the ground is 5 μm. In this paper an afloat is used instead of a simple slot. The afloat is hold by 16 beams and they are attached to the antenna in 8 points. The dimensions of the antenna and afloat are summarized in Table 1. UWB antenna simulations were performed with the CST Microwave Studio 2012 (MWS) based on the finite integration method (FIM).

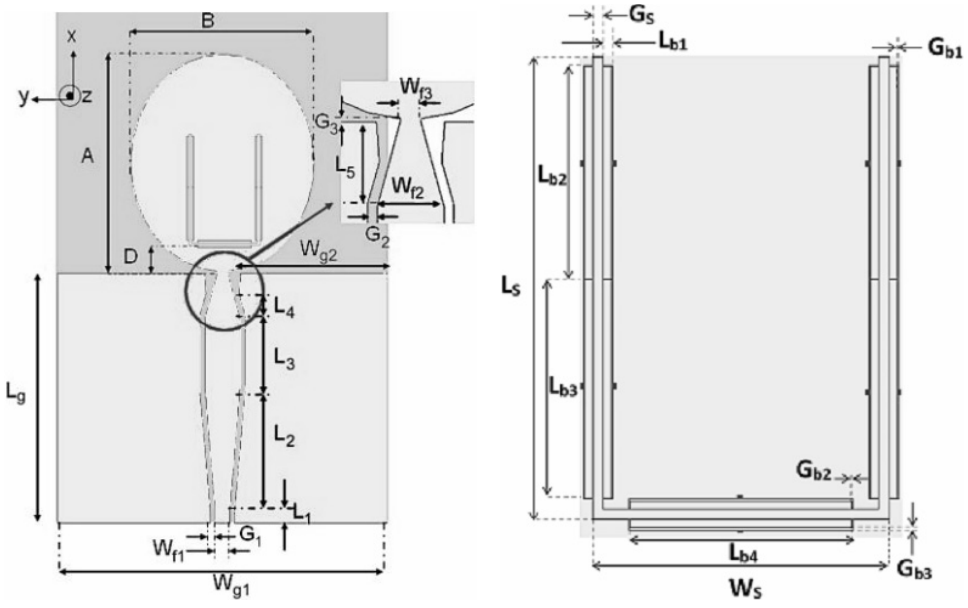

a) b)

Fig. 1. Schematic diagram of (a) monopole antenna and (b) U-shaped afloat.

Table 1. Antenna and afloat dimensions

L_1	1.000 mm	W_{g1}	26.000 mm	G_S	0.200 mm
L_2	0.000 mm	W_{g2}	12.250 mm	W_S	5.600 mm
L_3	5.000 mm	W_{f1}	1.280 mm	L_{b1}	0.150 mm
L_4	1.930 mm	W_{f2}	2.970 mm	L_{b2}	4.045 mm
L_5	3.700 mm	W_{f3}	0.850 mm	L_{b3}	4.150 mm
D_1	2.600 mm	L_g	20.700 mm	L_{b4}	4.200 mm
G_1	0.050 mm	A	18.000 mm	G_{b1}	0.025 mm
G_2	0.100 mm	B	15.300 mm	G_{b2}	0.010 mm
G_3	0.110 mm	L_S	8.800 mm	G_{b3}	0.050 mm

Afloat and the beams are disported from the antenna by a 1 μm width and 5 μm groove. Beams are attached to the antenna with 8 bridges. Bridges positions are indicated with red points in Fig. 2 (b). They have 1 μm long and 50 μm width. There is groove with depth of h = 45 μm under the afloat and its beams. A 1 μm thick high resistive sheet, underneath a passivation layer, is at the bottom of the groove witch is connected to the ground. When the dc actuation voltage is applied to the CPW center line, the λ/2 long U-shaped afloat moves down (45 μm) and creates a slot (resonating element) in its vacant place Fig. 2a). Whereas no voltage is applied, the afloat remains in the up position and serves as a part of the antenna which eliminates the resonance Fig. 2b).

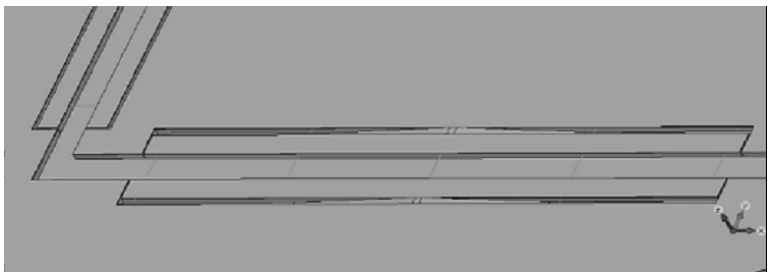

a)

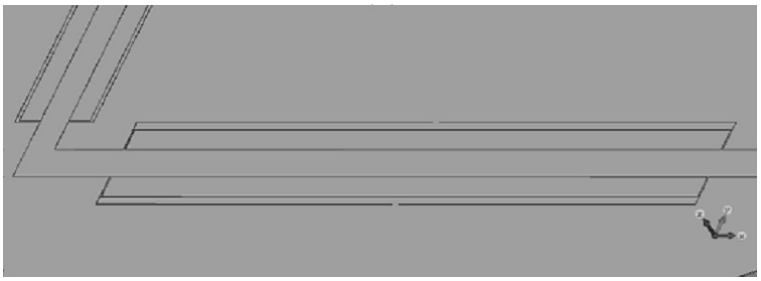

b)

Fig. 2. Schematic diagram of U-shaped afloat in (b) down position and (c) up position.

The total length of the slot is approximately λ/2 (considering the effect of $\sqrt{\varepsilon_{eff}}$ at the frequency at which the rejection band is desired (around 5.5 GHz). The relation between central notched frequency and afloat dimensions can be expressed approximately as follows [1]:

$$f_U \cong \frac{C}{4\left(L_S + \left(W_S/2\right) - G_S\right)\sqrt{\varepsilon_{eff}}} \tag{1}$$

where c is the speed of light.

Figure 3 shows the Surface current distribution in two frequencies. As shown in Fig. 3(a), when the afloat is in down position the current density in the edges of the U-shaped slot is stronger than any other area at the notch frequency of 5.5 GHz. The direction of the currents in the inner and outer side of the U-shaped slot are opposite to each other as presented in [7]. Therefore they cancel each other and the antenna does not radiate. On the other hand, in Fig. 3(b), we can see stronger current distributions concentrated near the outer edges of the antenna at the center frequency of the corresponding notched band. At a passband frequency of 8 GHz (outside the notched band), the distribution of the surface current is uniform near the outer edges of the antenna as shown in Fig. 3(c).

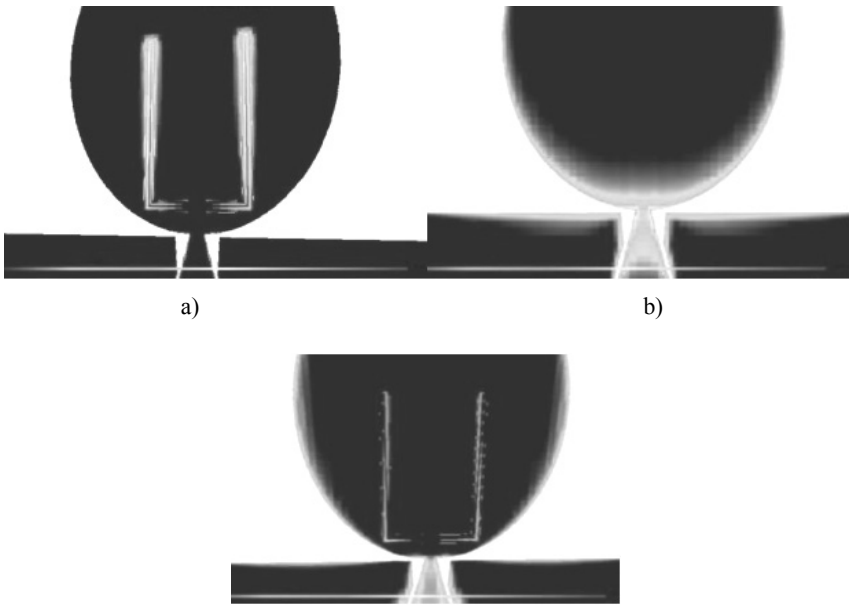

a) b)

c)

Fig. 3. Simulated Surface current distributions (a) afloat down at 5.5 GHz, (b) afloat up at 5.5 GHz, (c) afloat down at 8 GHz.

The slot can be modeled by a short circuit terminated series stub in a transmission line model as shown in Fig. 4. The presence of the slot is modeled as a long, short circuit terminated series stub, which is similar to a spurline filter. If the afloat is down, Fig. 4a) the spurline filter is in the circuit, and at the stub resonant frequency, there is an equivalent series open circuit that reflects the signal. Whereas the afloat is up, the spurline filter is not connected to the circuit Fig. 4b), or not in the circuit. Thus, rad-iation occurs at all frequencies.

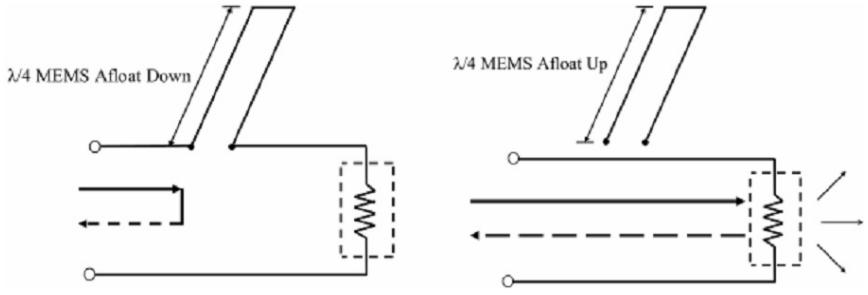

Fig. 4. Transmission line model for antenna with (a) U-shaped afloat down, (b) U-shaped afloat up.

Fig. 5 indicates the simulated S11 results for the proposed antenna. The simulated plots for the "Reference" antenna (the antenna presented in Fig. 1a) without the afloat) and the U-shaped slot antenna when the afloat is up (MEMS up) are in very good agreement. The presented return loss simulations verify the good performance of the MEMS afloat and the effectiveness of the suggested integration. Fig. 6 shows the simulated gain of the antenna. It is found that gain decreases sharply over 7 dBi in the notched band. For other frequencies out of the notched band, the antenna exhibits moderate gain about 3.2 dBi.

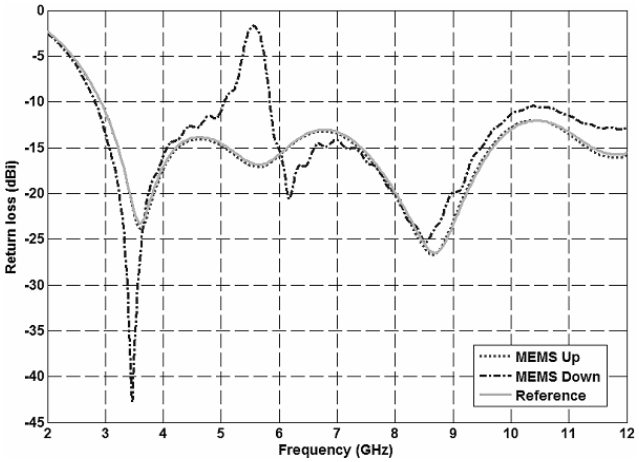

Fig. 5. Simulated (a) Return loss.

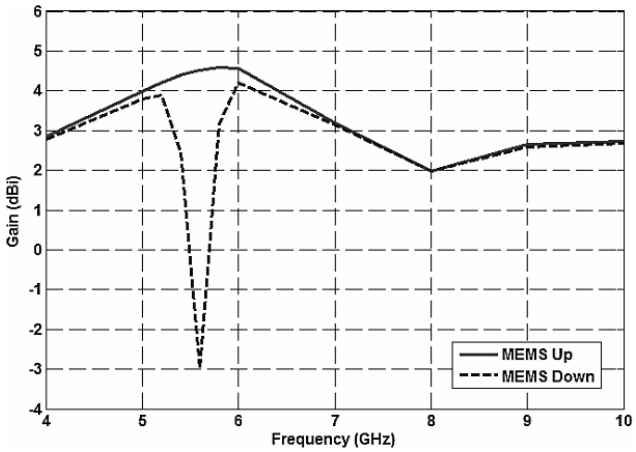

Fig. 6. Simulated Realized Gain for the antenna.

Figure 7 shows simulated S11 characteristics with the opti-mum values of other dimensions and for different values of L_S. As the L_S increases from 7.8 to 9.8 mm, the center frequency of notched band is varied from 5.1 to 6.1 GHz. From this result, one can conclude that the frequency of notched band is controllable by changing length L_S. It can be seen that by changing L_S the bandwidth of notch remains almost fixed.

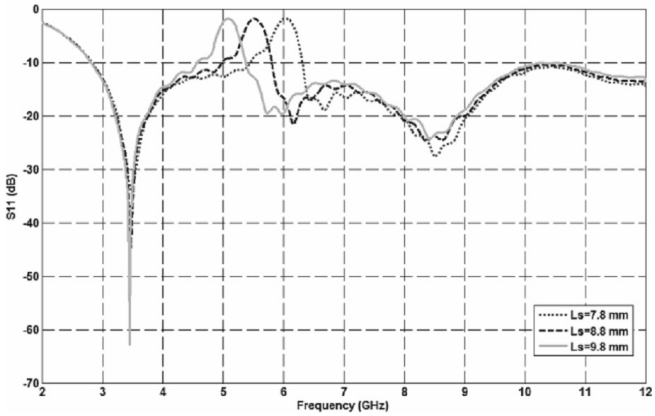

Fig. 7. Slot length effect on return loss with D=1.4, h=0.045, Ws=2.8, Gs=0.2

Figure 8 shows simulated S11 characteristics with the opti-mum values of other dimensions for different values of h. As the length h increases from 25 to 65 μm, the center frequency of notched band is varied from 5.4 to 5.7 GHz. From this result, one can conclude that the frequency of notched band increases 50 MHz for every 20 μm increase of h. It can be seen that the bandwidth of notch remains almost fixed.

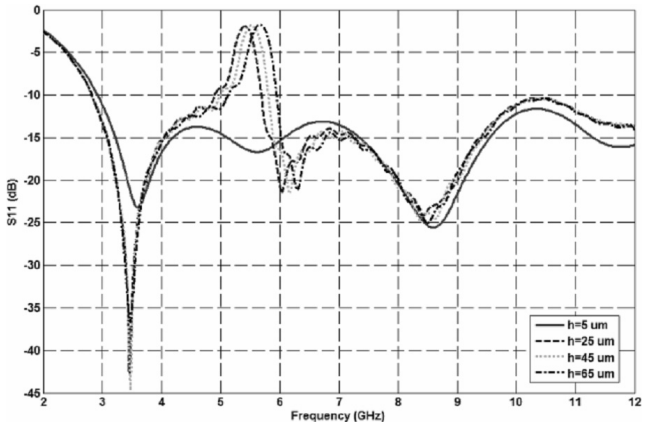

Fig. 8. Slot height effect on return loss with D = 1.4, Ls = 8.8, Ws = 2.8, Gs = 0.2.

Figure 9 shows the afloat displacement versus voltage under bias condition from 0 V to 16 V. The deflection as a function of voltage increases slightly until a drastic change occurs indicating the pull in voltage of the afloat about 16 V which is low and permanent. In this paper, the MEMS mechanical structure is simulated using the Intellisuite which is a multiphysics simulator that uses the finite element method.

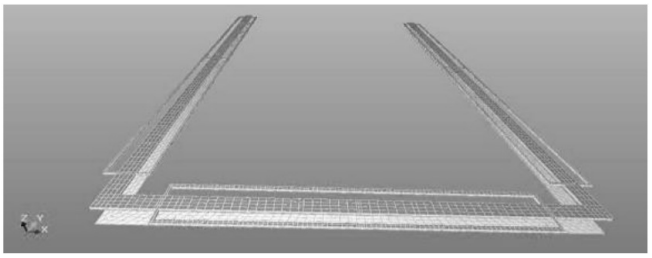

a)

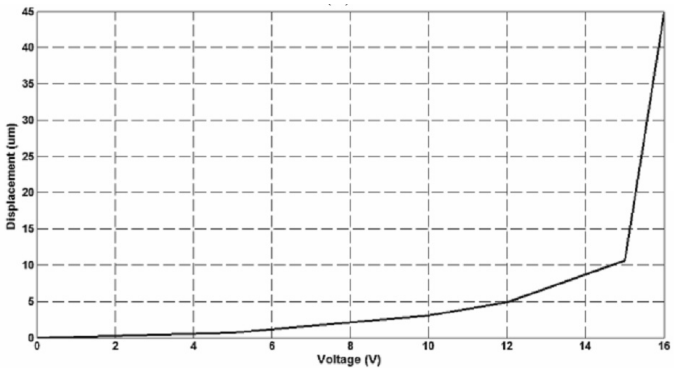

b)

Fig. 9. (a) The MEMS afloat and ground in simulator are shown.
(b) Afloat displacement vs. DC voltage.

Simulations at 5.5 and 8 GHz are presented in both E (x-y) and H (x-z) planes. Figure 10 shows the radiation patterns for the antenna. The two states (MEMS afloat up and down) of the reconfigurable antenna are compared with the "Reference" antenna. It is seen (radiation patterns at 8 GHz) that the addition of the resonating elements does not affect the radiation performance of the antennas in frequencies outside the notch band. On the other hand, within the band-notch range (radiation patterns at 5.5 GHz) and with the appropriate MEMS switch state the radiated field intensity is degraded Fig. 10a) and c).

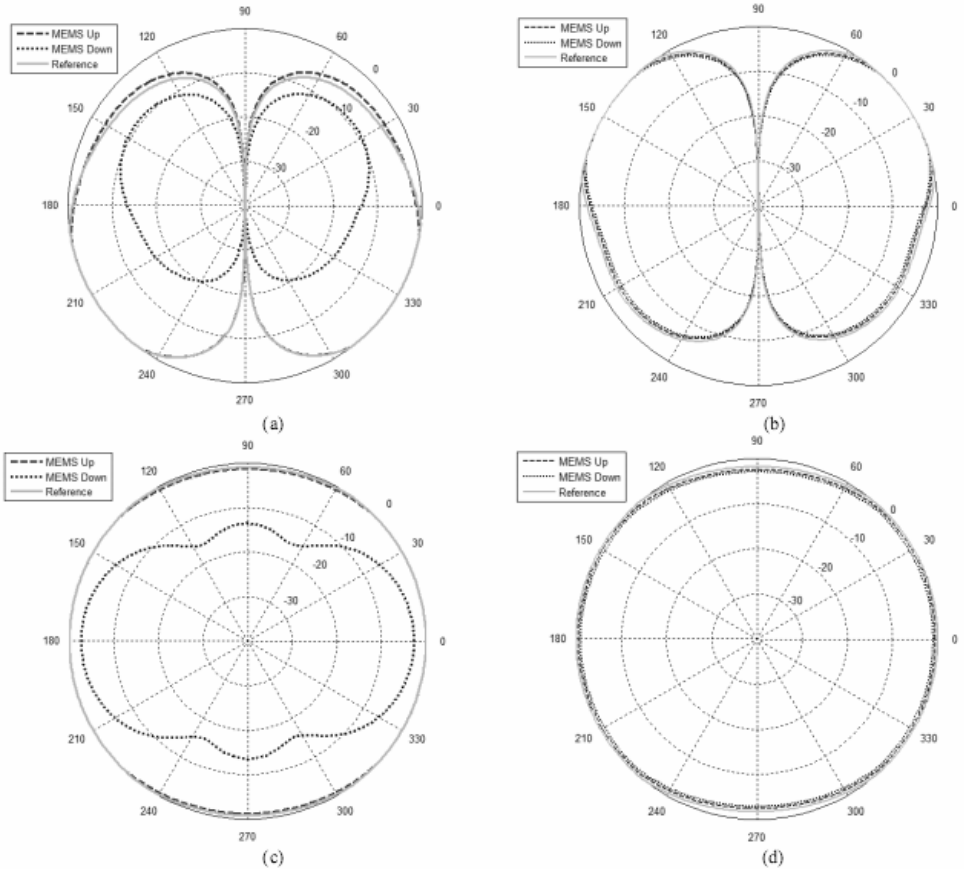

Fig. 10. radiation pattern simulations (a) E plane at 5.5 GHz, (b) E plane at 8 GHz, (c) H plane at 5.5 GHz, (d) H plane at 8 GHz.

3. Conclusion

An ultrawideband (UWB) CPW-fed elliptical monopole antenna with reconfigurable rejection band (band notch) characteristic at the WLAN band (5.15_5.825 GHz) is presented and discussed. To obtain Reconfigurability, a λ/2

long U-shaped MEMS afloat that is actuated through the RF signal path, without the need of dc bias lines, is used. The effects of the various geometrical parameters on the notched frequency band are studied. The pull in voltage of the afloat was low and its switching was permanent. Due to a novel afloat design, the proposed antenna has good omnidirectional pattern in different frequencies and the addition of the resonating elements does not affect the radiation performance of it in frequencies outside the notch band.

References

[1] Federal Communications Commission Revision of Part 15 of the Commission's Rules Regarding Ultra-Wideband Transmission System from 3.1 to 10.6 GHz. In: FEDERAL Communications Commission. Washington, DC: ET-Docket, FCC; 2002. p. 98–153.

[2] Y.J. CHO, K.H. KIM, D.H. CHOI, S.S. LEE, S.-O. PARK, *A miniature UWB planar monopole antenna with 5-GHz band-rejectionfilter and the time-domain characteristics*, IEEE Trans Antennas Propag **54**, pp. 1453–60, 2006.

[3] T.P. VUONG, A. GHIOTTO, Y. DUROC, S. TEDJINI, *Design and characteristics of a small U-slotted planar antenna for IR-UWB*, Microw Opt Technol Lett. **49**, pp. 1727–31. 2007.

[4] S. KHAN, J. XIONG, S. HE, *Low profile and small size frequency notched planar monopole antenna from 3.5 to 23.64 GHz*, Microwave Opt Technol Lett. **50**, 2008.

[5] V.A. SHAMEENA, M.N. SUMA, K. RAJ ROHITH, P.C. BYBI and P. MOHANAN, *Compact ultra-wideband planar serrated antenna with notch band ON=OFF control*, Electronics Letters **42**(23), 9 November 2006.

[6] S. NIKOLAOU, N.D. KINGSLEY, G.E. PONCHAK, J. PAPAPOLYMEROU and M.M. TENTZERIS, *UWB Elliptical Monopoles with a Reconfigurable Band Notch Using MEMS Switches Actuated Without Bias Lines*, IEEE Trans. Antennas Propag. **57**(8), pp. 2242–2251, August, 2009.

[7] Y.J. CHO, K.H. KIM, D.H. CHOI, S.S. LEE AND S.-O. PARK, *A minia-ture UWB planar monopole antenna with 5-GHz band-rejection filter and the time-domain characteristics*, IEEE Trans. Antennas Propag. **54**(5), pp. 1453–1460, May, 2006.

Residual Stress and Switching Transient Studies for BiCMOS Embedded RF MEMS Switch Using Advanced Electro-Mechanical Models

A. MEHDAOUI[1], S. ROUVILLOIS[1], G. SCHRÖPFER[1], G. LORENZ[1], M. KAYNAK[2], M. WIETSTRUCK[2]

[1]COVENTOR Sarl, 3 avenue du Quebec Z-I de Courtaboeuf, 91140 Villebon sur Yvette, France
[2]IHP, Im Technologiepark 25, 15236 Frankfurt (Oder), Germany

Abstract. This paper presents parameters investigation of BiCMOS embedded RF MEMS switches, like residual stress, actuation voltage and switching transient by using advanced electro-mechanical models in the MEMS/IC co-design platform MEMS+ integrated with CADENCE tools. Simulations are performed and compared to the measurements. An equivalent model has been developed and validated by experiments. The model accurately predicts residual stress and switching transient. The minimum actuation voltage required to close the switch is around 30V. The switching speed of the RF switch is around 50 µs. This model includes fully coupled multiphysics such as fluids mechanics (squeeze film damping, pressure adjustments), structural mechanics (equivalent mass, young modulus and pre-stress models) and electrostatics.

Index Terms: RF MEMS switch, MEMS modeling, transient, residual stress, switching time, squeeze film damping.

1. Introduction

Over the past several years, RF MEMS such as switches, varactors, inductors etc. have become technologically competitive enough to enter the market place. RF MEMS switches are the most common and basic circuit elements. However, successful design and manufacture of these components is still very challenging. *Computer-Aided Design* (CAD) tools are thus needed to support rapid design of RF MEMS Switches involving physical interactions between multiple physical domains (*e.g.*, mechanical, electrostatic, magnetic and fluidic domains).

We investigate in this paper BiCMOS embedded RF MEMS switch parameters, like the residual stress, actuation voltage and switching transient by using advanced electro-mechanical models in the commercial MEMS/IC co-design platform named

MEMS+ [1]. Simulations are performed on the platform MEMS+ integrated with Cadence [2] and compared to measurements. The modelling methodology has been presented in detail earlier [3] and allows the MEMS designers to work in a 3-D environment that delivers fast, accurate and parameterized models of the MEMS device. The model parameters may include manufacturing variables, such as material properties and process parameters, as well as geometric properties and their variations. The specific example in this paper is a capacitive RF-MEMS switch built between Metal 2 and Metal 3 of IHP's 0.25 µm BiCMOS technology. High voltage electrodes are formed using Metal 1, while Metal 2 is used as RF signal line. The movable membrane was realized using the Metal 3 layer which is an AlCu layer stacked by TiN layers on top and bottom [4]. Figure 1 shows the IHP's RF switch quarter model in MEMS+, representing ¼ of the symmetric device. By applying a voltage between the high voltage electrode and the suspended membrane (Metal 3), the suspended membrane can be pulled towards the RF signal line (Metal 2). As the voltage is increased, pull-in occurs and the membrane collapses onto the RF signal line. In this way, the switch is closed and RF signals are able to pass through the device. The gap height between the membrane and the high voltage electrode is 2.62 µm. The gap height between the membrane and the RF signal line is 0.722 µm.

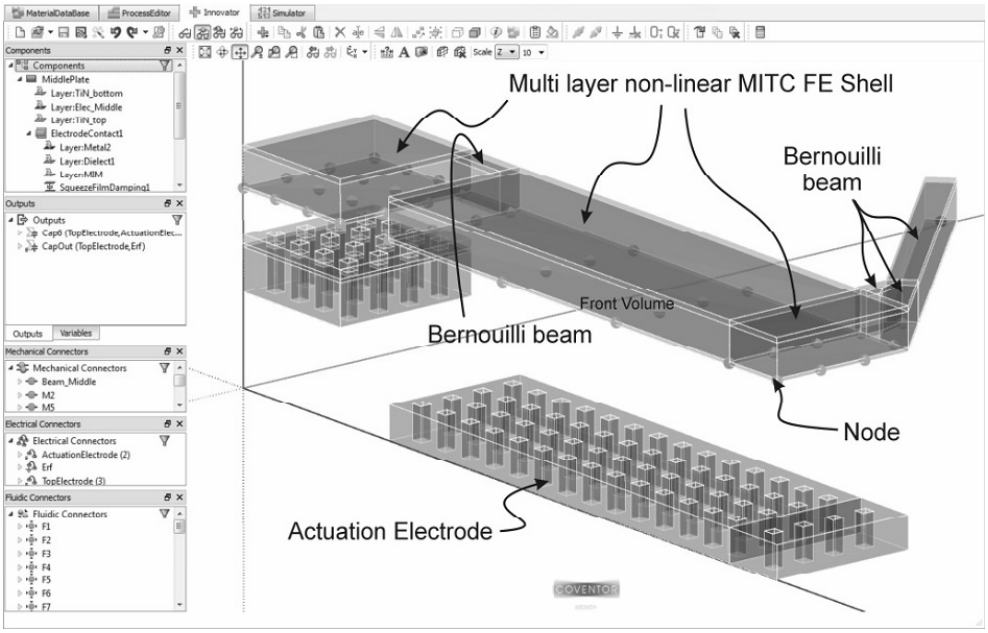

Fig. 1. IHP Nanotec RF switch quarter model in MEMS+ showing mechanical and electrostatic elements. The model also contains fluid models for squeeze-film damping, though these are not visible in the view mode shown. The model is scaled in z by 10 for clarity.

2. Equivalent Model Description

The movable suspended membrane model has solid plates instead of perforated ones, see Fig. 2a. In this configuration, perforations will be defined on the high voltage electrode and the RF signal line, see Fig. 2b.

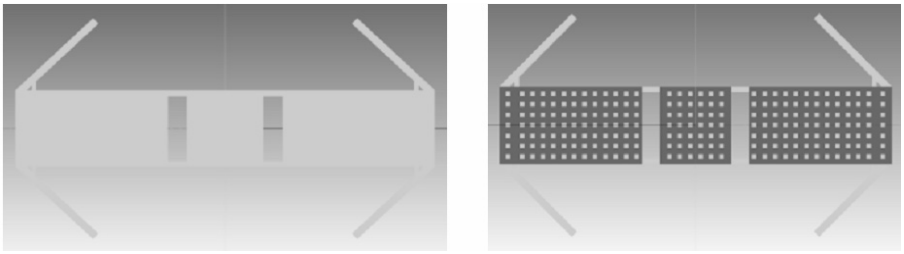

a) b)

Fig. 2. Equivalent Model of the RF Switch (a) top view of the suspended membrane, (b) bottom view of the model.

A. Influence of the pre-stress and Young's modulus

In this case, pre-stress values and young's modulus of the membrane are taken into account by adjusting the initial deflection due to the residual stress simulated in MEMS+ to the measured one. The maximum deflection due to the residual stress, measured at the center and the corner of the suspended membrane, are respectively around 0.48 µm and 0.5 µm, see below Fig. 3. In accordance with this deflection measurement, the new pre-stress and young's modulus of the movable membrane are summarized in the Table 1.

Table 1. Results of new pre stress and Young Modulus (equivalent model)

	Pre- stress (MPa)	Young's modulus (Mpa)
AlCu layer	450	95000
TiN layer on top	-550	710000
TiN layer on bottom	-960	710000

The simulated deflection corresponding to the new pre stress and Young's modulus are 0.45 µm and 0.52 µm, at the corner and the center respectively. Figure 3 shows the simulation performed by different tools (CoventorWare and MEMS+) and the measurement of the initial deflection due to the residual stress. It shows a good agreement between the measurement and the equivalent model simulation. Figure 4 shows the influence of different values of stress layer and Young's modulus on the initial deflection for AlCu layer. The stress is directly proportional

to the strain and the Young's modulus (Hooke's law).

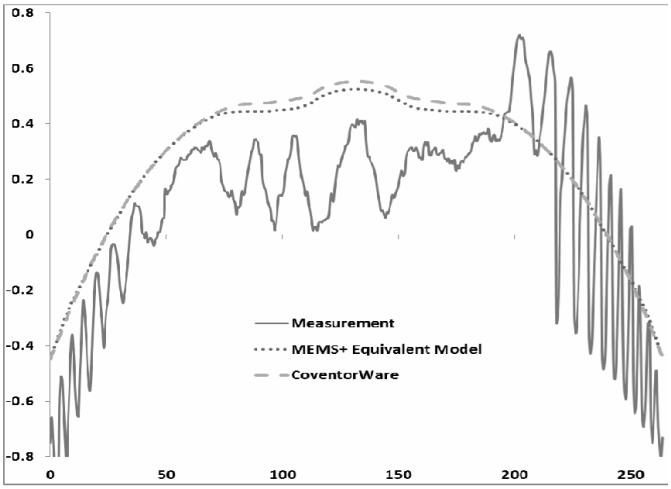

Fig. 3. Intial deflection due to the residual stress. Comparison between the measurement and the simulation using CoventorWare and MEMS+.

The equivalent RF switch is using a mechanical model for the suspended membrane with the new pre- stress and Young's modulus, an electrostatic one describing the electrostatic field and attracting forces between the membrane, the high voltage electrodes with perforations and the RF signal line with perforations and a fluidic one of the squeeze film damping forces acting on the moving membrane [5].

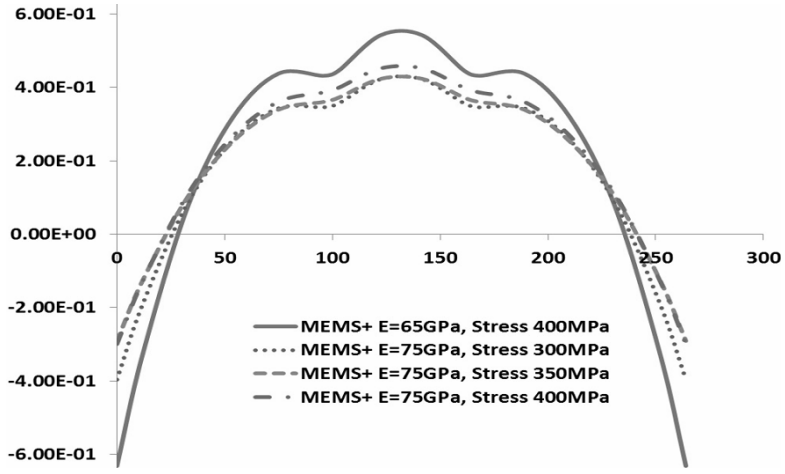

Fig. 4. Initial deflection of the membrane (AlCu layer) for different values of stress and Young's modulus.

B. Influence of the density

Instead of having perforations on the movable plate, we define it on the high voltage electrodes and RF signal line. The perforated plate is illustrated in Fig. 5. The perforated plate is assumed to be composed of repetitive identical plate unit cells. Parameter D specifies the fraction of holes as $D = \frac{A_{holes}}{A_{unit}}$. The size and the holes space defined on the Metal 1 and 2 are respectively 2 μm and 4 μm. In that case, D = 0.88.

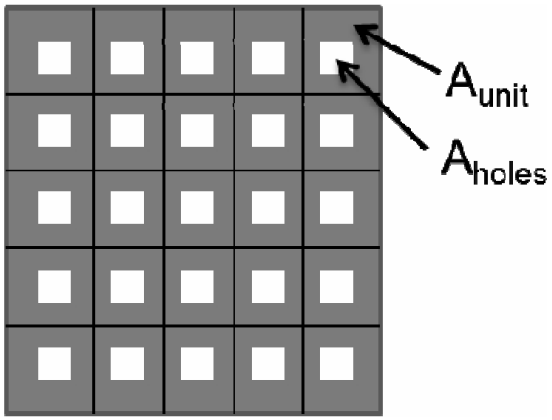

Fig. 5. Perforated plate units element.

To find an optimal model, the measured resonant frequencies, see Fig. 6, should fit with the simulated resonant frequencies (Fig. 7). The Fig. 7 shows the simulation of the resonant frequency for different values of the membrane density. The density of the equivalent model is defined as: parameter D. Density We simulate the resonant frequency for three values of the parameter D: 0.8, 0.9 and 1.

For different values of D (0.8, 0.9) and 1, Fig. 7 shows a resonant frequency at 101 kHz, 97 kHz and 90 kHz respectively. The optimal simulated resonant frequency in accordance with the measurement is 101 kHz, corresponding to a D parameter of 0.8. This value, expected, enables to define a plate model with square perforation of 2 μm and the holes space of 4 μm. Then the equivalent model will take account on the movable electrode new density (Density x D), Young Modulus and pre stress values (see Table 1).

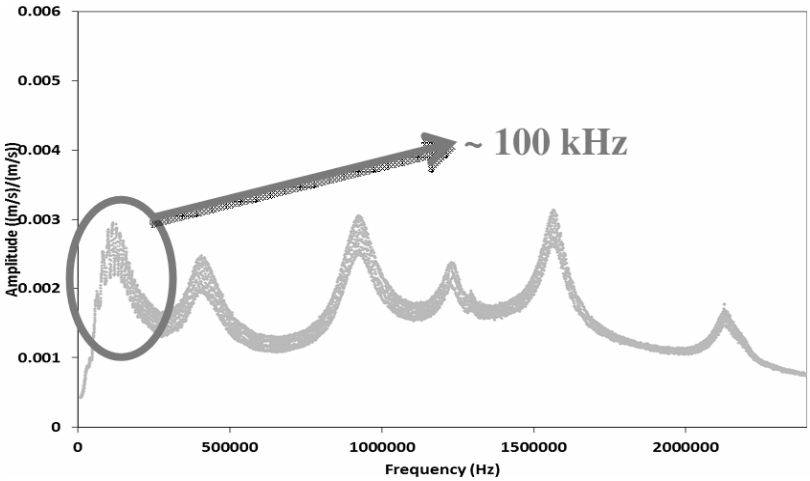

Fig. 6. Frequency response function (Measurement).

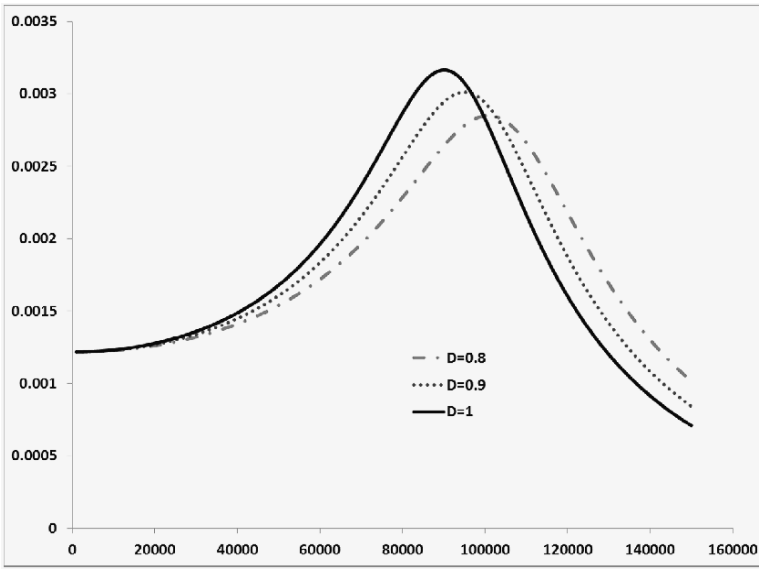

Fig. 7. Frequency response function Mode 1, simulated on MEMS+ for different values of parameter D.

3. Results and Discussion

Both static and transient analysis are performed for the RF switch. The actuation voltage analysis was performed to find out the minimum actuation voltage to close the switch. From this analysis it was confirmed that the minimum actuation voltage required to close the switch is around 30V. Fig. 8 shows the

vertical displacement of the membrane versus actuation voltage. We have a good agreement between the measurement, the simulation with the conventional finite element tool CoventorWare and the simulation on MEMS+.

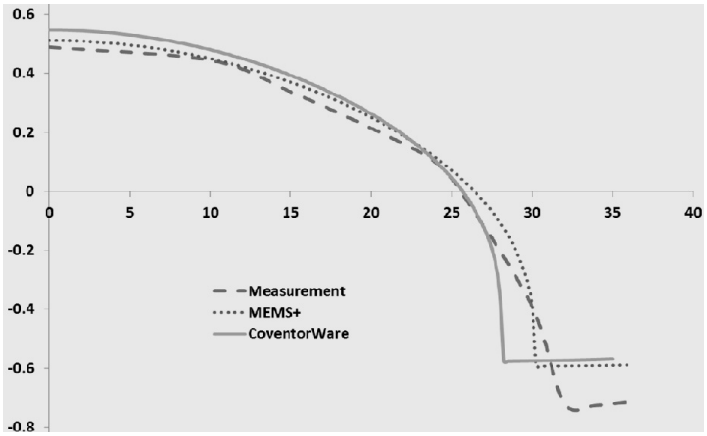

Fig. 8. Vertical displacement of the membrane versus actuation voltage.

Transient Analysis refers to the curve of displacement (μm) vs. time (μs) so as to obtain the required switching time of operation. Switching time is the main figure of merit for RF switches, but usually very difficult or even impossible to simulate with conventional modelling tools. Measurements and models of the switching time are shown in the Fig. 9. The switching speed of the RF switch is around 50 μs. Figure 9 shows a good agreement between the transient simulation of MEMS+ and the experimental measurement.

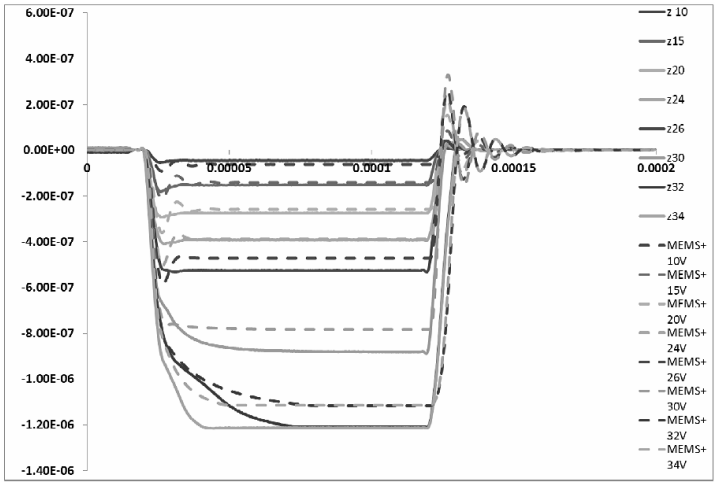

Fig. 9. Vertical displacement of the membrane versus time for different actuation voltages-compared to experimental measurements.

The performance of the fluidic model is evaluated by performing transient simulation at varying pressure conditions [6]. This model covers a wide range of situations, which may arise in the design and simulation of MEMS devices. The cavity pattern includes optional leakage resistances set by the user, and the model incorporates Reynolds terms of loss, automatically activated when the plates delimiting the volume of the cavity is perforated. The figure 10 shows the influence of the pressure on the switching time. The simulation has been done for an actuation voltage of 30 V and for a pressure varying from 10 kPa to 500 kPa.

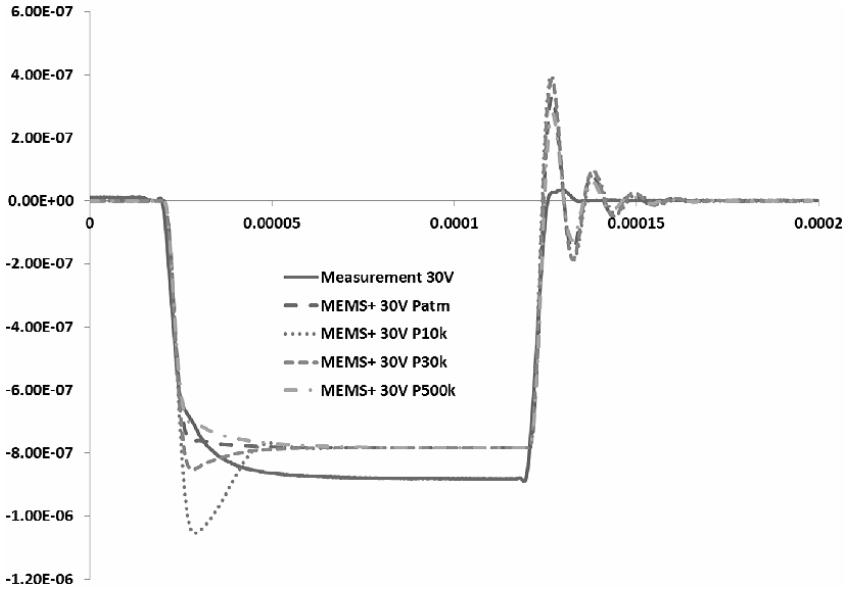

Fig. 10. Influence of the pressure on the switching time at 30 V.

4. Conclusions

This paper has shown the analysis using MEMS+ for the residual stress, actuation voltage and switching time of BiCMOS RF MEMS switches and compared with the experimental data. The proposed model shows very good agreement with the measured actuation voltage characteristic and with the transient measurements at ambient pressure. This analysis includes fluids mechanics (squeeze film damping, pressure adjustments), structural mechanics (equivalent mass, young modulus and pre-stress models) and electrostatics.

The overall result is a calibrated predictive MEMS+ model that enables to vary parameters of various origins (material, process, geometry) and perform in multiphysics studies (mechanic, electrostatic, fluidic..) in few hours while achieving the same or even better accuracy as with conventional finite element

approach. This opens the path to further design optimization and studies related to design for manufacturability taken into account process tolerances.

Ackowldedgments. Thanks to the European Commission Framework 7 project NANOTEC for support of this work and IHP for the support given on the technological parameters.

References

[1] G. LORENZ, G. SCHRÖPFER, *System-Level Modeling of MEMS*,3D Parametric-Library-Based MEMS/IC Design, Chapter **17**, T. Bechtold, G. Schrag, L. Feng (Editors), Wiley, 2012, ISBN: 978-3-527-31903-9

[2] G. SCHRÖPFER, G. LORENZ, S. BREIT, *Novel 3-D modeling methods for virtual fabrication and EDA compatible design of MEMS via parametric libraries*, Journal of Micromechanics and Microengineering **20**, pp. 064003, 2010.

[3] A. MEHDAOUI, G. SCHRÖPFER, G. LORENZ, M. KAYNAK, M. WIETSTRUCK, *New Methodology for Process Design Kit (PDK) of BiCMOS compatible RF MEMS*, MEMSWAVE Conference, Antalya, Turkey, July, 2012.

[4] M. WIETSTRUCK, *et al*., *Material Properties Characterization of BiCMOS BEOL Metal Stacks for RF MEMS Applications*" 12th International Symposium on RF MEMS and RF Microsystems, Athens, Greece, June 27-29, 2011.

[5] R. LaROSE, K. MURPHY, *Impact dynamics of MEMS switches*, Nonlinear Dynamics **60**(3), pp. 327–339, May, 2010.

[6] P.G. Steeneken, *et al*., *Dynamics and squeeze film gas damping of a capacitive RF MEMS switch*, Journal of Micromechanics and Microengineering **15**(1), pp. 176–184, 2005.

This volume is promoted by the Commission: *Science and Technology of Microsystems* of the Romanian Academy with the technical and financial support of the National Institute for Research and Development in Microtechnologies (IMT Bucharest, http://www.imt.ro). The volume is part of the *Micro and Nanoengineering series*, (coordinator – Professor Dan Dascalu, member of the Romanian Academy).